Alma Mater Studiorum – Università di Bologna

DOTTORATO DI RICERCA IN
Ingegneria Chimica, dell'Ambiente e della Sicurezza
XXVIII ciclo

Settore Concorsuale: 09/D3 Impianti e Processi Industriali Chimici
Settore Scientifico disciplinare: ING-IND/25

Fluid dynamic analysis of shaken and mechanically stirred reactors by means of optical techniques.

Irene Pieralisi

Coordinatore Dottorato
Prof. Serena Bandini

Relatore
Prof. Alessandro Paglianti

Esame finale anno 2016

1 General Introduction

1.1 Mixing

Mixing is one of the most widespread technologies in the chemical, petrochemical and pharmaceutical industries.

It aims at reducing the inhomogeneity of concentration, phase, or temperature of a single or multi-phase system, in order to achieve a desired process result (Paul et al., 2004).

To correctly accomplish this objective many aspects of the process have to be optimized, e.g. mass transfer, reactions, residence time and flow dynamics, revealing the intrinsic complexity of the operation.

For standard applications efficient scale-up criteria are readily available, while in many other cases the design of mixing apparatuses is still subjected to approximations and uncertainties.

Particularly, failure to address mixing scaling up in the early stages can result in poor product yield, quality, and physical attributes with substantial increase in manufacturing costs and delay/cancel of product marketing to fix the mixing problem (Paul et al., 2004). For example Butcher and Eagles (2002) report that annual losses due to poor mixing design are estimated in $2-11 billion worldwide, with a typical medium/large chemical plant experiencing around 12 operating problems related to mixing, which amount to $0.4-4m per year.

Detailed knowledge of the flow dynamics and turbulence levels occurring in a process is essential to increase its mixing performances, and careful selection of optimal flow conditions can reduce processing times, waste materials and power consumption.

1.2 Mechanically Stirred Tanks

According to the specific needs and objectives of the operation, mixing in vessels can be performed in different ways, through mechanical or magnetic agitation, gas sparging or using jets. However, due to their ease of construction, cleanness and versatility of operation, over 50% of the world's chemical production is performed in mechanically stirred tanks, that can be run in continuous, batch, or fed-batch mode.

In these apparatuses the movement is ensured by rotating impeller blades, whose shape and configuration are adjusted on the requirements of the mixing process. For example, axial flow

impellers are commonly used for liquid blending and solids suspension, while radial impellers are more efficient in gas dispersion processes.

In order to obtain the desired mixing performances, the geometrical features of the mixing system have to be carefully selected, as they influence significantly the mean and turbulent flow dynamics developing within the apparatus, and therefore the entire process.

Usually, mechanically stirred tanks of "standard geometry" are employed. They consist of baffled or unbaffled vessels with tank height-to-tank diameter ratio, $H/T \geq 1$, and impeller diameter-to-tank diameter ratio, $1/3 < D/T < 1/2$. Baffled systems have been studied for more than 50 years by means of experimental and computational investigations, leading to a deep knowledge of their flow and mixing dynamics, and to the development of reliable rules for process scale-up (Brown et al., 2004).

Attention has been also devoted to unbaffled stirred tanks of standard geometry. Typically, in these tanks a prevailing tangential flow develops, and, depending on impeller speed and liquid height, a definite vortex may expand from the free surface. On the contrary, in vessels equipped with baffles (typically 4 baffles at 90° from each other), the vortex formation is inhibited and the circulation of the fluid along tangential patterns is weaker. This leads to a stronger axial flow which improves the pumping flow rate and the mixing efficiency, thus making these apparatuses more suitable for many industrial applications.

Nevertheless, in some cases the use of unbaffled tanks has been shown to be convenient, as for example in food and pharmaceutical industries, where vessel cleanness is a fundamental requirement of the process (Assirelli et al., 2008), and in biological applications where cell damage has to be avoided (Aloi and Cherry, 1996; Scargiali et al., 2012-b). In solid suspension treatments, unbaffled tanks were found to give rise to higher fluid-particle mass transfer rates for a given power consumption (Grisafi and Brucato, 1994; Yoshida et al., 2008), and to ensure complete suspension attainment with lower mechanical power, if compared to baffled vessels requirements (Brucato et al., 2010; Wang et al., 2012).

When the process involves a very viscous fluid or a two-phase mixture at high solid concentration, baffles can actually worsen the mixer performances, as they give rise to dead zones where the solid particles tend to accumulate (Nagata, 1975; Lamberto et al., 1996; Rousseaux et al., 2001). Also, unbaffled systems are adopted in pharmaceutical applications involving the dissolution of powders (e.g., lyophilized proteins) into a liquid phase, as the feeding of solid material into the extensive central vortex has been proved to accelerate the process (Hormann et al., 2011).

Notwithstanding unbaffled stirred reactors may be suitable for a wide range of mixing applications, a characterization of the local flow field generated inside these apparatuses has rarely been performed (Armenante et al., 1997; Alcamo et la., 2005).

Even more complex is the case of unbaffled stirred tanks of unconventional geometry, as for example those commonly used for the production of biogas through wet fermentation of organic scraps. Typically, in anaerobic digesters huge volumes of biomass (from 1000 to 4000 m^3) are treated with very long residence time (weeks) in unbaffled stirred tanks of low aspect ratio, provided with single or multiple stirrers of small diameter to tank diameter ratio and partially filled (Weiland, 2010). This configuration is preferred to the "standard geometry" bioreactor, as it allows to reduce landscape impact and power consumption of the plant.

However, the peculiar geometry of the mixing apparatus and the absence of baffles determine the occurrence of peculiar interactions between the strong tangential motion of the flow, the impeller discharge stream and the flow free surface (Pieralisi et al. 2015). This leads to the evolution of a complex flow field, whose mean and turbulent characteristics have to be accurately monitored as they influence greatly process performances. So far, this aspect has rarely been considered (Reinecke et al., 2012; Montante and Paglianti, 2015), and the few available results cannot be applied to obtain general predictive equations for the bioreactors' behavior, as it is strictly related to the geometrical features of the configuration analyzed.

Consequently, the design and the operational conditions of digester systems are still subjected to relevant uncertainties (De Baere, 2000), resulting in commercial anaerobic digestion processes that are often operated well below their optimal efficiency (Ward et al., 2008).

To clarify the influence exerted by mixing on the anaerobic fermentation process, a better knowledge of the local hydrodynamics developing within the digester should be attained.

1.3 Orbitally Shaken Reactors

Another way of achieving mixing in vessels is through orbitally shaken systems, where mixing is induced by the rotating motion of the tray that is holding the vessel.

Shaking reactors are extremely simple systems, however there are some geometrical variables and operating conditions that have to be accurately set in order to obtain the desired mixing performances. In particular, vessel type and geometry, shaking diameter, presence of baffles, filling volume and shaking frequency have to be adjusted to meet process requirements (Buchs, 2001).

Shaken bioreactors are largely employed in many pharmaceutical and biological applications, as the absence of the impeller guarantees a low shear stress environment, which is essential for the evolution of most bioprocesses carried out. This characteristic together with the formation of a well-defined gas-liquid interface, make them particularly suitable for the culture of mammalian cells in terms of oxygen transfer and cell metabolism requirements (Liu et al., 2001; Muller et al., 2005).

Shaken systems are currently employed also in microcarrier-based culture methods for stem cells expansion, ensuring high cell productivity and short cultivation times, that allow to produce the huge number of cells needed for clinical trials (up to millions cells/kg of body weight) (Storm et al., 2010).

Shaking flasks or tanks with a typical nominal volume of 25 mL to 6 L are very widely applied for screening and bioprocess development, as these systems guarantee low power consumption, and the possibility of monitoring several conditions in parallel.

Once the process is optimized at small scale, it is then scaled-up to stirred tank reactors, which is the type of bioreactor most commonly used at production level.

However, the environmental conditions and the mixing mechanisms promoted by the two types of bioreactors are significantly different, and consequently, cell growth rate can experience critical variations along bioprocess development.

To overcome this problem, miniature stirred tanks have been employed in the early stages of process development, while large scale shaken systems up to a scale of 1000 L have recently become available in the market, and studies have demonstrated their mixing effectiveness and oxygen transfer capabilities (Zhang et al., 2009).

Notwithstanding more than 90% of all culture experiments in biotechnology are performed in shaking bioreactors (Buchs, 2001), and the importance of these systems is increasing considerably also at production level, little is known about the engineering aspects related to their operation (Suresh et al., 2009). Great uncertainties still exist in the selection of the suitable mixing conditions that can prevent shaken systems from the presence of spatial gradients in culture parameters, like nutrients concentration, oxygen transfer, and flow shear rate. This may lead to detrimental consequences for bioprocesses, whose optimization is rarely achieved. Only recently design and operating conditions guidelines to perform culture experiments in shaken systems have been described by Klöckner and Büchs (2012).

With the aim of improving mixing efficiency, the study of the hydrodynamics developing within shaken systems has shown to play a crucial role, as these phenomena have been proved to be the main responsible of the occurrence of inhomogeneities in culture parameters.

Big efforts have been recently devoted to this topics, and some light has been thrown on the mean and turbulent characteristics of the flow developing within cylindrical shaken systems and Erlenmeyer flasks. In addition, the magnitude and distribution of mixing, interfacial area, energy dissipation, shear stress and volumetric power consumption have been characterized for a series of operational conditions (Weheliye et al., 2013; Ducci and Weheliye, 2014; Rodriguez et al., 2013)

1.4 Aims and Objectives

This research aims at deepening the knowledge of some of the mixing processes outlined above, with the final objective of improving their performances. To this end, an experimental investigation of the hydrodynamics developing within some specific mixing system configurations is carried out. In particular, a standard geometry stirred vessel, an unbaffled stirred vessel of unconventional geometry and a shaken bioreactor are studied.

Optical techniques (LDA, PIV) are employed in order to obtain detailed information on the mean and turbulent characteristics of the flow developing within the different lab-scale reactors, while subsequent data analysis addresses the comprehension of the principal macro and micro phenomena occurring in the flow.

When studying the standard geometry stirred reactor, the evolution of trailing vortices on the wake of a PBT turbine is investigated for the first time under laminar regime. A three-dimensional characterization of the vortical structures is carried out in terms of vorticity levels and locus. This represents the starting point to assess the strain and deformation dynamics developing in the flow, and to establish the total surface deformation rate undergone by a virtual fluid element located in the vortex region.

The second case study regards an unbaffled stirred tank of low liquid height-to-tank diameter ratio, obtained from the scale-down of a digester industrially used for the wet fermentation of organic scraps. Due to the unconventional geometry of the system, peculiar interactions arise between the strong tangential motion of the flow, the impeller discharge stream and the flow free surface. Big efforts are devoted to the characterization of this phenomenon which seems to strongly influence the flow under certain operational conditions, and a mathematical model able to predict the onset and the impact of this macroinstability is sought for.

In the last part of this research, the operation of shaken bioreactors is explored. Particularly, the suspension dynamics occurring in the presence of solids within a flat-bottomed cylindrical system are investigated, and the associated two-phase flow is assessed by means of 2D-PIV. Also, the influence of a conical bottom on the single-phase flow is examined, and interesting results are collected for the correct operation of these devices.

A comparative study of the different bioreactors typologies allowed to identify interesting affinities never detected before in the fluid dynamic behaviour of unbaffled stirred tanks and shaken bioreactors, revealing that these two types of reactors can induce very similar flows, although being technologically very different.

1.5 Thesis Outline

The remainder of this thesis is subdivided in six chapters. In the following chapter the experimental techniques used for the present investigation are described. In chapter 3 an in-depth analysis of the hydrodynamics developing in a reactor equipped with an axial PBT turbine is carried out, with a special focus on the trailing vortex sctructures generated on the wake of the impeller.

Chapter 4 deals with the the characterization and prediction of the sloshing dynamics in a model unbaffled bioreactor, while in chapter 5 and 6 the mixing and flow dynamics encountered in an orbitally shaken bioreactor are investigated. In particular, chapter 5 looks at the suspension dynamics generated in a flat-bottomed cylindrical system in the condition of solid-liquid flow, and chapter 6 examines the impact exerted by a conical bottom on the single-phase hydrodynamics.

Finally, a brief overview of the research carried out, a summary of the main findings obtained, and recommendations for future developments are outlined in the last chapter.

1.6 References

Paul, E.L., Atiemo-Obeng, V.A., Kresta, S.M., 2004, Handbook of Industrial Mixing: Science and Practice. Wiley-Interscience, Hoboken, NJ.

Butcher, M., Eagles, W., 2002. Fluid mixing re-eengineered. The Chemical Engineer , 28–29.

Brown, D.A.R., Jones, P.N., Middleton, J.C., 2004, Experimental methods. In: Paul, E.L., Atiemo-Obeng V.A., Kresta, S.M. (Eds.), Handbook of Industrial Mixing: Science and Practice. Wiley-Interscience, Hoboken, NJ, pp. 183–184 (Chapter 4).

Assirelli, M., Bujalski W., Eaglesham A., Nienow A.W., (2008) Macro- and micromixing studies in an unbaffled vessel agitated by a Rushton turbine, Chem. Eng. Sci. 63, 35–46.

Aloi, L. E., Cherry, R. S., 1996, Cellular response to agitation characterized by energy dissipation at the impeller tip, Chem. Eng. Sci. 51, 1523–1529.

Scargiali, F., Busciglio A., Grisafi F., Brucato A., 2012-b, Oxygen transfer performance of unbaffled stirred vessels in view of their use as biochemical reactors for animal cell growth, Chem. Eng. Trans. 27, 205–210.

Grisafi, F., Brucato A., Rizzuti L., 1994, Solid–liquid mass transfer coefficient in mixing tanks: influence of side wall roughness, IChemE Symp. Ser. 136, 571–578.

Yoshida, M., Kimura, A., Yamagiwa, K., Ohkawa, A., Tezura, S., 2008, Movement of solid particles on and off bottom of an unbaffled vessel agitated by unsteadily forward–reverse rotating impeller, J. Fluid Sci. Technol. 3, 282–291.

Brucato, A., Cipollina, A., Grisafi, F., Scargiali, F. , Tamburini, A., 2010, Particle suspension in top-covered unbaffled tanks, Chem. Eng. Sci. 65, 3001–3008.

Wang, S., Boger, D.V. , Wu, J. ,2012, Energy efficient solids suspension in an agitated vessel-water slurry, Chem. Eng. Sci. 74, 233–243.

Nagata, S. ,1975, Mixing Principles and Applications, Halsted Press, New York.

Lamberto, D.J., Muzzio, F.J., Swanson, P. D. , Tonkovich, A. L.,1996, Using time dependent RPM to enhance mixing in stirred vessels, Chem. Eng. Sci. 51, 733–741.

Rousseaux, J.M., Muhr, H., Plasari, E.,2001, Mixing and micromixing times in the forced vortex region of unbaffled mixing devices, Can. J. Chem. Eng. 79, 697–707.

Hörmann, T., Suzzi, D., Khinast, J.G.,2011, Mixing and dissolution processes of pharmaceutical bulk materials in stirred tanks: experimental and numerical investigations, Ind. Eng. Chem. Res. 50, 12011-12025.

Armenante, P., Luo, C., Chou, C-C, Fort, I., Medek, J., 1997, Velocity profiles in a closed, unbaffled vessel: comparison between experimental LDV data and numerical CFD predictions, Chem. Eng. Sci. 52, 3483-3492.

Alcamo, R., Micale, G., Grisafi, F., Brucato, A., Ciofalo, M., 2005, Large-eddy simulation of turbulent flow in an unbaffled stirred tank driven by a Rushton turbine, Chem. Eng. Sci. 60, 2303–2316.

Weiland, P., 2010, Biogas production: current state and perspectives, Appl. Microbiol. Biotechnol. 85, 849-860.

Pieralisi, I., Montante, G., Vallini, V., Paglianti, A., 2015, Free Surface Instabilities in a Model Unbaffled Bioreactor, 10th Pacific Symposium on Flow Visualization and Image Processing, June 15-18, Naples, Italy

Reinecke, S., Deutschmann, A., Jobst, K., Kryk, H., Friedrich, E., Hampel, U., 2012, Flow following sensor particles – validation and macro-mixing analysis in a stirred fermentation vessel with a highly viscous substrate. Biochem. Eng. J. 69, 159–171.

Montante, G., Paglianti, A., 2015, Fluid dynamics characterization of a stirred model bio-methanation digester, Chem. Eng. Sci. 93, 38-47.

De Baere L., 2000, Anaerobic digestion of solid waste: state-of-the-art. Water Science and Technology, 41(3), 283–90.

Ward, A.J., Hobbs, P.J., Holliman, P.J., Jones, D.L., 2008. Optimisation of the anaerobic digestion of agricultural resources. Bioresour. Technol. 99, 7928–7940.

Buchs, J., 2001, Introduction to advantages and problems of shaken cultures. Biochem. Eng. J. 7, 91-98.

Liu, C.M., Hong, L.N., 2001, Development of a shaking bioreactor system for animal cell cultures. Biochem. Eng. J. 7, 121–125.

Muller, N., Girard, P., Hacker, D. L., Jordan, M., Wurm, F. M. 2005, Orbital shaker technology for the cultivation of mammalian cells in suspension. Biotechnol. Bioeng. 89, 400–406

Storm, M.P., Orchard, C.B., Bone, H.K., Chaudhuri, J.B., Welham, M.J., 2010, Three-dimensional culture systems for the expansion of pluripotent embryonic stem cells. Biotechnology and bioengineering 107, 683–695.

Zhang, X., Bürki, C.A.A., Stettler, M., De Sanctis, D., Perrone, M., Discacciati, M., Parolini, N., DeJesus, M., Hacker, D.L., Quarteroni, A., Wurm, F.M., 2009, Efficient oxygen transfer by surface aeration in shaken cylindrical containers for mammalian cell cultivation at volumetric scales up to 1000L. Biochem. Eng. J. 45, 41–47.

Suresh, S., Srivastava, V. C., Mishra, I. M., 2009, Techniques for oxygen transfer measurement in bioreactors: a review. Journal of Chemical Technology and Biotechnology, 84(8), 1091-1103.

Klöckner, W., and Büchs, J., 2012, Advances in shaking technologies. Trends in biotechnology, 30(6), 307-314.

Weheliye, W., Yianneskis, M., Ducci, A., 2013, On the Fluid Dynamics of Shaken Bioreactors - Flow Characterization and Transition. AIChE Journal 59, 334–344.

Ducci, A., Weheliye, W.H., 2014, Orbitally shaken bioreactors - Viscosity effects on flow characteristics. AIChE Journal 60, 3951–3968.

Rodriguez, G., Weheliye, W., Anderlei, T., Micheletti, M., Yianneskis, M., Ducci, A., 2013, Mixing time and kinetic energy measurements in a shaken cylindrical bioreactor. Chemical Engineering Research and Design 91, 2084–2097.

2 Experimental Techniques

2.1 Introduction

This chapter provides a detailed description of the experimental methods employed along the present study. In Section 2.2 the attention is focused on the Laser Doppler Anemometry technique, employed to determine the mean and turbulent flow field within a PBT-mechanically stirred reactor. An overview on the mean working principles of the optical technique is provided, together with a detailed description of the experimental LDA apparatus employed.
In Section 2.3 the main features of Particle Image Velocimetry are presented. This technique has been extensively used along this study to gain information on the flow developing within different types of reactors. Particularly, an unbaffled stirred tank and cylindrical shaken bioreactors with different bottom configurations have been investigated in the single-phase condition, while two-phase PIV has been employed to understand the fluid dynamic features of a solid-liquid flow within a shaken system.

2.2 Laser Doppler Anemometry

2.2.1 LDA principle

Laser Doppler Anemometry is a well-known experimental technique employed in the fluid dynamic analysis of gaseous and liquid flows. It provides local information on the velocity vector, and through multiple measurements it allows a reconstruction of the entire volumetric flow field developing within a reactor. Reliable measurements are carried out if the investigated fluid is transparent, the geometrical features of the system enable the optical access of the laser beams, and the fluid is seeded with a suitable tracer.
It has many advantages if compared to other experimental techniques traditionally employed in fluid dynamic investigations:
- it carries out an optical measure of the velocity, thus it is not intrusive and it doesn't influence flow characteristics;
- it provides information not only on the intensity, but also on the direction of the velocity vector;
- it is able to measure simultaneously multiple velocity components: the standard LDA apparatus gives information on two velocity components, while 3D-LDA enables a direct characterization of the velocity vector in all its directions;

- the technique has a very high temporal and spatial resolution;
- it doesn't require any calibration as the measure is absolute and based on the stability of electromagnetic waves.

LDA is based on the Doppler principle, stating that a particle in motion reflects the light with a frequency depending only on its speed. When two electromagnetic waves cross each other in the respective waist regions, the front of waves is planar and perpendicular to the direction of propagation, and the phenomenon of interference occurs manifesting with parallel light and dark fringes. The fringes are spaced at a distance λ^*, according to Equation 2.1:

$$\lambda^* = \frac{\lambda}{2 \sin(\delta)} \tag{2.1}$$

where λ is the wavelength of the laser beam employed, and δ is the half beam angle between two intersecting beams.

As a particle crosses the fringes the light is scattered with a Doppler frequency f_D directly proportional to the velocity of the particle as expressed by Equation 2.2:

$$U = f_D \frac{\lambda}{2 \sin(\delta)} \tag{2.2}$$

However, f_D is independent of the velocity direction, meaning that particles moving with the same velocity normal to the fringes but with opposite orientation will produce the same Doppler frequency. To resolve this directional ambiguity a constant freqeuncy shift, f_{shift} , is applied to one laser beam, and the measured velocity is calculated as follows (Equation 2.3):

$$U = (f_{shift} \pm f_D) \frac{\lambda}{2 \sin(\delta)} \tag{2.3}$$

with the $\pm$ depending on the direction of the moving particle.

Due to the Gaussian distribution of the laser beam intensity, the measuring volume has an ellipsoid shape. Its dimensions are defined considering the 13% ($1/e^2$) of the maximum beam intensity and are proportional to the diameter d_f of the beam waist, as follows:

$$d_y = d_f \tag{2.4-a}$$

$$d_x = \frac{d_f}{\cos(\delta)} \tag{2.4-b}$$

$$d_z = \mu' \frac{d_f}{\sin(\delta)} \tag{2.4-c}$$

where d_y, d_x and d_z indicate respectively the diameter in the plane of the fringes, the diameter in the direction normal to the fringes, and for the length. In Equation 2.4-c, the elongation of the measuring volume due to the refractive index of the fluid μ' has been considered.

Finally, Equation 2.5 shows how the beam waist diameter is calculated:

$$df = \frac{4\, f\, \lambda}{\pi E\, d_I} \tag{2.5}$$

where f indicates the focal distance of the lens eployed, d_I is the beam waist diameter before passing the focusing lens and E is the beam expansion factor.

2.2.2 LDA apparatus

The LDA employed in the present study is a commercial Dantec Ltd. system with a two-dimensional probe, that can measure at the same time two components of the velocity of the flow under study. The probe works in back-scattered mode, meaning that the devices transmitting the laser beams and receiving the scattered light are integrated in a single unit.

The laser employed is a water cooled Argon-Ion Innova 90C-5 (Coherent Inc.) that can provide a maximum power of 5 W.

A transmitter box containing a Brag cell splits the original laser light into two beams, one blue (λ = 488.0 nm), and one green (λ = 514.5 nm), then each radiation is divided into two beams, one of which is shifted by 40 MHz. The two couple of radiations are focused in the measuring volume and allow to measure two components of the velocity vector.

The light scattered by the seeding particles is collected and sent to a photomultiplier which amplifies its intensity. Then, a Burst Spectrum Analyser (BSA) analyses the signal and determines in the spectrum of the burst the dominant frequency, f_D, corresponding to the velocity of the particle that crossed the measuring volume.

The data are validated when the frequency f_D is at least four times higher than the second highest local peak in the spectrum of the burst.

To resolve the smallest scales of the flow field, the experiments are carried out with a beam expanders mounted on the probe, and with a lens of focal length 310 mm, which ensures a high spatial resolution.

The probe is mounted on a light-weight transverse that can be remotely moved along the three orthogonal direction of the coordinate system.

To carry out the experiments silver coated hollow particles are used as tracer. A diameter of 10 μm is chosen, so the particles are small enough to follow accurately the flow, but also large enough to scatter an amount of light clearly detectable by the photo-detector unit.

To avoid multiple simultaneous bursts from a single control volume, the concentration of particles is kept sufficiently low, and an oscilloscope is used to control the signal.

2.3 Particle Image Velocimetry

Particle Image Velocimetry is a non-intrusive optical technique that allows to measure the instantaneous velocity vector field of a flow over a plane of interest. It is a well-established technique that has been employed over the last 30 years to study a big variety of flows, with several applications in the chemical and biochemical field.

To carry out the experiments neutrally-buoyant particles are added to the flow as a tracer.

By means of a high-powered laser a plane within the seeded flow is illuminated, and the light scattered by the particles is recorded via a high quality lens on two separate frames of a digital camera. The light sheet is shone twice with a time delay between the two pulses depending on the mean flow velocity and on the magnification of the image.

By capturing two images at successive time instants, the displacement of the particles can be determined.

Specifically, the time delay must be long enough to be able to determine the displacement of the particles between the two images with sufficient resolution, but short enough to avoid particles leaving the light sheet due to the out-of-plane velocity component.

Also, the duration of the laser pulse must be sufficiently short to “freeze” the motion of the particles during the light exposure and to avoid blurring of the image.

The digital PIV recordings are then divided in small subareas called "interrogation areas", where it is assumed that all particles have moved homogeneously between two illuminations.

The local displacement vector for the two images is determined by means of statistical methods like auto and cross correlation. Hence, the projection of the velocity vector into the plane of measurement is calculated taking into account the time delay between the two pulses. The same process is repeated for all interrogation areas until a complete reconstruction of the two-dimensional flow field is achieved. Modern charge coupled device cameras (CCD) allow to capture a great amount of data and to transfer the output of the digital sensor directly to the memory of a computer.

A schematic diagram of the PIV working principle is shown in Figure 2.1.

Hence, PIV is an optical technique that works non-intrusively, and this allows its application even in high-speed flows or in boundary layers close to the wall, where the flow may be disturbed by the presence of the probes.

In addition, PIV has the unique feature of determining velocity vector fields over large flow areas, while all the other techniques (e.g. LDA) only allow single point measurements.

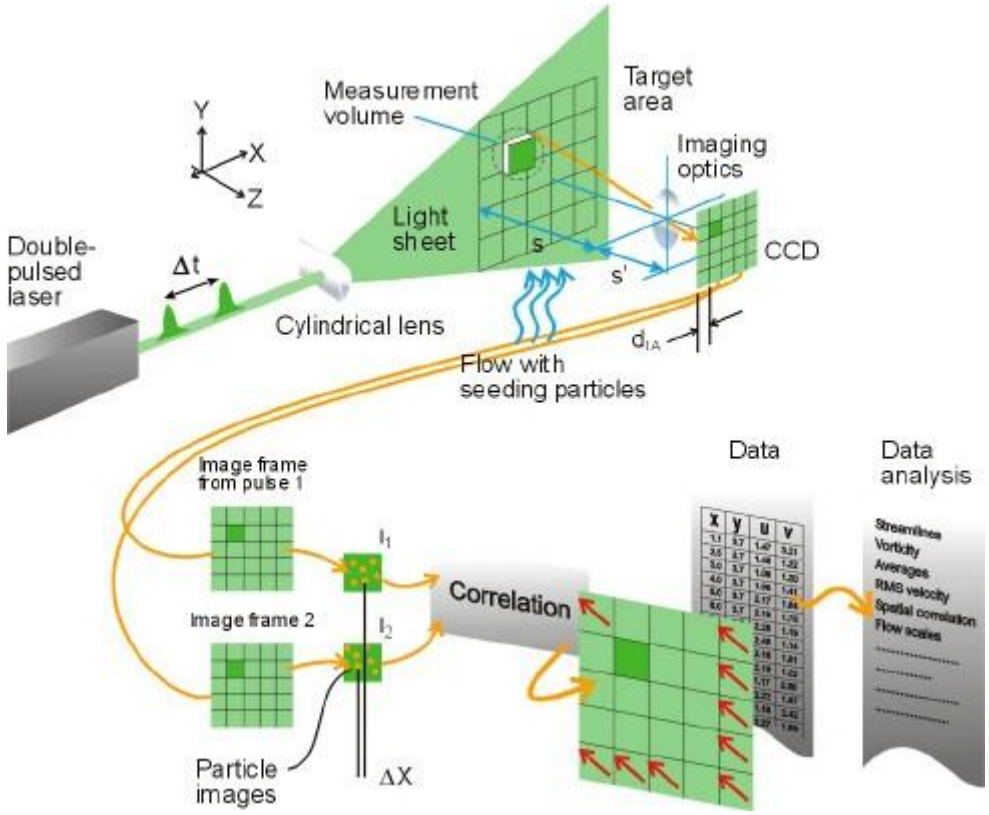

Figure 2.1: Schematic diagram showing PIV working principles (from www.dantecdynamics.com)

Two-phase PIV is a particular application of the technique, that allows to simultaneously and separately measure the velocities of a two-phase flow. The working principle is the same, but two cameras provided with appropriate light filters are employed to distinguish between the two phases. In this way each camera is able to see only the light scattered by either the solid particles (or gas bubbles) or the flow tracer, and velocity vector fields of solid-liquid or gas-liquid flows are determined independently analyzing the twin sets of images recorded by the two cameras.

In this study both a single and a two-phase PIV systems are employed. More detailed information on the characteristics of the laser and cameras used in each investigations are provided in the subsequent sections.

3 Characterisation of the fluid dynamics in a reactor equipped with an axial PBT turbine

3.1 Introduction on Pitched Blade Turbines

Pitched-blade turbines, PBTs, are commonly used in industrial applications where a strong axial flow is required, as for example, in solid suspensions (see Unadkat et al., 2009) or gas dispersion systems (see Khopkar et al., 2003). Under turbulent regime, the effects of the PBT impeller design (blade number, blade angle, blade and disk dimensions), and the location of the impeller (off-bottom clearance, impeller eccentricity), on the liquid-phase flow dynamics, have been extensively studied experimentally by means of flow visualizations (e.g. Tatterson and Stanford, 1981; Ali et al., 1981), Laser Doppler Anemometry, LDA, (e.g. Yianneskis et al., 1987; Ranade and Joshi, 1989; Kresta and Wood, 1993; Jaworski et al., 2001) and high resolution Particle Image Velocimetry, PIV (e.g. Aubin et al., 2001; Chapple et al., 2002; Khan et al., 2004; Kumaresan and Joshi, 2006).

The trailing vortices produced by the blade passage have been investigated, as their structure and turbulence content play a major role in the mixing dynamics occurring in the reactor, as for example blade trailing vortices control ligament and sheet production in liquid-liquid dispersion systems (Sheu et al., 1982) and micromixing in fast competitive reaction processes (Villermaux, 1986). The flow visualizations of Tatterson and Stanford (1981) were the first to address the trailing vortex structures generated by a down pumping 45° four-bladed turbine operating under turbulent regime. Their experiments showed the formation of a single vortical structure behind each blade, with its axis oriented vertically downward and radially outward. Similar findings were obtained by Ali et al. (1981) by means of stereoscopic motion pictures. They reported a single vortex at the edge of a 45° PBT, with vortex tangential velocities of 0.25 V_{tip} for all impeller speeds investigated, and vortex diameter increasing with increasing distance from the blade, as more fluid is entrained within the vortex. Schäfer et al. (1998) used phase-resolved LDA measurements to study the fluid dynamics in a PBT stirred tank reactor at various Reynolds numbers, and found that the flow regime was fully turbulent for $Re > 2300$. For turbulent flow regime they reported the presence of a single trailing vortex of spiral shape and oval cross section formed primarily by the interaction of the flow along the upstream and downstream blade surfaces. In agreement with the results of Ali et al. (1981), Schäfer et al. (1998) found that the vortex axis was inclined by 20° with respect to the horizontal

direction, while its radial distance from the reactor axis did not vary with increasing azimuthal coordinate from the back of the blade, φ. The LDA experiments of Kresta and Wood (1993) showed the presence of a secondary smaller vortex at the upper tip of each blade, which was considered by Schäfer et al. (1998) part of the main single trailing vortex.

A multi-block approach combining in a single flow map different sets of PIV data obtained in different section of the reactor, was devise by Khan et al. (2004) and applied to a stirred vessel operating at Re = 50000. Phase-resolved measurements of the radial and axial velocity components allowed to visualise the trailing vortex generated by the impeller, which was found in good agreement with the results of Schäfer et al. (1998). In a following work, Khan et al. (2006) used stereoscopic PIV to obtain a complete 3D characterization of the reactor flow, and found that turbulence intensity in the trailing vortex core was higher than that predicted assuming pseudo-isotropy. This is in agreement with the findings of Hockey and Nouri (1996) and Tyagi et al. (2007), who reported anisotropic turbulence in proximity of the impeller, which they associated to the presence of the trailing vortices. A recent work of Roy et al. (2010) investigated the interactions between low frequency macro-instabilities (MI) and large-scale flow structures, and concluded that the former affected significantly the size of the trailing vortices.

Although mixing is usually conducted at high Reynolds numbers, in some applications involving viscous fluids or shear sensitive material, turbulence should be avoided, and stirred reactors must be operated under laminar flow regime, as for polymerization and bioprocesses (Woziwodzki and Jedrzejczak, 2011). From this point of view laminar mixing improves significantly the mass diffusion phenomena, as the strain and shear deformation rates induced by the flow increase the interfacial area where the material exchange takes place.

Laminar mixing in stirred reactors equipped with pitched-blade impellers have been investigated by Lamberto et al. (1996), Harvey et al. (2000) and Alvarez et al. (2002). Nouri and Whitelaw (1990) assessed the flow dynamics of a PBT at low Reynolds numbers by means of LDA experiments ($Re \leq 3000$),and reported that at these regimes the flow remained more attached to the blade surfaces, and a progressive change in the angle discharge stream of the PBT impeller was produced as Re was decreased, with a maximum discharge angle of 75° from the axial direction at Re = 500. Similarly, Hockey and Nouri (1996) reported a change in the discharge stream direction from primarily radial to primarily axial for $Re \geq 490$ and $Re \geq 650$ for 45° and 60° PBTs, respectively. The LDA results of Bakker et al. (1996) showed that the PBT region was dominated by radial flow

at Re = 21, while the bulk of the tank was controlled by the tangential velocity component, with poor recirculation of fluid over vertical planes.

Although the influence of the Reynolds number seems extremely relevant even on the mean flow patterns of the fluid, no one has investigated so far the occurrence and the characteristics of trailing vortex structures under laminar conditions. As deeper understanding of this aspect is deemed very important for process optimization, in the current study an LDA system has been employed to obtain ensemble and angle-resolved velocity measurements in a PBT stirred tank operating at Re = 1200. Trailing vortex structures were detected and accurately characterized, while subsequent data analysis allowed to perform a three-dimensional visualization of the large-scale vortical patterns, and to assess the strain and deformation dynamics undergone by the fluid inside the tank.

3.2 Experimental Apparatus

Phase resolved LDA measurements were carried out in a stirred tank of standard geometry with flat-bottom, diameter T = 294 mm and height $H = T$. The tank was covered with a lid and filled to the top, to prevent air entrainment in the system. Four equally spaced baffles of thickness $T/100$ and width $T/10$ were positioned at right angles on the vessel wall. A square trough was employed to minimise optical distortion at the cylinder surface, while optical access from the bottom of the reactor was gained from a glass window inserted into the stainless steel base. As shown in Figure 3.1, the impeller was a 45° four-bladed down pumping PBT of diameter $D = 0.5\ T$ (147 mm), blade thickness $t = 0.018\ D$ (2.7 mm), and height $W = 0.2\ D$ (29.4 mm), the off-bottom clearance was set to $C = T/2$ (147 mm).

The working fluid was a mixture of 80% glycerin in volume and 20% water, with a dynamic viscosity, μ = 89.4 mPa s, and a density, ρ = 1210 kg/m^3 ($\nu \approx 73.8\ 10^{-6}$ m^2 s^{-1}). In order to avoid variation of the fluid properties, the working temperature was kept constant at T = 20 °C with a constant temperature recirculation bath and checked periodically by means of a high resolution thermometer. The impeller rotational speed was N = 165 rpm, resulting in a tip blade velocity, V_{tip} = 1.28 m/s, and $Re \approx 810$. The 2D LDA experiments were carried out in the impeller stream on a vertical plane located half-way between two adjacent baffles. In order to obtain accurate estimates of the deformation rate velocity gradients, high resolution measurements were obtained in the region visualised in Figure 3.1, which comprised 900 points 1 mm apart both in the vertical and

radial directions. Phase resolved averages were obtained with an optical shaft encoder aligned with the centreline of the blade tip.

The 2D-Dantec LDA probe worked in back-scattered mode, and was arranged either horizontally, entering the tank from the side, or vertically, entering the tank from the bottom, to obtain simultaneous measurements of the axial and tangential velocity components, u_z -u_θ , or of the radial and tangential ones, u_r -u_θ , respectively. To verify the reproducibility of the measurements, and to validate the data, the profiles of u_θ obtained in both configuration were systematically compared, and a good agreement between the two samples was found in every point of the mesh, apart for those located in the impeller wept region, which was accessible to a different degree depending on the probe set up employed. The probe was equipped with a 310 mm focal length lens resulting in a control volume of 3.6 x10^{-3} mm^3 for the green channel (λ = 514.4 nm), and 3 x10^{-3} mm^3 for the blue channel (λ = 488 nm). To minimize statistical errors a sample of 100000 velocity measurements was obtained in each point, resulting in approximately 1000 velocity data for each phase angle. In the remaining of this work a cylindrical coordinate system is employed with the origin set at the centre of the vessel base, and the azimuthal coordinate rotating counter-clockwise when the system is seen from above.

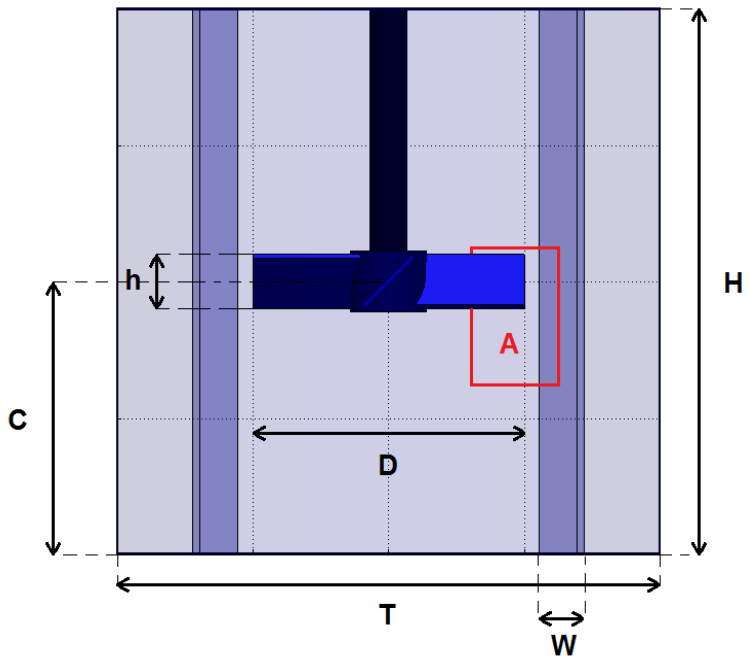

Figure 3.1: Front view of the reactor and visualisation of the measurement region.

3.3 Theoretical Background

The methodology developed by Bouremel et al. (2009) is employed in this study to assess the deformation dynamics undergone by a virtual fluid particle located in the stream of a down-pumping pitched blade turbine. The deformation rate tensor is obtained from the gradient of the velocity vector, ∇u, which can be decomposed into the symmetric part, the strain rate tensor, S, and the antisymmetric one, the rotation rate tensor, Ω, of Equation 3.1 (Davidson, 2004).

$$\nabla u = S + \Omega = \left(\frac{\nabla u + \nabla u^T}{2}\right) + \left(\frac{\nabla u - \nabla u^T}{2}\right) \tag{3.1}$$

A better understanding of the strain dynamics locally induced by the flow can be obtained from the principal components of the strain rate tensor, see Equation 3.2, and the associated eigenvectors:

$$\nabla u = \begin{pmatrix} S_{11}^* & 0 & 0 \\ 0 & S_{22}^* & 0 \\ 0 & 0 & S_{33}^* \end{pmatrix} + 0.5 \begin{pmatrix} 0 & -\omega_3^* & \omega_2^* \\ \omega_3^* & 0 & -\omega_1^* \\ -\omega_2^* & \omega_1^* & 0 \end{pmatrix} \tag{3.2}$$

where S_{11}*, S_{22}*, S_{33}* and ω_1*, ω_2*, and ω_3* correspond to the strain and rotation terms estimated along the principal directions of the strain rate tensor. Each S_{ii}*, is an eigenvalue of the matrix *S*, which indicates the local intensity of the strain, and corresponds to an eigenvector, related to the direction along which the strain operates. To identify clearly this direction, two parameters were used: γ_i* and δ_i*, defined as the angles included between the i-th principal eigenvector and the tangential and radial directions, respectively. The parameter S_{11}* x S_{22}* x S_{33}* can be used to assess whether a blob of fluid is locally subject to axial strain (i.e. two principal directions of compression and one of stretching, S_{11}* x S_{22}* x S_{33}* > 0) or biaxial strain (i.e. two principal directions of stretching and one of compression S_{11}* x S_{22}* x S_{33}* < 0).

An assessment of the derivative terms included in the deformation rate tensor was made by considering the volume balance of the continuity equation, which is reported in Equation 3.3 in a cylindrical coordinate system and for an incompressible fluid.

$$\underbrace{\frac{1}{r}\frac{\partial u_\theta}{\partial \theta} + \frac{u_r}{r} + \frac{\partial u_r}{\partial r}}_{C_1} + \underbrace{\frac{\partial u_z}{\partial z}}_{-C_2} = 0 \tag{3.3}$$

The axial profiles of the terms C_1 and C_2 defined in Equation 3.3 are shown in Figures 3.2 (a) and (b) for two radial coordinates r/D = 0.483 and r/D = 0.435, respectively. To better visualise the position of the axial profiles with respect to the vortices generated by the blade, Figures 3.2 (a, b) also include the variation of the radial vorticity. The two sets of profiles exhibit an overall good agreement, with the average absolute difference between C_1 and C_2 being 14 % and 10 % of C_2 max for the two radial coordinates considered. Similar values were obtained across the entire measurement domain.

The surface deformation rate experienced by a virtual spherical fluid particle located in the flow was estimated according to the analysis described in Bouremel et al. (2009). The surface of the virtual particle was meshed according to a spherical coordinate system (r, α, β), and the strain rate tensor on the sphere surface was obtained through a three-dimensional interpolation of the measured strain rate in the cylindrical measurement grid. The rate of surface deformation, $d(ln\eta)/dt$, experienced by each facet of the sphere was calculated using the Ottino (1989) for incompressible fluids (Equation 3.4), which expresses the proportionality between the local percentage variation of the surface, dA/A, and the component of the strain rate tensor along the local normal to the surface, n.

$$d(\ln \eta) = \frac{dA}{A} = -S_{nn} dt \tag{3.4}$$

The total surface deformation rate, η'_{tot}, was estimated from the integral of S_{nn} over the external area of the sphere (Equation 3.5).

$$\eta'_{tot} = -\frac{1}{4\pi} \int_0^{\pi} \int_0^{2\pi} S_{nn} \sin(\alpha) d\beta d\alpha \tag{3.5}$$

It should be pointed out that the mesh size used to approximate the spherical particles has to be carefully selected as it directly affects the final value of η'_{tot}. This is more evident when considering Figure 3.3 where the variations with angular mesh size, $\Delta\alpha$, $\Delta\beta$, of the total surface deformation $\eta'_{tot}/(N\pi)$ and of the non dimensional surface, $A_s/(4\pi r_s^2)$, are plotted on the left and right hand side ordinates, respectively (virtual spherical particle located located at r/D = 0.49, z/D = 0.864, θ = 75°). As expected, finer meshes result in particles closer to a spherical shape, with the nondimensional ratio $A_s/(4\pi r_s^2)$ assuming a value of 0.98 for $\Delta\alpha = \Delta\beta$ = 5°. Similarly the total surface deformation, $\eta'_{tot}/(N\pi)$, is denoted by a deviation lower the 10 % from the highest angular resolution value (i.e. $\eta'_{tot}/(N\pi) \approx 0.013$ for $\Delta\alpha = \Delta\beta$ = 3°) for $\Delta\alpha = \Delta\beta < 10°$. Based on this the data presented in the rest of the paper were estimated for $\Delta\alpha = \Delta\beta$ = 3°.

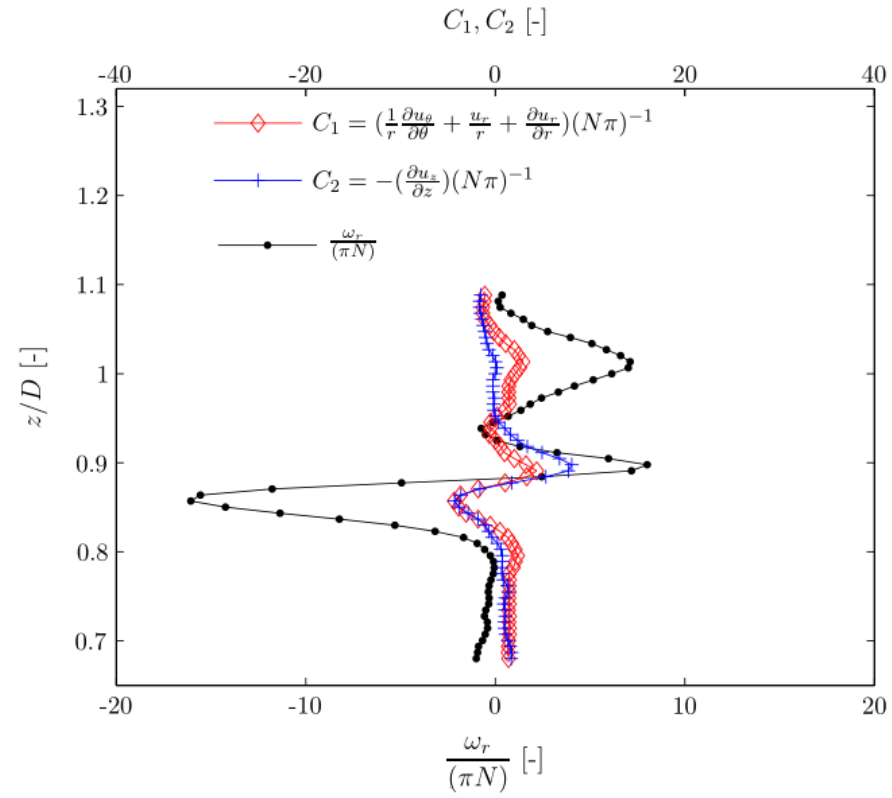

(a)

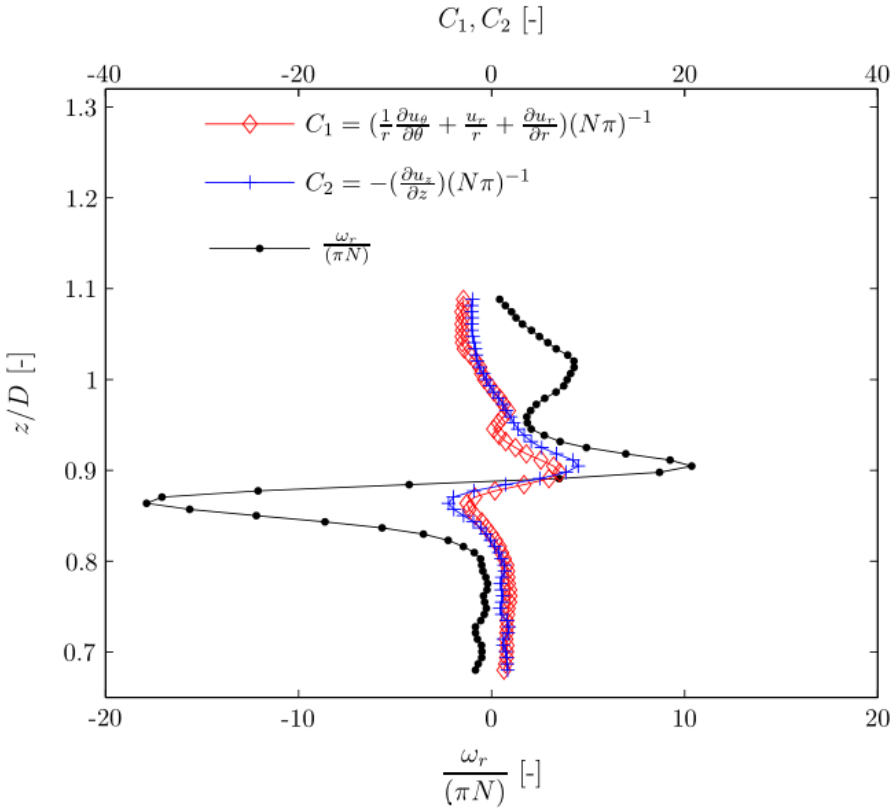

(b)

Figure 3.2: Axial profiles of $[(1/r)(\partial u_\theta/\partial\theta) + (u_r/r) + (\partial u_r/\partial r)]N^{-1}$ and $-(\partial u_z/\partial z)N^{-1}$, at: (a) r/D = 0.483, θ = 70° ; (b) r/D = 0.435, θ = 70° .

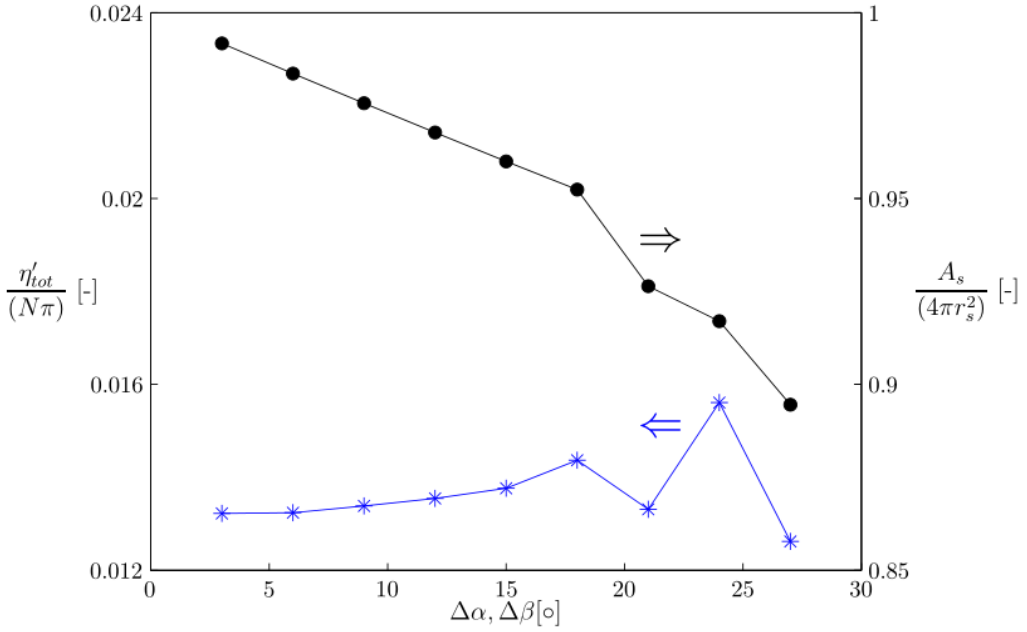

Figure 3.3: Variation of the sphere surface, $A_s/(4\pi r^2_s)$, and of its total surface deformation rate, η'_{tot} for different mesh sizes, $\Delta\alpha$, $\Delta\beta$: (•) $A_s/(4\pi r^2_s)$; (∗), η'_{tot} (r/D = 0.49, z/D = 0.864, θ = 75°).

3.4 Results and Discussion

3.4.1 Ensamble- and Phase-Averaged Velocity Fields

Through ensemble-averaged measurements in the impeller discharge stream, the mean velocity flow field in a vertical plane of the reactor was obtained (Figure 3.4). The single-loop flow pattern typically induced by an axial turbine can be identified: the fluid is driven mainly vertically by the leading blade, proceeds in the direction of the vessel wall, and then it is recirculated towards the center by the passage of the following blade. However, the axial stream doesn't reach the bottom of the tank, but rises gradually for decreasing values of z/D, until it exhibits an inclination of only 15° from the horizontal direction, at an height of z/D = 0.65. Below this value, the flow is fully radial and has a very low intensity, suggesting that there may be problems if processes involving lifting of solids are implemented in the reactor. This is due to the laminar flow regime established inside the tank, and to the weak pumping action of the turbine, which cannot convey its motion to the whole volume of fluid.

Another effect consequence of the low Reynolds number, is that the impeller discharge stream is not strictly axial, with mean velocities exhibiting an average inclination of 33° from the vertical axis, if points of coordinates $0.42 < r/D < 0.54$ and $0.82 < z/D < 0.94$ are considered. This result is

in agreement with Nouri and Whitelaw (1990a), who assessed that decreasing levels of turbulence inside the reactor, generate a progressively radial flow. Figure 3.4 also displays the contour map of the tangential component of the vorticity, $\omega_\theta/(N\pi)$, computed using the ensemble-averaged velocity data. In the whole area investigated these values appear very low, and relevant vortical structures cannot be identified.

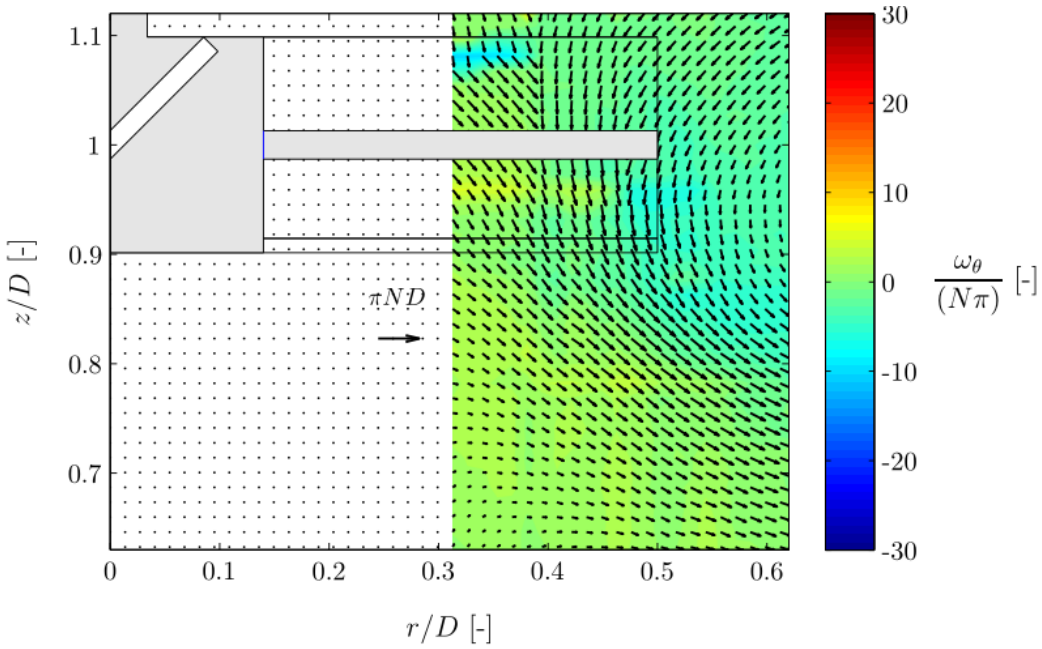

Figure 3.4: Ensemble-averaged flow field and contour map of the tangential component of the vorticity, ω_θ, for N = 166 rpm (Re = 1200).

Looking at the phase-averaged results, obtained for each angular coordinate θ, a maximum intensity of 18 was reported for $\omega_\theta/(N\pi)$, whereas the radial component of the vorticity, $\omega_r/(N\pi)$, assumed twofold values ranging between -42 and 51, as visible from Figure 3.5. This suggests that in a PBT-stirred reactor working under laminar regime, vortical structures would more likely develop along the radial direction rather than the tangential, as inferred by many authors who considered the turbulent flow case (Kresta and Wood, 1993a, Tatterson et al., 1980, Ali et al., 1981, Schafer et al., 1998). Therefore, from this point on a greater attention was addressed to the radial component of the vorticity, which is displayed in the contour plots of the following figures.

Phase-resolved vector fields in vertical planes are shown in Figure 3.5 a-d, for four different values of θ: 0° , 9° , 16° , 25° . To better comprehend the images, it should be considered that the blade is moving inside the page, and that in certain points the velocity vectors is not available because during the measurements the impeller was partially obstructing the laser beams (Figure 3.5 a-b).

Observing the four contour plots of $\omega_r /(N\pi)$, the occurrence of two trailing vortices can be noticed, and some of their characteristics can be already outlined. The swirling structures are counter-rotating and never merge together, but remain clearly separates, even if as θ increases, their intensity gets lower.

To describe trailing vortices more accurately, the flow field and vorticity levels of the fluid were analyzed in azimuthal planes, and are shown in Figure 3.6, for three different values of the radial coordinate r/D (r/D = 0.428; r/D = 0.5; r/D = 0.531). The images show that the fluid circulates with tangential velocities comparable to the axial and radial ones, and that due to the pumping action of the turbine, the flow assumes a direction almost perpendicular to the turbine blades. However, when $z/D < 0.75$, all the three components of the velocity assume negligible values, and the global intensity of the flow dramatically decreases, as reported in the analysis of Figure 3.6, for a similar axial position. Trailing vortices start growing at the tips of each blade, and develop along the tangential coordinate, giving rise to almost parallel wakes of decreasing strength. Looking at the contour plot of the radial component of the vorticity, $\omega_r /(N\pi)$, it is evident that apart from the direction of circulation (the red vortex rotates counter-clockwise, while the blue clockwise), the two vortices present very similar characteristics, assuming absolute intensities comparable at any r/D considered, and generating in both cases wakes with an inclination of about 20° from the horizontal direction. The vortices maintain their features almost unaltered as the radial coordinate increases, but for r/D greater than the blades radius, they lose gradually intensity, until they disappear at around r/D = 0.6.

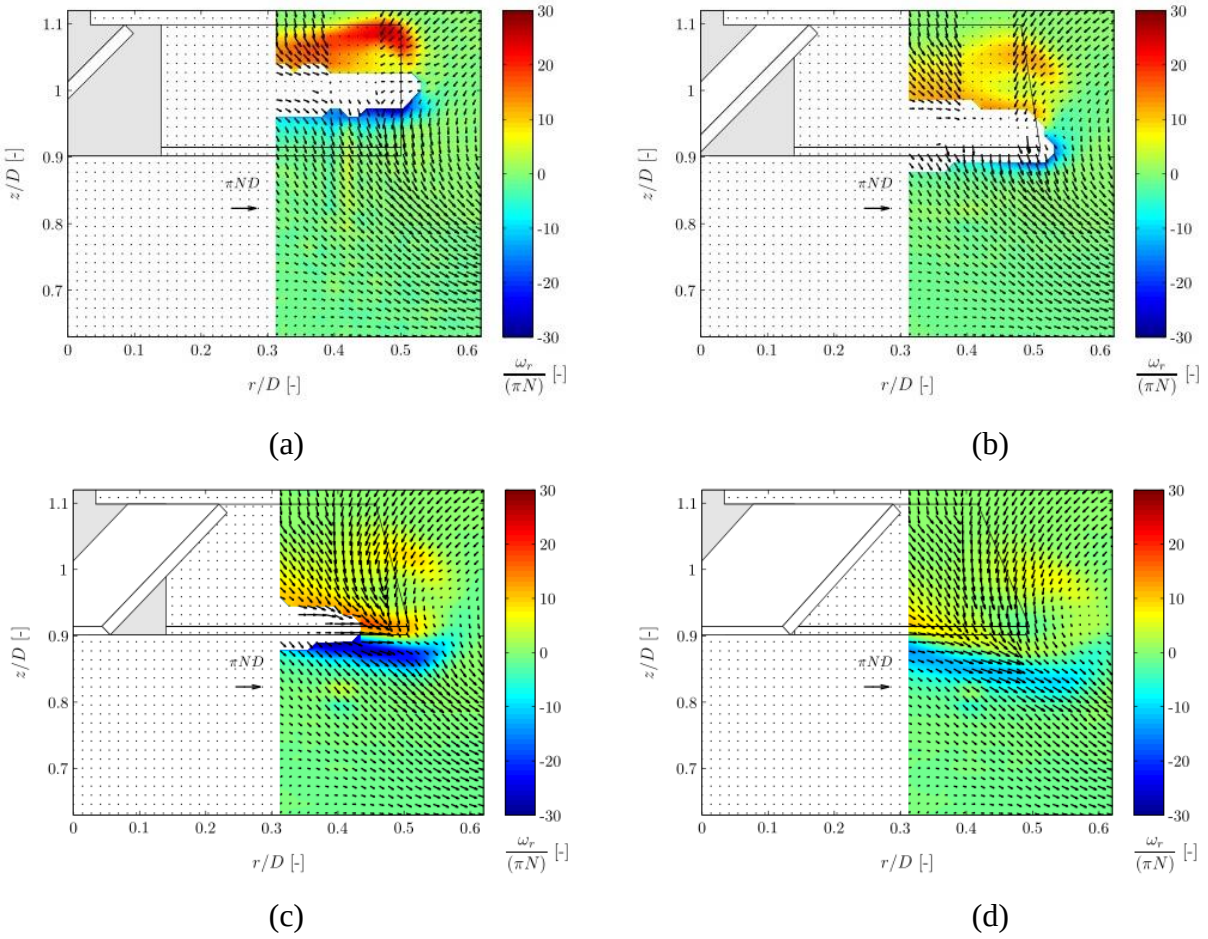

Figure 3.5: Phase-resolved flow fields and contour plots of the radial component of the vorticity, ω_r, for N = 166 rpm (Re = 1200), in different axial planes: (a) θ = 0°; (b) θ = 9°; (c) θ = 16°; (d) θ = 25°.

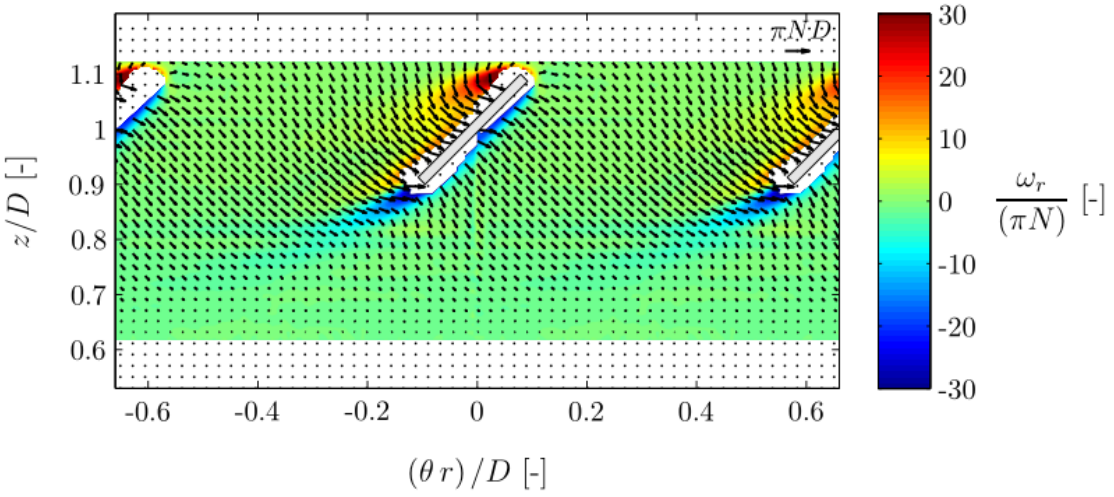

(a)

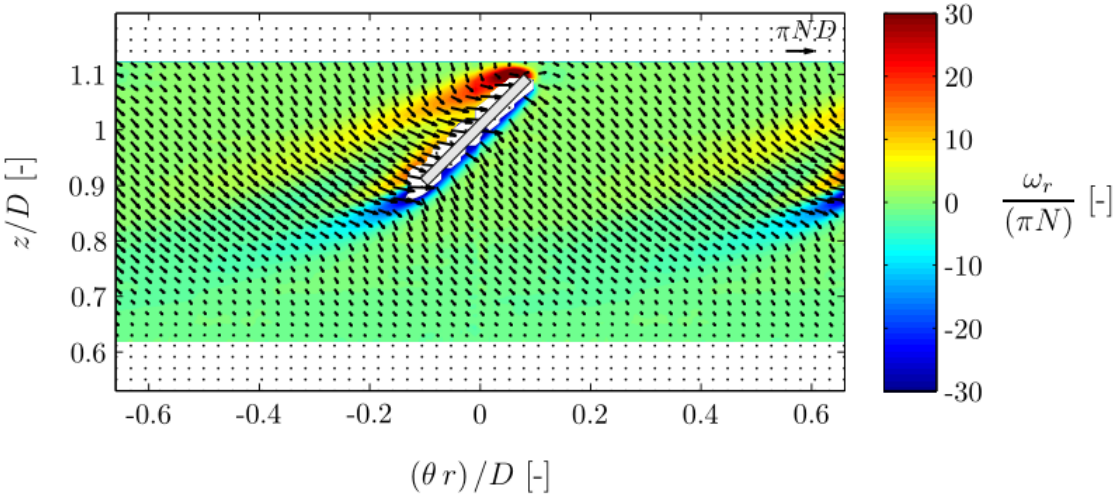

(b)

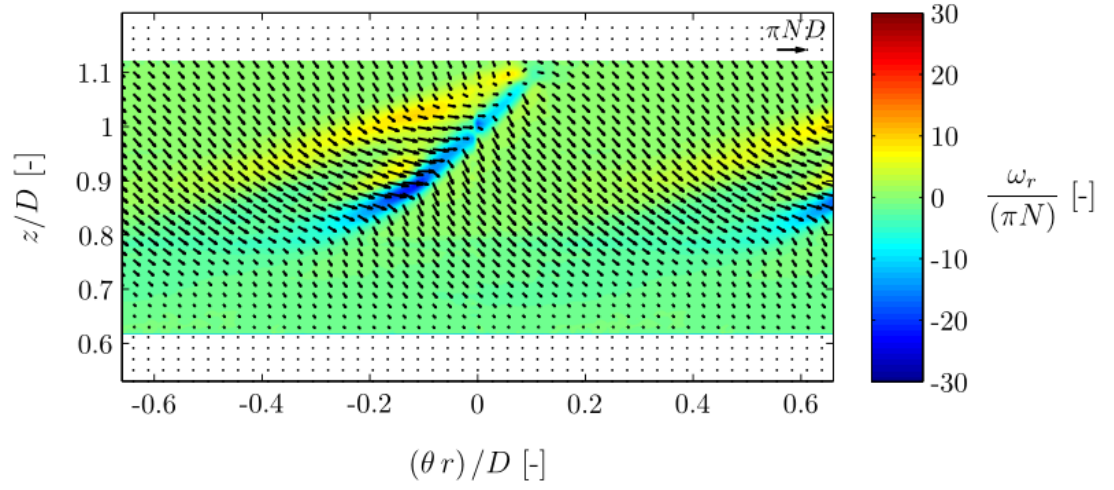

(c)

Figure 3.6: Phase-resolved vector fields and contour plots of the radial component of the vorticity, ω_r, for N = 166 rpm, in different azimuthal planes: (a) r/D = 0.428; (b) r/D = 0.5; (c) r/D = 0.531.

3.4.2 Three-Dimensional Visualization of Trailing Vortices

Iso-vorticity surfaces were used to provide a three-dimensional visualization of trailing vortices generated in the wake of a four-bladed pitched impeller operating in laminar conditions. Choosing suitable levels in the contour of the radial vorticity, the shape of the two counter-rotating vortices was outlined, and it is shown in Figure 3.7, where the red vortex is associated to values of $\omega_r /(N\pi)$ > 7.5, and the blue one to $\omega_r /(N\pi)$ < -7.5.

Trough the three-dimensional view, all the observation made in the previous section are validated, and a clearer understanding of how the vortices spatially develop along the flow is achieved.

Considering the tangential vorticity, the estimation of iso-surfaces at $\omega_\theta /(N\pi)$ = 5.5, revealed the presence of another swirling structure in the flow, depicted in green in Figure 3.7 with characteristics similar to trailing vortices occurring in the wake of a PBT working under turbulent regime (Schafer et al., 1998, Roy et al., 2010). Nevertheless, the phase-resolved analysis of the flow on vertical planes, pointed out that the maximum value of the tangential vorticity was considerably lower than the radial one, at any value of the azimuthal coordinate (see Section 3.4.1 - Ensemble and phase-averaged flow fields). Therefore, the analysis of the tangential vortex wasn't extended, as its influence on the flow was considered minor to that exerted by the two radial swirling structures, which were further investigated.

In Figure 3.8 a visualization of the axes of the two vortices is provided. Here, the red and blue starred symbols represent the center of respectively the upper and lower vortex, computed by vorticity weighted averages over each azimuthal plane. The black axes were obtained through a three-dimensional linearization of the calculated points, and show in both cases a clear radial trend. As the two counter-rotating flow structures have very similar characteristics, only the analysis of the lower vortex is further reported, for brevity of presentation.

The normalized coordinates of the vortex axis (z/D, θ) vary with r/D in the manner shown in Figure 3.9 a-b. Along the entire vortex path, the axial distance of the center is practically constant, and assumes a value of z/T = 0.865. Even the tangential locus doesn't vary considerably, ranging from 22° to 17° for all the radial locations considered, and attesting that the vortex axis follows quite closely a radial path.

At last, a value around 30 % of the height of the blade is found at any r/D for the vortex radius, r^*, calculated considering iso-vorticity surfaces at $\omega_r /(N\pi)$ = -7.5 (Figure 3.9 c). This value corresponds to r^* = 0.06 D.

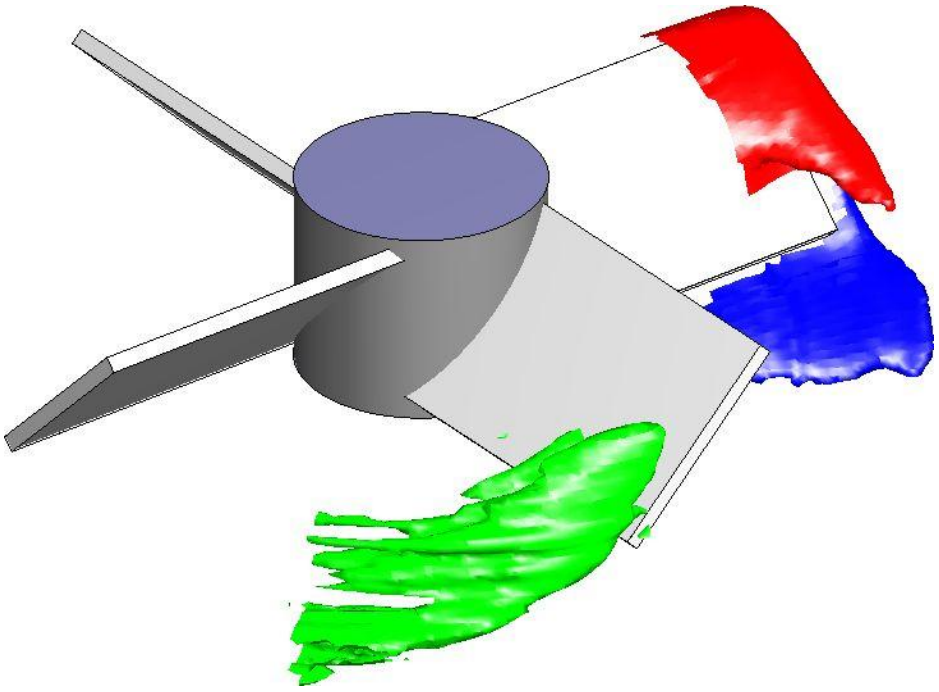

Figure 3.7: Visualization of the trailing vortices behind the impeller blades, by mean of iso-vorticity contours drawn for the values: $\omega_r /(N\pi)$ = ±7.5 (red and blue iso-surfaces) and for $\omega_\theta /(\pi N)$ = 5.5 (green iso-surface).

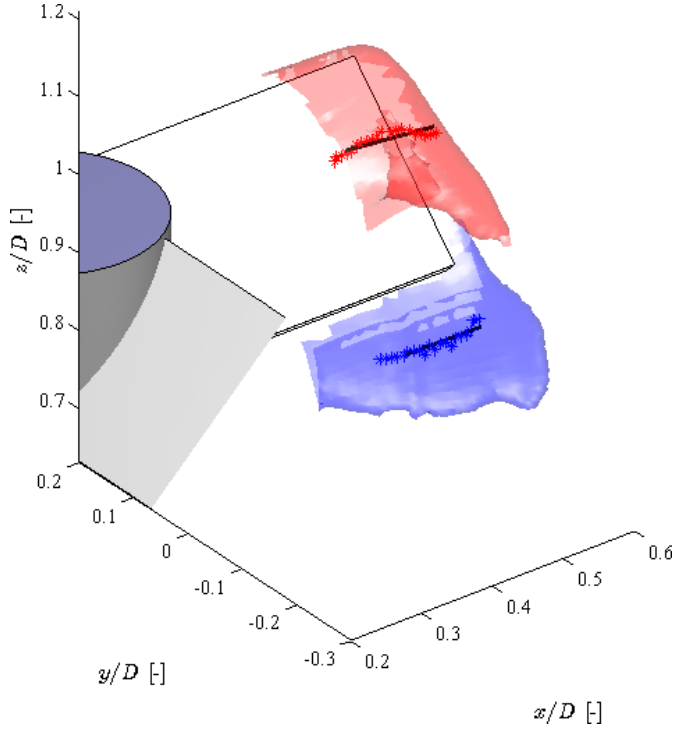

Figure 3.8: Analysis of the vortex structures characterized by | $\omega_r /(N\pi)$ | ≥ +7.5: axis identification.

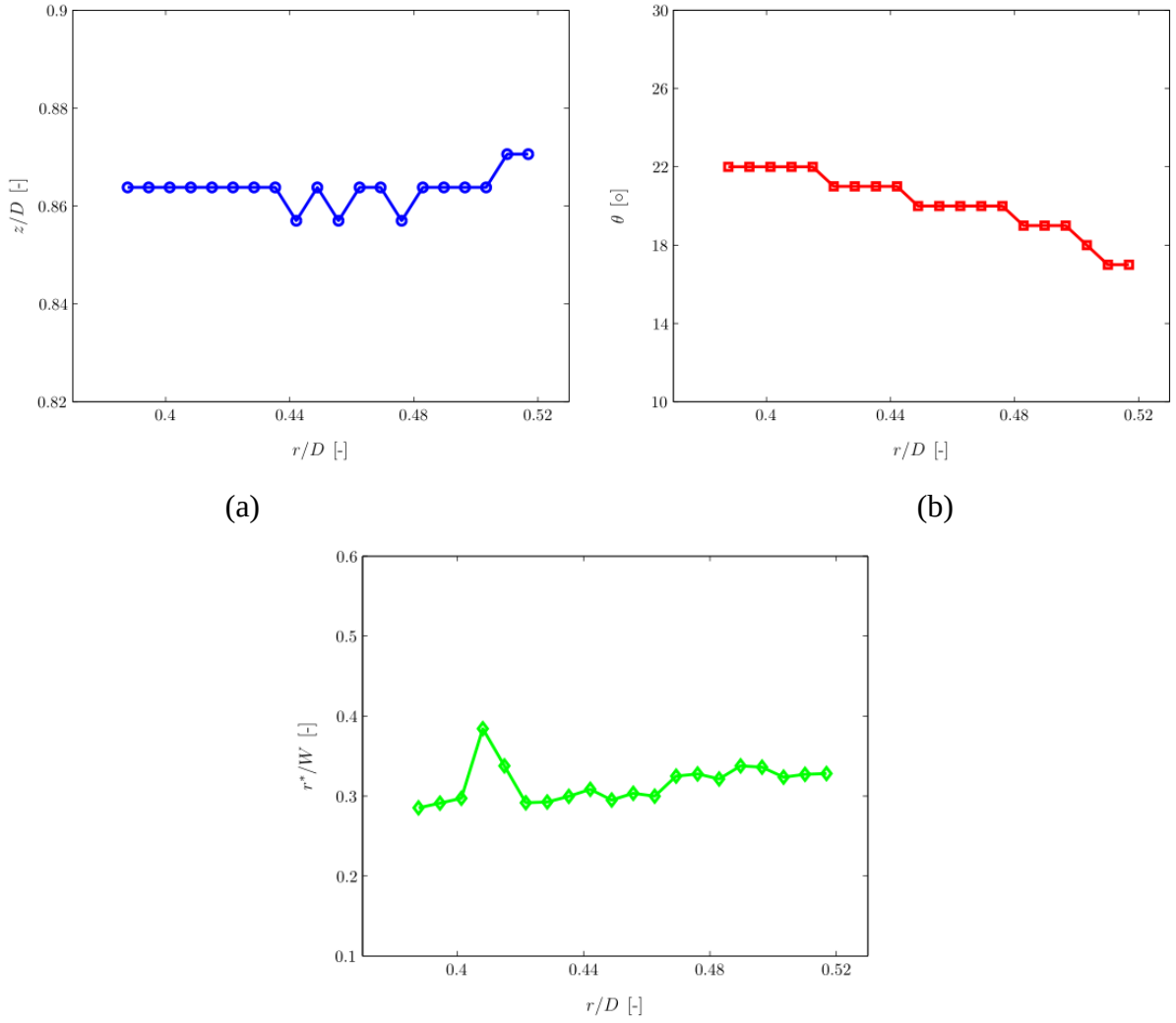

Figure 3.9: Locus and geometrical characterization of the lower trailing vortex axis: (a), (b) variation of the normalized axial and azimuthal coordinates of the vortex axis, *z/D* and θ, with the radial coordinate *r/D*; (c) variation of the vortex radius normalized with the blade height, *r*/W*, with *r/D*.

3.4.3 Principal Strain Rates

To understand the strain and deformation dynamics occurring in the core of trailing vortices, the principal components of the deformation rate tensor, S_{ii}*, were assessed. Their directions of action were estimated through the analysis of two angular parameters, δ_i^* and γ_i*, which indicate the orientation of each principal eigenvector, with respect to the radial and tangential axes (see Section 3.3 - Theoretical Background). As the value of both angles varies in any location, a statistical approach was applied to determine which directions were more likely to be associated with each principal strain rate in the flow region considered. In Figure 3.10 a-e, the blue histograms show the probability density functions of δ_i^* and γ_i* for points with $\omega_r/(\pi N) \leq -7.5$, so located in the core of the lower trailing vortex. In the images, a red labeling is applied to bars which contributes to a probability of 50 % around the peak of the histogram, and is used as a visual indicator of the accuracy in the angle estimation. Figure 3.10 a and c show that in the flow region considered, δ_1* and δ_3* are both likely to assume values around 90° , meaning that the first and third principal component of the deformation rate tensor, are with good probability perpendicular to the radial direction, and lie on the azimuthal plane $(\theta - z)$.

The missing direction can be easily determined considering that the three principal eigenvectors are mutually orthogonal, and therefore the one corresponding to S_{22}* should be orientated radially ($\delta_2^* = 0$). Looking at Figure 3.10 b, the value $\delta_2^* \approx 18°$ can be identified, however the mismatch with the expected result is considered acceptable, given that the graphs refer to probability distributions, and are affected by a certain experimental and computational error.

Histograms in Figure 3.10 d, and e show the orientation of the eigenvectors associated S_{11}* and S_{33}* with respect to the tangential direction, and reveal that as awaited, the two strains are perpendicular, being γ_1* (≈ 30°) and γ_3* (≈ 65°) approximately complementary angles.

To better comprehend the probability distributions just described, the correlation between each angle, δ_i*, and the radial vorticity was investigated for all the points of measurement with $\omega_r < -7.5$, and is shown in Figure 3.11 a-b for the case of δ_3*. In the first image (Figure 3.11 a), the colour coding reflects the intensity variation of the strain rate, S_{33}* , and reveals that locations of highest vorticity are associated to highest strain rate, and to values of δ_3* almost equal to 90° . As the vorticity decreases, S_{33}* does, and the angle scatter grows.

In Figure 3.11 b, the absolute distance of each point from the vortex axis, $\Delta y/D$, is investigated, and associated to symbols of hues varying from blue to red. Despite the larger scatter, the colour-coded correlation shows that the angle δ_3* tends to 90° for locations closer to the vortex axis. As in the

core of trailing vortices the eigenvectors corresponding to S_{11}* and S_{33}* were found perpendicular to the radial direction, their analysis continued over azimuthal planes.

Contour plots of the first and third principal strain rates are shown in Figure 3.12 a and b for a radial position r/D = 0.48, and show that S_{11}* is associated to compression and S_{33}* to stretching of the fluid. In the whole field of view the magnitude, $|\ S_{ii}^*/(\pi N)\ |$, of the two eigenvalues is comparable, being very modest everywhere but close to the impeller blade and in the trailing vortices region, where it becomes considerably higher, with values up to $|\ S_{ii}^*/(\pi N)\ | \approx 24$. Lines locally tangent to the eigenvectors corresponding to S_{11}* and S_{33}* were identified, and are depicted separately in Figure 3.12 a and b in the core of trailing vortices. The white lines (Figure 3.12 a), provide a visualization of the direction of compression undergone by the fluid, whereas the black ones (Figure 3.12 b), suggest the orientation along which the principal stretching mechanism operates in the flow. Focusing on the lower vortex region, angles of ≈ 35° and ≈ 60° can be visually identified between the x-axis and respectively the compression and stretching-lines, validating the result of the statistical analysis previously made on $\gamma_{1,3}$* (Figure 3.10 d-e).

To provide a summary view of the principal strain dynamics occurring in the core of trailing vortices, a map of the radial vorticity associated with lines of compression and stretching, is shown in Figure 3.12 c for points with $|\omega_r/(\pi N)| \geq +7.5$. Observing the image, it is worth noting that the directions of action of S_{11}* and S_{33}* reported in the lower trailing vortex, are perpendicular to those identified in the upper one. The contour plot of S_{22}* is not shown here, as it assumes values close to zero in the whole flow field investigated. The maximum shear stress experienced by the fluid inside the stirred reactor was calculated using Equation 3.6:

$$\tau^*_{max} = \frac{|S^*_{11}| + |S^*_{33}|}{2} \tag{3.6}$$

and it is visualized in Figure 3.13 in the azimuthal plane at r/D = 0.48. Observing the image, it can be noticed that $\tau^*_{max}/(\pi N)$ assumes a relevant intensity only in the region of the flow where trailing vortices occur, reaching a maximum value of $\tau^*_{max}/(\pi N)$ = 20. Figure 3.13 displays also the directions of action of the maximum shear stress, which were estimated considering that by definition τ^*_{max} is oriented at 45° with respect to the principal strains.

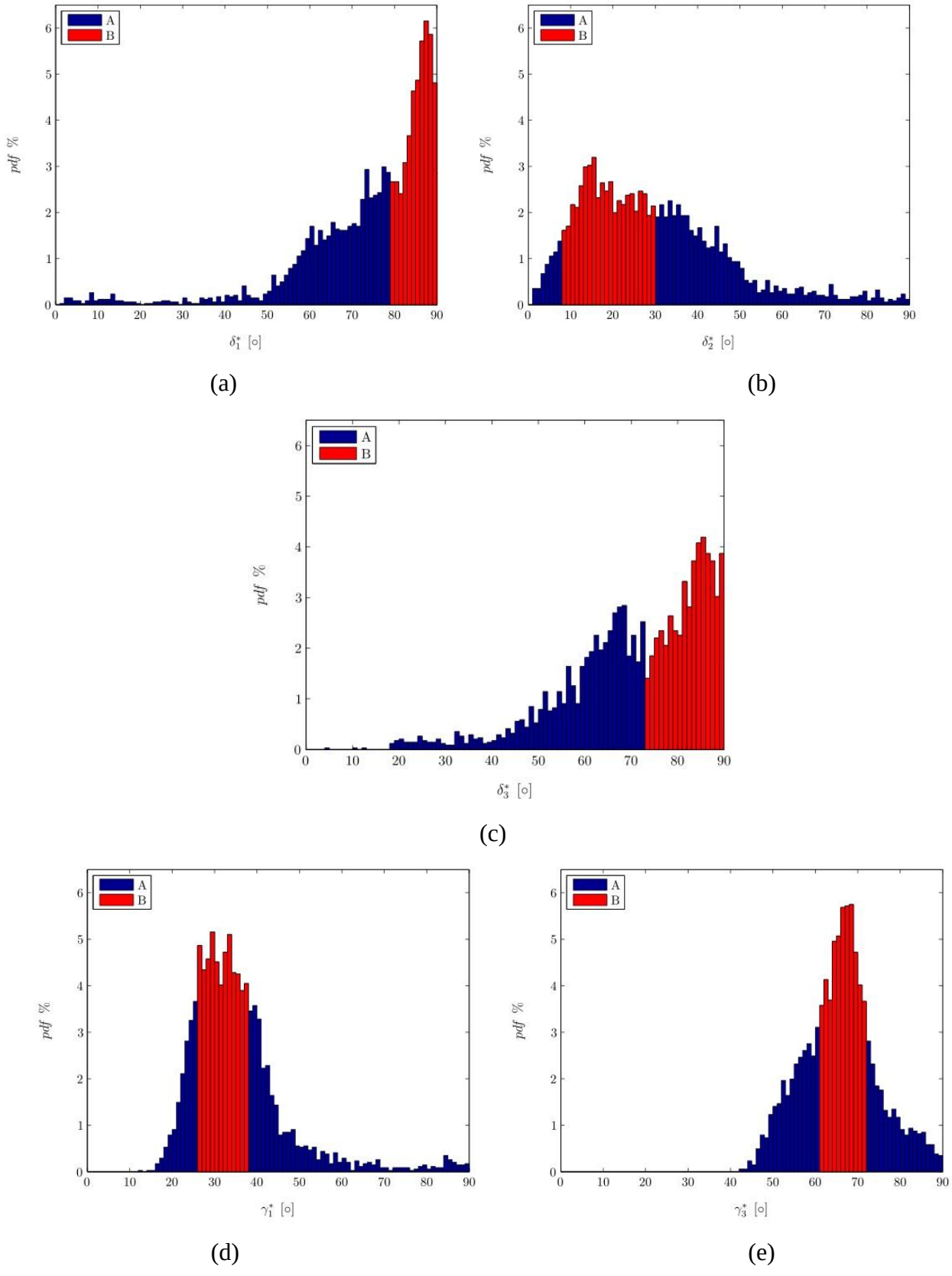

(a) (b)

(c)

(d) (e)

Figure 3.10: Probability density functions of δ_i* and γ_i* , for point with $\omega_r/(\pi N) \leq -7.5$: (a) δ_1*; (b) δ_2*; (c) δ_3*; (d) γ_1* ; (e) γ_3*.

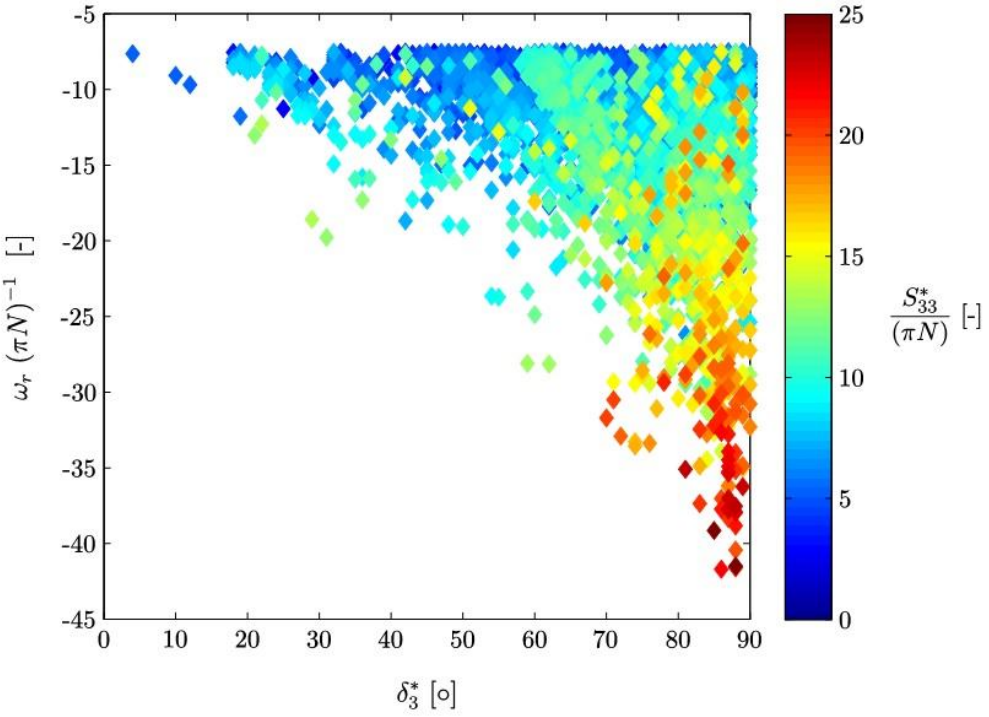

(a)

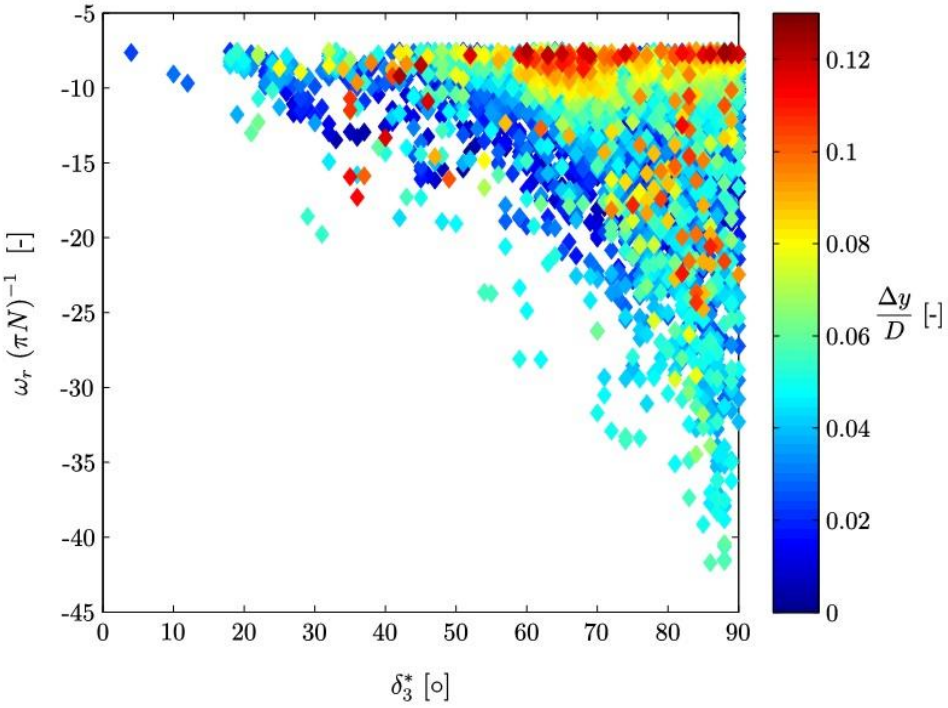

(b)

Figure 3.11: Color-coded correlation between (δ_3* - ω_r) points located in the core of the lower trailing vortex, and: (a) the eigenvalue, S_{33}* ; (b) the absolute distance of each point from the vortex axis, $\Delta y/D$.

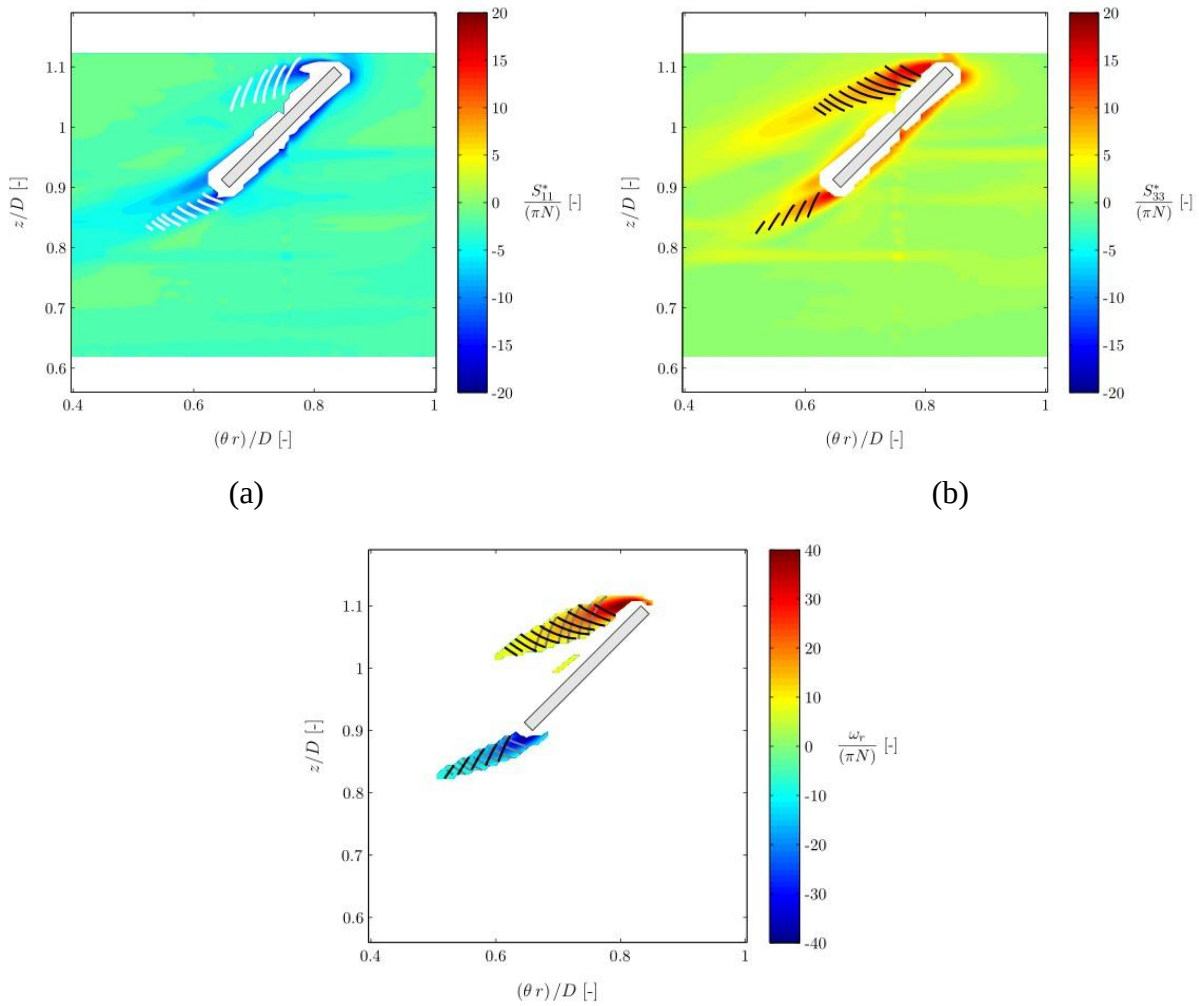

Figure 3.12: Contour plots of the principal components of the strain rate tensor, S_{ii}*, in the azimuthal plane *r/D* = 0.483, and visualization of the strains directions in the core of trailing vortices: (a) map of S_{11}*, and lines locally tangent to the corresponding eigenvector; (b) map of S_{33}*, and lines locally tangent to the corresponding eigenvector; (c) map of the radial vorticity ω_r , and lines associated to S_{11}* and S_{33}*.

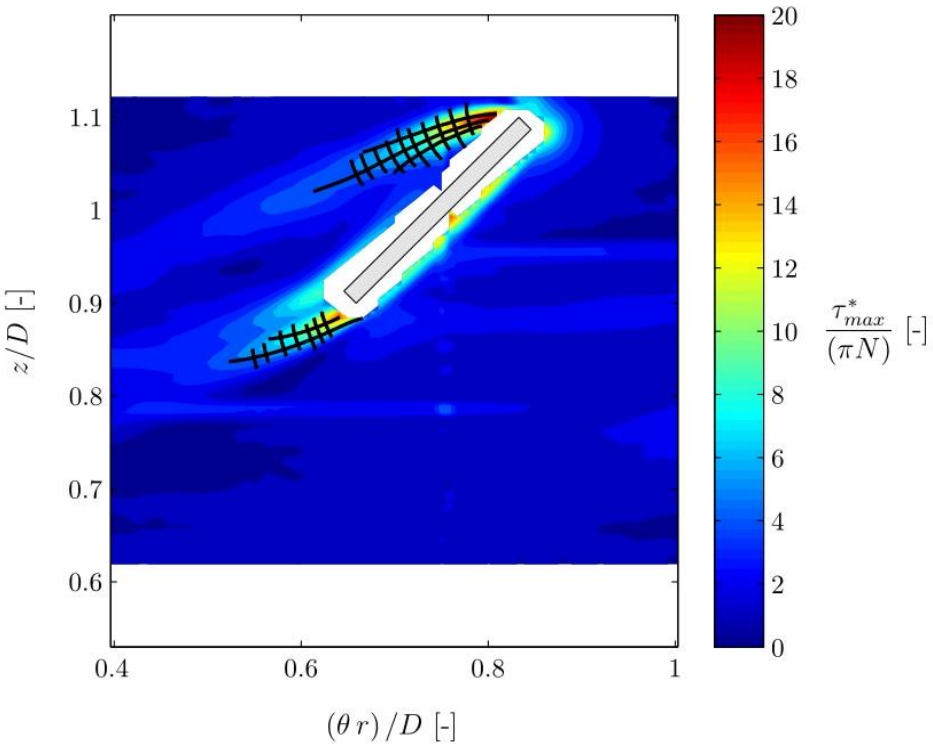

Figure 3.13: Contour plot of the maximum shear stress, $\tau^*_{max}/(\pi N)$, in the azimuthal plane r/D = 0.483, and visualization of its main direction of action in the core of the trailing vortices.

3.4.4 Surface Deformation Rate

Bouremel et al. (2009)'s approach was replicated to investigate the total surface deformation rate, η'_{tot} , undergone by a virtual fluid element located in each point of the measurement volume. The analysis was computed for a particle of initial spherical shape and diameter D_s = 0.068 D, which corresponds to approximately 50 % of the size of the lower trailing vortex ($D_{tv} \approx 0.12\ D$). Figure 3.14 a shows the axial profile of η'_{tot} at r/D = 0.483 and θ = 70° , together with the tangential vorticity (black-dotted line), which provides an indication of the vortex core location. Given that a surface deformation process doesn't involve a volume variation, and that the sphere is the shape which minimizes the surface area at constant volume, a positive value of the surface deformation rate is expected at any location considered. However, η'_{tot} assumes negative values for 0.75 < z/D < 0.82, and 1.05 < z/D < 1.08 (Figure 3.14 a), meaning that a reduction of the particle external surface seems to occur at certain positions. The mismatch with the expected result can be explained considering Figure 3.14 b, which shows that the actual volume variation experienced by the particle during the deformation process differs considerably from zero in most of the axial locations considered. dV/V assumes a value up to 0.94 at z/D = 0.09, and this reveals that the hypothesis of constant volume transformation is actually lost. Analyzing further Figure 3.14 a and b, a linear relation can be found between the surface deformation rates and the volume variation values, with a proportionality coefficient, 2/3 , being in accordance with theoretical considerations on the sphere geometry.

Considering the link between the two quantities, the volume change locally experienced by the virtual particle is used as an estimation of the error affecting the surface deformation rate, and is displayed in Figure 3.14 a as a red errorbar associated to the each value of η'_{tot}. The uncertainties laying behind these results surely arise from the estimation of S_{nn} , the deformation rate tensor locally perpendicular to the particle surface, and used to compute η'_{tot} (see Equation 3.5). In fact, the tensor is calculated through velocity derivatives affected by a certain error (see Section 3.3 - Theoretical Background), which is further enhanced when the interpolation over the sphere surface is computed. As the negative values appearing in the profile of η'_{tot} may be misinterpreted (Figure 3.14 a), a better visualization of the surface deformation dynamics encountered by the spherical particle is provided in Figure 3.14 c. Here, the axial profile of the absolute value of the surface deformation rate, $|\ \eta'_{tot}\ |$, is displayed at r/D = 0.483 and θ = 70 ° , whereas the errorbar refers again to the volume deformation experienced by the sphere, and provides an estimation of the error affecting the data displayed.

The influence of the particle size on the surface deformation rate is investigated considering three virtual spheres of increasing diameter: D_s/D = 0.027, 0.054, 0.068. Figure 3.15 a shows axial profiles of $|\eta'_{tot}|$ computed for different D_s/D, together with the profile of the radial vorticity, $\omega_r/(\pi N)$. The location chosen is the same considered in the previous analysis (r/D = 0.483 and θ = 70°). Inspecting the figure, it can be concluded that bigger particles are subjected to lower surface deformation rates, to the extent that the maximum of $|\eta'_{tot}|$ for D_s/D = 0.027 is twofold greater than that experienced by the biggest sphere (D_s/D = 0.068). The same trend is reported in Figure 3.15 b, where the volume variation associated with the surface deformation process is displayed for different D_s/D. As the diameter increases, dV/V decreases, meaning that the hypothesis of constant volume transformation is being approached, and that the error affecting $|\eta'_{tot}|$ is lower.

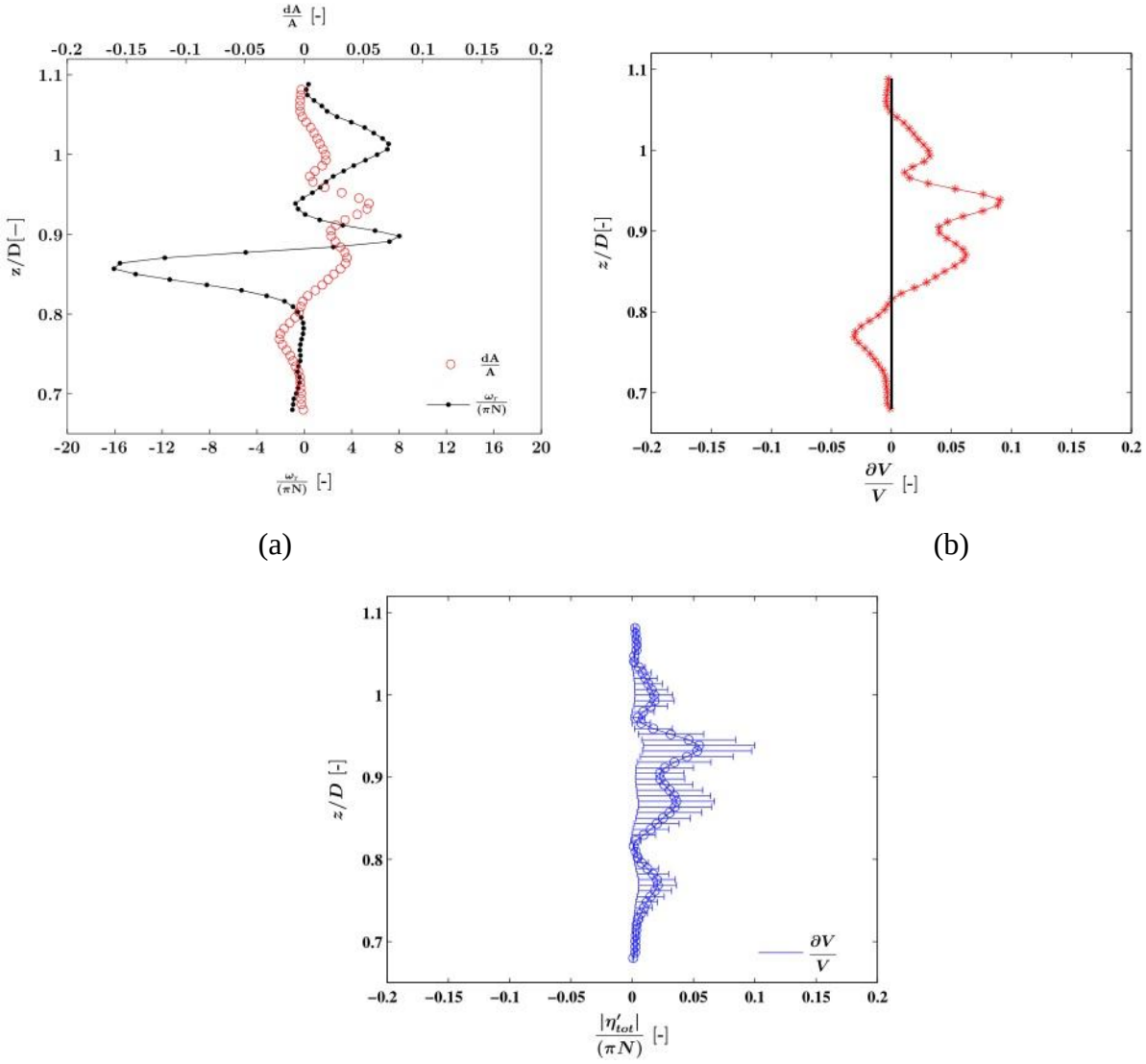

(a) (b)

(c)

Figure 3.14: Deformation dynamics encountered by a virtual spherical particle of diameter D_s = 0.068 D, located at (r/D = 0.483 , and θ = 70 °): (a) axial profile of the total surface deformation rate, η'_{tot} , and corresponding values of $\omega_\theta /(\pi N)$; (b) volume variation experienced by the particle during the process, dV/V; (c) axial profile of the absolute total surface deformation rate, $|\eta'_{tot}|$.

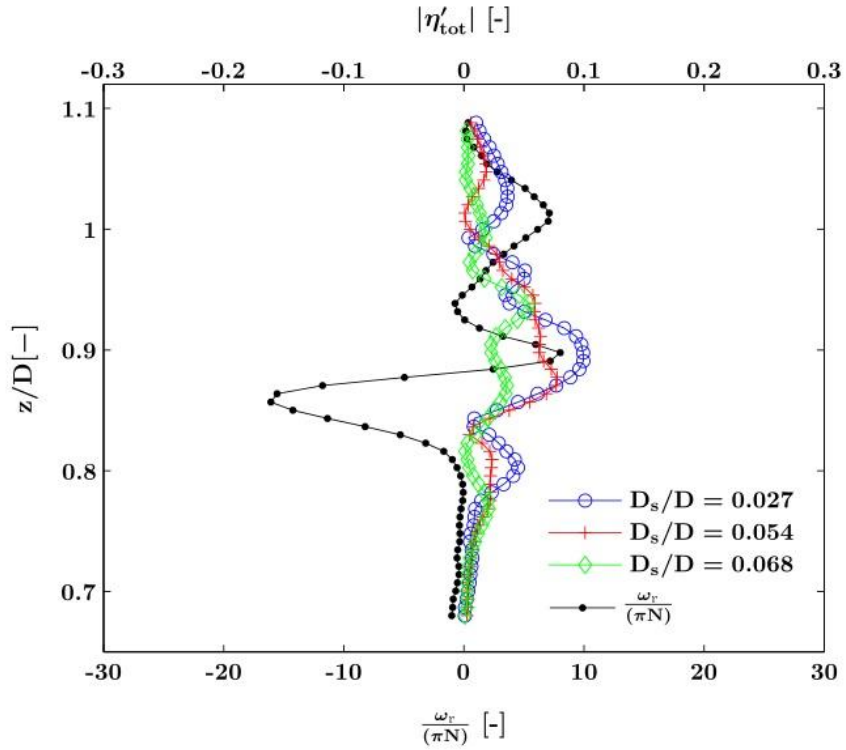

(a)

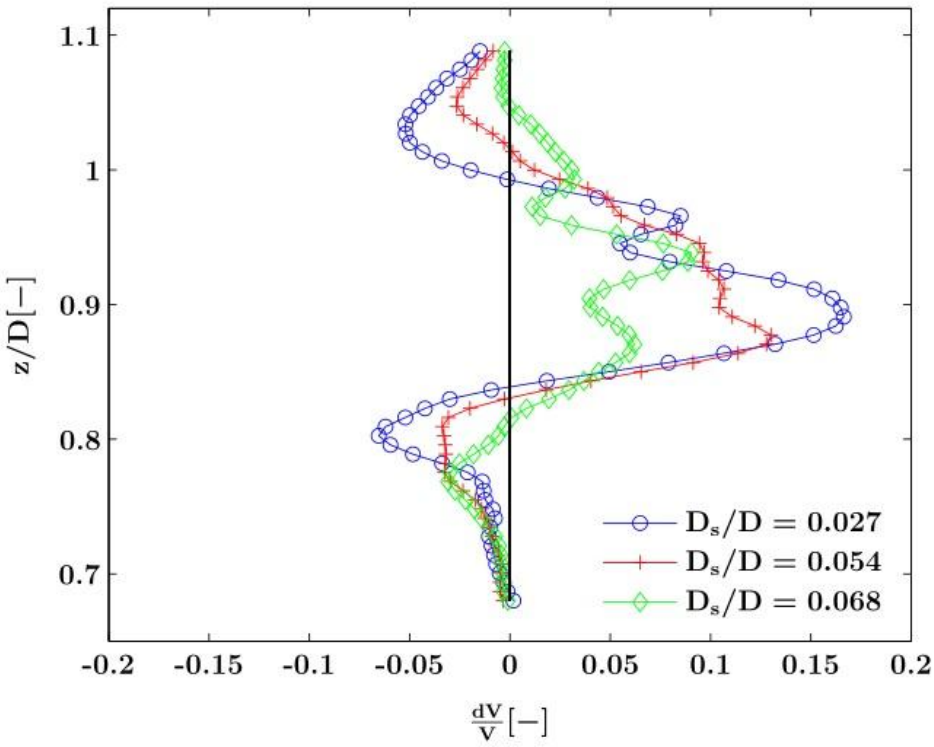

(b)

Figure 3.15: Influence of the sphere dimensions on the deformation dynamics of a spherical particle located at (r/D = 0.483 , and θ = 70°): (a) axial profiles of the absolute total surface deformation rate, $|\eta'_{tot}|$, and corresponding values of $\omega_\theta/(\pi N)$, for three different sphere diameters; (b) volume variation experienced by particles of different dimensions during the process, dV/V.

3.5 Conclusions

In the present work the hydrodynamics generated within a four-bladed PBT-stirred tank working under laminar regime were investigated in great detail. An LDA system was employed to obtain accurate ensemble and angle-resolved velocity measurements, while data analysis allowed to achieve a thorough characterization of the main flow structures developing within the system.

Analyzing the mean flow over vertical planes, the single-loop flow pattern typically induced by an axial turbine was identified. However, due to the low value of Reynolds number, the axial stream did not reach the bottom of the tank, but rose gradually for decreasing values of *z/D*, until it appeared totally radial. The observation of the flow field and radial vorticity levels on azimuthal planes revealed the occurrence of two trailing vortices, definite swirling structures that start growing at the tips of each blade, and develop along the tangential coordinate, giving rise to almost parallel but counter rotating wakes of decreasing strength. Iso-vorticity surfaces were used to provide a three-dimensional visualization of these structures, while vorticity weighted averages over azimuthal planes were computed to identify the locii of the vortices axes.

At this stage, the strain and deformation dynamics occurring in the core of the trailing vortices were investigated: the deformation rate tensor was calculated, and its principal components were assessed. The direction of action of the principal strain rates was estimated considering the angles developing between the radial and tangential axes, respectively, δ_i^* and γ_i^*, and the eigenvectors of S_{ii}^*. A probability distribution of the two angular parameters revealed that it's very likely that the first and third component of the deformation rate tensor (S_{11}^* and S_{33}^*) are perpendicular to the radial direction, and therefore lie on the azimuthal plane. Consequently, the missing direction is oriented radially.

Contour plots of S_{11}^* and S_{33}^* were obtained over azimuthal planes, and showed that S_{11}^* is associated to compression and S_{33}^* to stretching of the fluid. Particularly, it was observed that the magnitude of the two eigenvalues was comparable and very modest everywhere, a part from the area close to the impeller blade and to the vortices. Then, a visualization of the directions of compression, stretching and maximum shear stress, τ^*_{max} , was provided in the core of trailing vortices.

At last, the total surface deformation rate, η'_{tot} , undergone by a virtual fluid element located in the measurement volume was assessed. Particles of initial spherical shape and increasing diameters were considered, and it was found that bigger particles are subjected to lower surface deformation rates.

3.6 References

Ali, A.M., Yuan, H.H.S., Dickey, D.S., Tatterson, G.B., 1981. Liquid dispersion mechanisms in agitated tanks .1. pitched blade turbine. Chemical Engineering Communications 10, 205–213.

Alvarez, M.M., Zalc, J.M., Shinbrot, T., Arratia, P.E., Muzzio, F.J., 2002. Mechanisms of mixing and creation of structure in laminar stirred tanks. AIChE J 48, 2135–2148.

Aubin, J., Mavros, P., Fletcher, D.F., Bertrand, J., Xuereb, C., 2001. Effect of axial agitator configuration (up-pumping, down-pumping, reverse rotation) on flow patterns generated in stirred vessels. Chemical Engineering Research and Design 79, 845–856.

Bakker, A., Myers, K.J., Ward, R.W., Lee, C.K., 1996. The laminar and turbulent flow pattern of a pitched blade turbine. Chemical Engineering Research and Design 74, 485–491.

Bouremel, Y., Yianneskis, M., Ducci, A., 2009. Three-dimensional deformation dynamics of trailing vortex structures in a stirred vessel. Industrial & Engineering Chemistry Research 48, 8148–8158.

Chapple, D., Kresta, S.M., Wall, A., Afacan, A., 2002. The effect of impeller and tank geometry on power number for a pitched blade turbine. Chemical Engineering Research and Design 80, 364–372.

Davidson, P.A., 2004. Turbulence an introduction for scientist and engineers. Oxford University Press.

Harvey, A.D., West, D.H., Tufillaro, N.B., 2000. Evaluation of laminar mixing in stirred tanks using a discrete-time particle-mapping procedure. Chemical Engineering Science 55, 667–684.

Hockey, R.M., Nouri, J.M., 1996. Turbulent flow in a baffled vessel stirred by a 60 degrees pitched blade impeller. Chemical Engineering Science 51, 4405–4421.

Jaworski, Z., Dyster, K.N., Nienow, A.W., 2001. The effect of size, location and pumping direction of pitched blade turbine impellers on flow patterns: LDA measurements and CFD predictions. Chemical Engineering Research and Design 79, 887–894.

Khan, F.R., Rielly, C.D., Brown, D.A.R., 2006. Angle-resolved stereo-PIV measurements close to a down- pumping pitched-blade turbine. Chemical Engineering Science 61, 2799–2806.

Khan, F.R., Rielly, C.D., Hargrave, G.K., 2004. A multi-block approach to obtain angle-resolved PIV measurements of the mean flow and turbulence fields in a stirred vessels. Chem. Eng. Tech. 27, 264–269.

Khopkar, A.R., Aubin, J., Xuereb, C., Le Sauze, N., Bertrand, J., Ranade, V.V., 2003. Gas-liquid flow generated by a pitched-blade turbine: Particle image velocimetry measurements and

computational fluid dynamics simulations. Industrial & Engineering Chemistry Research 42, 5318–5332.

Kresta, S.M., Wood, P.E., 1993. The flow field produced by a pitched blade turbine: characterization of the turbulence and estimation of the dissiaption rate. Chem. Eng. Sci. 48, 1761 – 1774.

Kumaresan, T., Joshi, J.B., 2006. Effect of impeller design on the flow pattern and mixing in stirred tanks. Chemical Engineering Journal 115, 173–193.

Lamberto, D.J., Muzzio, F.J., Swanson, P.D., Tonkovich, A.L., 1996. Using time-dependent rpm to enhance mixing in stirred vessels. Chemical Engineering Science 51, 733.

Nouri, J., Whitelaw, J.H., 1990. Flow characteristics of stirred reactors with Newtonian and Non-Newtonian Fluids. AIChE J. 36, 627.

Ottino, J.M., 1989. The kinematics of mixing: stretching, chaos, and transport. Cambridge University Press.

Ranade, V.V., Joshi, J.B., 1989. Flow generated by pitched blade turbines .1. measurements using laser doppler anemometer. Chemical Engineering Communications 81, 197–224.

Roy, S., Acharya, S., Cloeter, M.D., 2010. Flow structure and the effect of macro-instabilities in a pitched-blade stirred tank. Chemical Engineering Science 65, 3009–3024.

Schäfer, M., Yianneskis, M., Wächter, P., Durst, F., 1998. Trailing vortices around a 45 degrees pitched-blade impeller. AIChE J. 44, 1233–1246.

Sheu, Y.H.E., Chang, T.P.K., Tatterson, G.B., Dickey, D.S., 1982. A 3-dimensional measurement technique for turbulent flows. Chemical Engineering Communications 17, 67–83.

Tatterson, G.B., Stanford, T.G., 1981. Liquid dispersion mechanisms in agitated tanks .3. low viscosity discrete phase into high-viscosity continuous phase. Chemical Engineering Communications 11, 371– 376.

Tyagi, M., Roy, S., Harvey, Albert D., I., Acharya, S., 2007. Simulation of laminar and turbulent impeller stirred tanks using immersed boundary method and large eddy simulation technique in multi-block curvilinear geometries. Chemical Engineering Science 62, 1351–1363.

Unadkat, H., Rielly, C., Hargrave, G., Nagy, Z., 2009. Application of fluorescent piv and digital image analysis to measure turbulence properties of solid-liquid stirred suspensions. Chemical Engineering Research and Design 87, 573–586.

Villermaux, J., 1986. Micromixing phenomena in stirred reactors. Encyclopedia of Fluid Mechanics 2, 707–771.

Woziwodzki, S., Jedrzejczak, L., 2011. Effect of eccentricity on laminar mixing in vessel stirred by double turbine impellers. Chemical Engineering Research and Design 89, 2268–2278.

Yianneskis, M., Popiolek, Z., Whitelaw, J.H., 1987. An experimental study of the steady and unsteady flow characteristics of stirred reactors. J. Fluid Mech. 175, 537 – 555.

4 Prediction of fluid dynamic instabilities of low liquid height-to-tank diameter ratio stirred tanks

4.1 Introduction

Mixing is a crucial unit operation in the chemical, biochemical and allied industries. It is often performed in mechanically stirred tanks, due to their ease of construction, cleanness and versatility of operation. A wide variety of stirred tanks' design are adopted in the industrial practice, depending on the process main requirements: blending of miscible liquids, dispersion of bubbles or droplets into a liquid phase, solids suspension, chemical or biological reactions, just to mention a few examples. In any case, it is well known that the performances of the mixing equipment are strongly dependent on the three-dimensional flow generated by the stirrer, as it affects the dispersed phase distribution, heat and mass transfer as well as the chemical reactions involved in the operation (Derksen, 2003).

Thorough experimental and computational investigations have been carried out in the past 50 years on fluid mixing, leading to a deep knowledge of the flow and the mixing dynamics taking place in baffled stirred tanks of standard geometrical features (Brown et al., 2004) (tank height-to-tank diameter ratio, $H/T \geq 1$, and impeller diameter to tank diameter ratio, $1/3 \leq D/T \leq 1/2$). Attention has been also devoted to unbaffled stirred tanks of standard geometry, which are often adopted in pharmaceutical and food processes (Hörmann et al., 2011; Assirelli et al., 2008), in bioreactions with shear sensitive cells (Aloi and Cherry, 1996), for very viscous fluids (Lamberto et al., 1996) for carrying out fast chemical reactions (Rousseaux et al., 2001). As a difference with baffled tanks, the prevailing fluid flow of unbaffled cylindrical vessels is tangential, and, depending on impeller speed and liquid height, a central vortex may expand from the free surface, whose depth has to be carefully monitored in order to avoid impeller flooding and gas entrainment. The local flow field characterization inside unbaffled tanks has revealed that axial impellers tend to lose most of their typical pumping action, and that the majority of the kinetic energy of the fluid is consumed along the tangential direction (Armenante et al., 1997; Alcamo et al., 2005).

Low tank height-to-tank diameter ratios and/or low liquid height-to-tank diameter ratios for vessels either provided or not provided with baffles are also adopted for important industrial operations in the pharmaceutical industries (Motamedvaziri and Armenante, 2012) and in anaerobic bio-processes (Montante and Paglianti, 2015). The available knowledge gained so far on the fluid flow and the

mixing dynamics encountered in reactors of this type is quite narrow. Further investigations would help improving design rules and operating conditions, since general predictive equations obtained in standard tanks cannot be applied even to calculate basic parameters, such as power consumption, flow number and mixing time, being the hydrodynamics produced by the impellers-tank interactions completely different. The gap of information is worth to be filled, due to the industrial interest on these configurations and the evidence gained in previous investigations of their quite complex fluid dynamic behavior (Montante and Paglianti, 2015), including the significant oscillations of the liquid free surface and the instabilities of the flow, whose quantitative characterization has never been reported so far.

In the detailed investigations of the fluid dynamic behavior of stirred tanks, temporal mean flow variations called macro-instabilities (MIs) have been observed for specific ranges of conditions and/or locations. The MIs, whose frequency is much lower than the impeller blade passing frequency, can strongly affect the mean velocity and r.m.s. velocity fluctuations (Nikiforaki et al., 2003), the mixing performances (Guillard et al., 2000), mass and heat transport, the mixing times (Ducci and Yianneskis, 2007). MIs were found to occur in stirred tanks from different origins: a) the change of flow patterns due to the impeller clearance (Kresta and Wood, 1993; Galletti et al., 2003); b) the flow regime transition induced by a change of the Reynolds number (Galletti et al., 2004); c) the occurrence of precessional vortices around the vessel axis (Nikiforaki et al., 2003; Yianneskis et al., 1987); d) the instability of the impeller jet (Paglianti et al., 2006). The instabilities of the mean flow have been investigated for stirred vessels of standard geometrical proportions provided or not provided with baffles and with a fill ratio equal or close to one. Different mechanisms and characteristic instabilities may be expected depending on the geometry, as shown among others by Galletti et al. (2009) in the case of unbaffled stirred tanks of different shaft eccentricities. To the best of our knowledge, the flow instabilities in partially filled stirred tanks with low height-to-tank diameter ratio have never been investigated systematically, either by experimental or numerical techniques. The liquid free surface oscillations in a low height-to-tank diameter ratio model digester have been just visually observed (Montante and Paglianti, 2015), while the free surface shape and the relevant oscillation modes of liquid sloshing in containers have been widely investigated mainly by theoretical approaches (Ibrahim et al., 2001; Ibrahim, 2005). Most of the results have been obtained solving the fluid flow equations under the hypothesis of potential flow (inviscid, incompressible and irrotational) and appropriate boundary conditions to account for the presence of lateral walls, thus determining the free surface flow and the resulting hydrodynamic pressure distribution, forces and moments. Besides, many experimental (Pal et al., 2001; Yang et al., 2015) and computational studies (Okamoto et al., 1990; Rebouillat and Liksonov, 2010) have been carried

out with the aim of determining the main features of liquid sloshing. Recently, the liquid sloshing dynamics encountered in orbital shaken cylinders has been investigated experimentally and interpreted by a potential sloshing model (Reclari, 2013; Reclari et al., 2014). The conclusions drawn so far on the sloshing dynamics in moving or stationary containers of different shapes might be usefully related to the liquid free surface dynamics in the stirred vessels considered in this work (Montante and Paglianti, 2015).

With the specific purpose of identifying the relationship between the liquid free surface dynamics and the fluid flow characteristics of low liquid height-to-tank diameter ratio stirred tanks, detailed velocity measurements by Particle Image Velocimetry (PIV) and frequencies analysis of the dynamic pressure time series collected by a Pitot system are carried out. The liquid free surface influences greatly the entire system fluid dynamics and it may have a relevant impact on the performances of industrial apparatuses of similar geometry.

4.2 Materials and Methods

The experiments were performed in two cylindrical stirred tanks of different dimensions, named T49 and T23 in the followings. The former has been investigated by both PIV and a Pitot system. For the latter, just selected measurements by the Pitot system have been collected for specifically identifying the geometry effect on the flow frequencies. T49, that is shown in Figure 4.1, consists of a low height-to-tank diameter ratio, flat-bottomed, unbaffled cylindrical vessel of diameter, T, equal to 0.49 m and height, H, equal to 0.255 m ($H/T=0.52$). T23 is a flat-bottomed unbaffled cylindrical vessel of diameter, T, equal to 0.232 m and height equal to 0.24 m ($H/T=1.03$). In both cases, the mechanical agitation was provided by two identical Lightnin A310 impellers of diameter, D, equal to 0.098 m, the lower of which was placed at off-bottom clearance, C_1, equal to 0.039 m and at distance from the upper impeller, C_2, equal to 0.088 m. The impellers were mounted on a shaft coaxially with respect to the vessel axis and demineralized water was used as the working fluid.

In T49, three different liquid heights, H_L (0.69 H; 0.80 H; 0.92 H), and fully turbulent rotational Reynolds numbers, Re (from 3.2×10^4 up to 9.6×10^4), were investigated. Two fill ratios lower than one were also considered in T23 (H_L = 0.71 H and 0.83 H).

Only for T49, the ensemble-averaged velocity field was determined by a standard 2D-PIV system in limited portions of a diametrical vertical plane of the vessel, named zone A and zone B in Figure 4.1, in order to account for the strong variations of the flow moving from the impeller region towards the vessel wall.

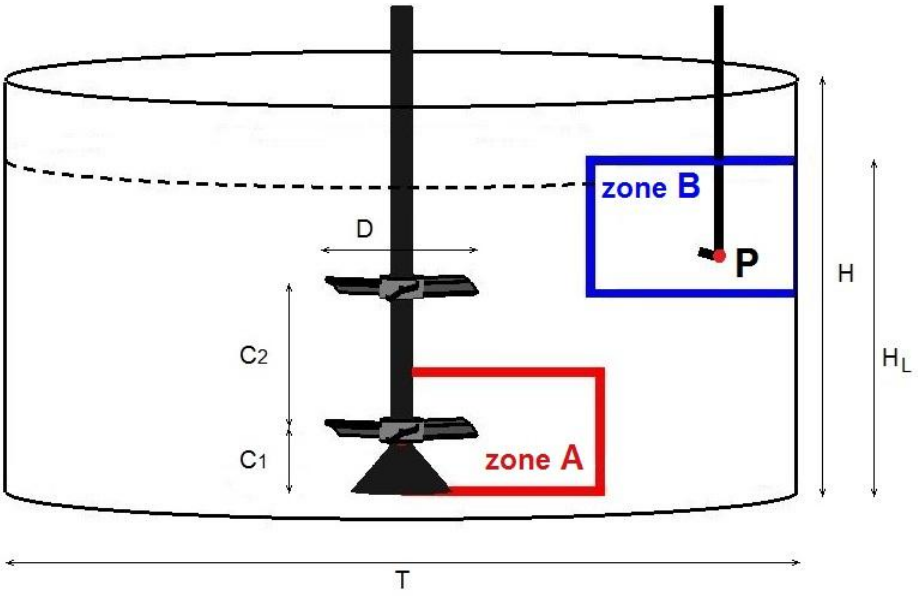

Figure 4.1: Sketch of T49 and location of the PIV and Pitot measurements.

The experimental system included a Litron Nd:YAG laser, emitting light at 532 nm with a maximum frequency of 15 Hz and energy equal to 65mJ, and a HiSense MK II 1344×1024 pixels CCD camera, provided with an optical filter cutting off the light wavelength lower than that emitted by the fluorescent seeding particles. When the lower impeller discharge stream was investigated (‘*zone A*’), the time interval between two laser pulses was experimentally set at Δt = 850 μs for the condition N = 300 rpm, and this value was then proportionally adjusted for all the other rotational speeds considered. Close to the vessel wall (‘*zone B*’), minor variation of the flow and lower velocity magnitudes were detected, therefore a constant value of Δt = 4000 μs was chosen at any impeller speed investigated. The analysis of the instantaneous image pairs was carried out through the use of an adaptive-correlation algorithm, applied on interrogation areas (IA) of initial size 64 x 64 pixel (‘*zone A*’), and 128 x 128 pixel (‘*zone B*’). Two refinement steps together with 50% overlap resulted in final windows of respectively 8 x 8 pixel and 16 x 16 pixel, allowing the reconstruction of the flow field with a spatial resolution of 2 mm in ‘*zone A*’, and of 3.7 mm in ‘*zone B*’. The instantaneous vectors underwent validation algorithms based on the evaluation of the peak heights in the correlation plane and of the maximum value of the velocity magnitude. The statistical convergence of data was checked on both mean velocities and turbulence levels, and the number of image pairs necessary to obtain reliable results was set to 1000. The PIV velocity time series were analyzed in the frequency domain by Fast Fourier transform (FFT) after data resampling, in order to get an initial estimation of the prevailing frequency of the flow.

For an accurate and extensive identification of the characteristic frequencies of the flow in both T49 and T23, dynamic pressure data were recorded on selected locations by a Pitot system. The dynamic pressure was measured by a transducer based on a silica chip and a slim diaphragm of 2.54 mm^2 surface, which was connected to the Pitot tube inserted in the reactors by a lid-port. The signal from the transducer was amplified and the time traces were recorded and transferred to the PC by a data acquisition card controlled by a LabView program. With this technique, a rate of acquisition much higher than that possible with the PIV and a total measurement time long enough to ensure a statistically sufficient number of instability periods contained in the data were adopted. Indeed, the data recordings frequency and the total measurements time were already found to affect the magnitude of the dominant detected frequency (Nikiforaki et al., 2003). For T49, the dynamic pressure time series were measured in a point '*P*' located at the radial distance from the vessel axis, *r*, equal to 0.44 *T* and at a axial distance from the vessel bottom, *z*, of 0.43-0.3 *T*, depending on the value of liquid height (Figure 4.1). For T23, the Pitot was set at a fixed position *(r/T*=0.41 and *z/T*=0.61). After checking the influence of both the acquisition rate and the sampling time, a time-span ranging from 15 to 60 minutes and a sampling frequency of 500-800 Hz were adopted.

In the following, the origin of the cylindrical coordinate system is located at the center of the vessel bottom; the coordinates are normalized with the tank diameter *T* (*r/T*, *z/T*); the mean velocities and turbulence levels are normalized with the blade tip speed $V_{tip} = \pi ND$. The mean axial velocity, u_z, is positive if directed upwards and the mean radial velocity, u_r, is positive if directed towards the vessel wall.

4.3 Results and discussion

4.3.1 Liquid free surface oscillation modes

The way of operation of T49 was characterized first by visual observations. This preliminary step was essential for the appropriate selection of the PIV measurements conditions. After any change in the impeller speed, a transient state lasting several tens of minutes was detected before the achievement of steady state conditions, while tens of seconds are required in stirred tanks of standard geometry (Montante et al., 2001). In addition, at steady-state wide oscillations of the free surface took place.

At each value of H_L, the liquid free surface manifested two distinct wave modes, depending on *N*. Figure 4.2 shows the case of *T49* at H_L = 0.175 m. In Figure 4.2a, relevant to *N* = 150 rpm (*Re* = 2.4 x 10^4), the free surface presents the typical outline of unbaffled stirred tanks, with a definite

whirlpool vortex developing around the shaft, and driving the fluid tangentially towards the vessel wall.

At N = 300 rpm (Re = 4.8 x 10^4), a considerably different scenario is apparent (Figure 4.2b), since the free surface exhibits wide oscillations with a frequency well below that of the blades passage, and the superficial vortex rotates eccentrically around the shaft.

Two videos are also provided in the supplementary materials to give a better visualization of the phenomenon (ModelUnbaffledBioreactor_150rpm.avi; ModelUnbaffledBioreactor _300rpm.avi).

It is worth mentioning that, for H_L = 0.175 m at around N = 600 rpm (Re = 9.6 x 10^4), the dimensions of the whirlpool vortex and the intensity of the free surface motion lead to the complete flooding of the upper impeller, which exerts negligible pumping action on the fluid. Nevertheless, the free surface continues to oscillate with constant features as reported in Figure 4.2b, suggesting that once the oscillatory phenomenon has been triggered, it tends to endure irrespective of the action of the upper impeller.

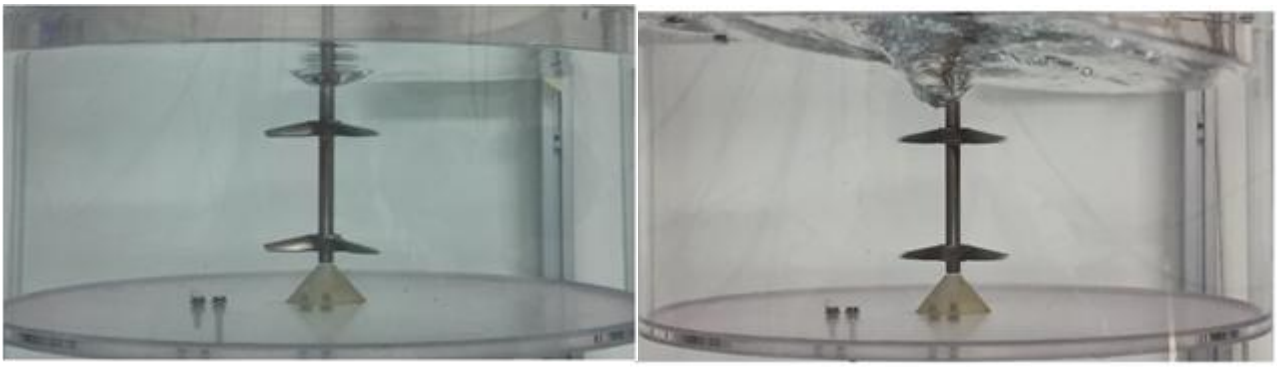

(a) (b)

Figure 4.2: Snapshots of the *T49* working at H_L = 0.175 m. (a) N = 150 rpm (Re = 2.4 x 10^4); (b) N = 300 rpm (Re = 4.8 x 10^4).

In order to widen the investigated conditions, the liquid free surface behavior of T23 for variable N and H_L was also considered. Two different stable modes of oscillations were found, depending on the values of impeller speed and liquid height. At low agitation speed and H_L = 0.17 m, the liquid surface manifests the typical outline often observed in unbaffled stirred tanks, with the whirlpool vortex developing around the shaft, and the free surface assuming a concave shape. As soon as the rotational speed increases over N=270 rpm, the features of the free surface change, and saddle-like waves start developing around the vessel axis.

Overall, we have observed for the first time three different oscillation modes of the free liquid surface in stirred tanks, while just central axial vortexes have been reported so far.

4.3.2 Flow characteristics of T49

The effects of the huge changes of the liquid free surface shape on the liquid mean flow field of T49 is evaluated by the analysis of the PIV measurements collected under steady-state conditions in the two zones A and B. The ensemble-averaged velocity vector plots are superimposed to the contour plots of the tangential component of the vorticity, ω_θ. The velocity vectors and the vorticity magnitude shown in Figure 4.3 and in the following figures are made dimensionless, dividing by the impeller tip speed, V_{tip}, and πN, respectively. The results collected in the lower impeller region at H_L = 0.235 m and varying impeller speed are shows in Figure 4.3. At N = 250 rpm (Re = 4 x 10^4), the impeller discharge stream is strongly axial, with mean velocities exhibiting an average inclination of 65° from the horizontal (Figure 4.3a). Under the thrust of the impeller, the discharge stream reaches the bottom of the tank and flows towards the lateral wall. For r/T < 0.1, a definite recirculation zone takes place below the impeller. As N increases (Figure 4.3b), the lower impeller jet starts to tilt radially, and at N = 400 rpm (Re = 6.4 x 10^4), it is completely lifted from the bottom (Figure 4.3c). Observing the specific flow features close to vessel basis, an elongated area of negative vorticity is apparent in Figure 4.3b and c, suggesting that under the selected stirring conditions the recirculation zone expands and more liquid heads for the center of the reactor, due to the orientation of the impeller discharge stream. The flow field measured at N = 250 rpm (Figure 4.3a) is closer to that typically obtained in a standard baffled tank stirred with A310 impellers (Bugay et al., 2002), since the impeller loop reaches the bottom of the vessel and runs towards the lateral wall. At higher impeller speeds, a flow transition occurs (Figure. 4.3b and c) and the main circulation loop features change completely. Flow patterns similar to that depicted in Figure 4.3c were detected increasing N, while reducing it backwards, the system tended to return to its initial configuration. This is the case shown in Figure 4.3d for N = 230 rpm (Re = 3.7 x 10^4). An analogous switch of the flow pattern between two stable configurations was visually observed in *T49* with H_L = 0.175 m and H_L = 0.205 m, at different values of the Reynolds number.

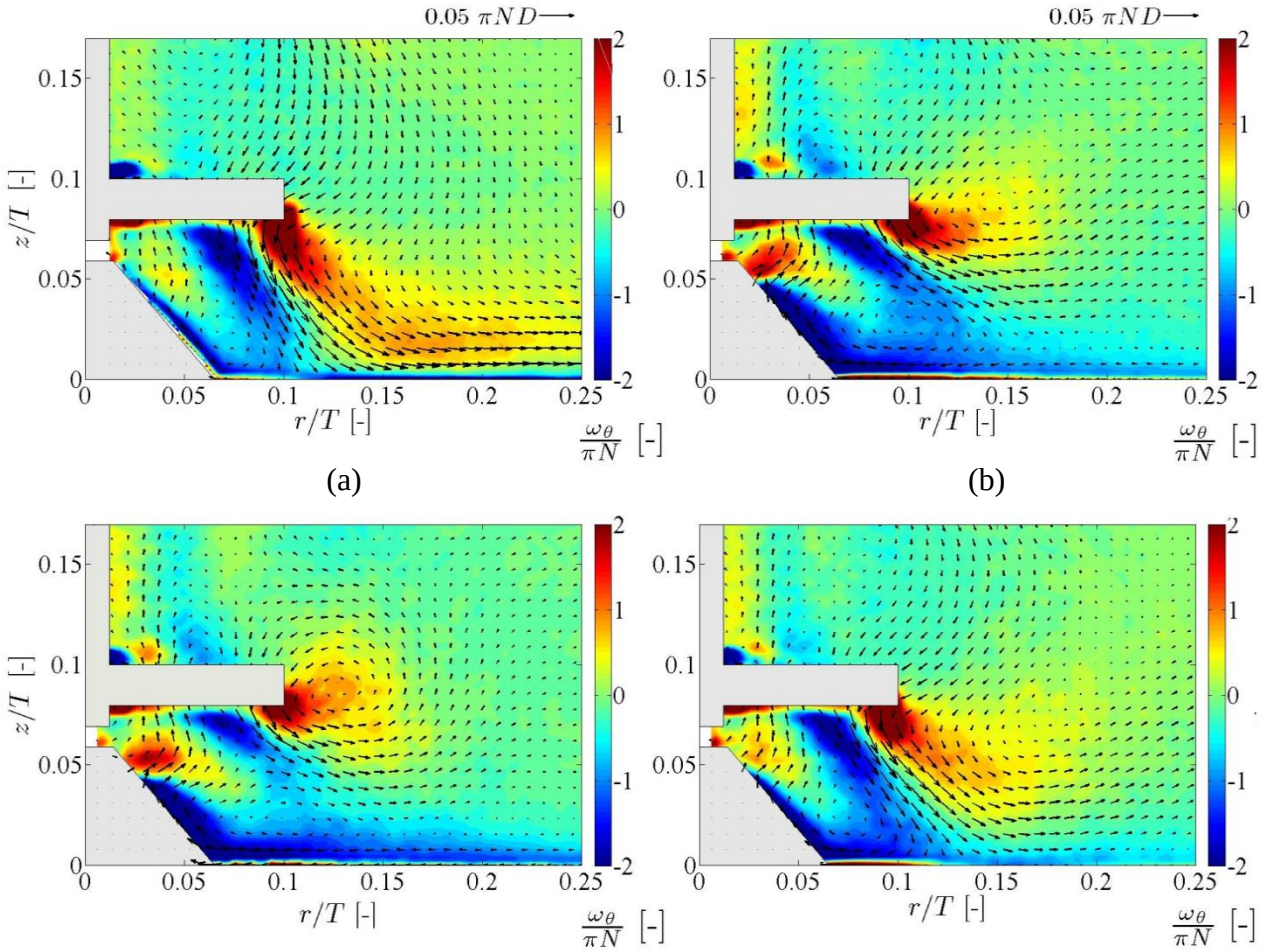

Figure 4.3: Ensemble-averaged flow field and contour plot of the tangential vorticity. *T49*, H_L = 0.235 m, '*zone A'*. (a) *N* = 250 rpm; (b) *N* = 330 rpm; (c) *N* = 400 rpm; (d) *N* = 230 rpm.

The flow transition of the lower impeller discharge stream from primarily axial to radial is further analyzed by the magnitude and the distribution of the turbulent kinetic energy, k'_{rz} which was estimated assuming isotropy for the unknown tangential component(Gabriele et al., 2011):

$$k'_{rz} = 2/3\left(u_r'^2 + u_z'^2\right) \tag{4.1}$$

Figure 4.4 shows the contour maps of $k'_{rz}/(\pi ND)^2$ at H_L = 0.235 m. For *N* = 250 rpm (Figure 4.4a), a zone with high turbulent kinetic energy content develops axially below the impeller. At *N*=400 rpm (Figure 4.4b) the impeller discharge stream is radially tilted and the distribution of k is completely different with respect to the previous case. Moreover, at the higher impeller speed, the highly turbulent fluctuations appear confined to the impeller region, while for radial locations *r/T* > 0.17

the turbulent fluctuations decrease very sharply.

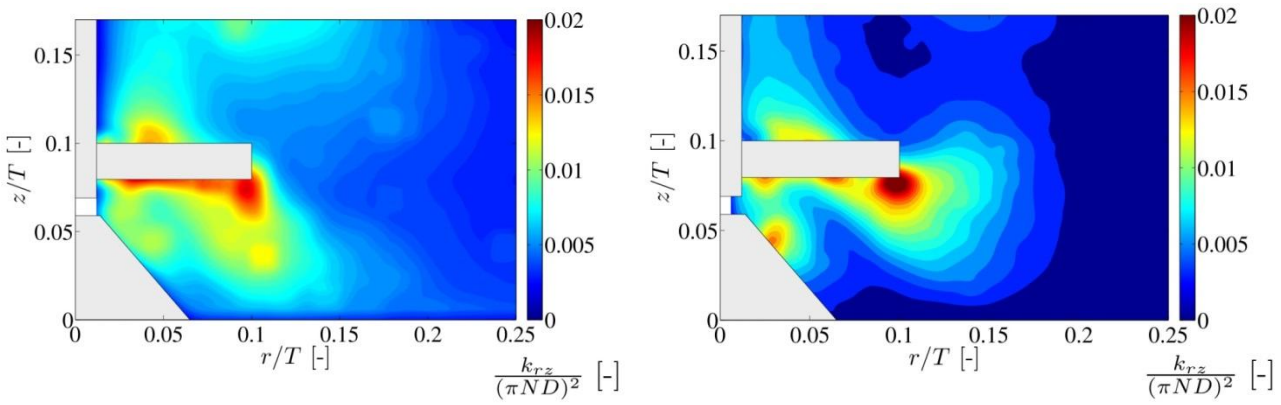

(a) (b)

Figure 4.4: Contour plot of $k'_{rz}/(\pi ND)^2$. *T49*, H_L = 0.235 m, '*zone A*'. (a) N = 250 rpm; (b) N = 400 rpm.

The effect of the impeller pumping action on the mean flow far away from the impeller can be appreciated in Figure 4.5, where the PIV data collected in zone B are shown for two impeller speeds corresponding to different impeller discharge stream inclinations.

The ensemble-averaged velocity vectors and the tangential vorticity contour plots disclose net differences between the two velocity patterns. At N = 200 rpm (Figure 4.5a), a circulation across the whole area investigated is apparent, where the fluid climbs up the lateral vessel wall and then is recalled towards the center of the tank. At N = 400 rpm (Figure 4.5b), the mean flow pattern is less definite, the dimensionless velocities have lower magnitude, suggesting that after the flow transition, the circulation of the fluid in regions located far away from the impeller is very limited.

It is worth observing that the wide free surface oscillations occurring at this agitation speed are expected to greatly affect the instantaneous vector fields measured in the vicinity of the gas-liquid interface, therefore, the ensemble averaged velocity field may not be adequate to properly depict the intrinsically transient behavior of the flow.

Also, the analysis of the velocity fluctuations in *zone B* reveals that at N = 400 rpm a significant increase in the fluctuating component of the velocities takes place, resulting in a tenfold increment of the dimensional kinetic energy, k'_{rz}, with respect to the N = 200 rpm condition.

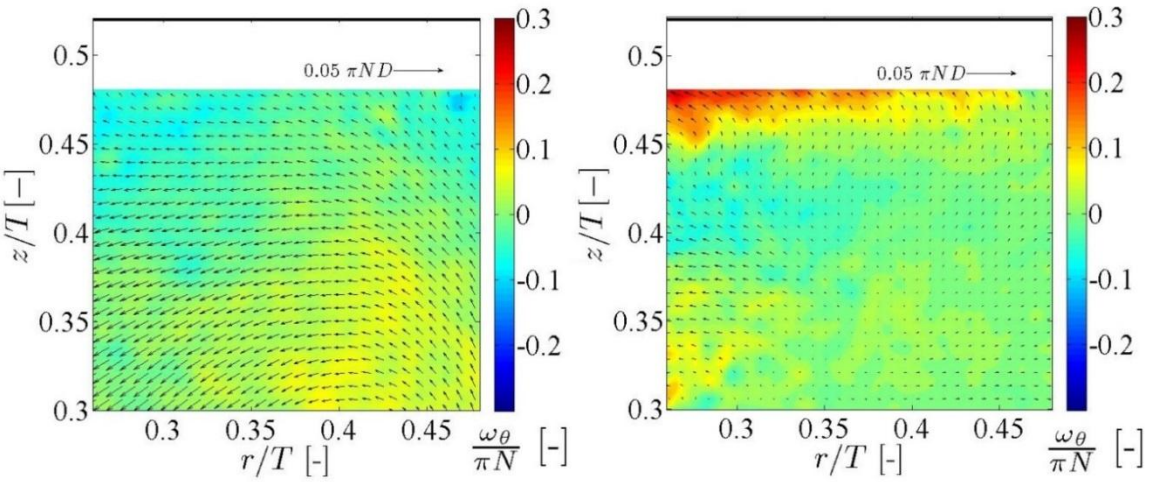

(a) (b)

Figure 4.5: Ensemble-averaged flow field and contour map of the tangential vorticity. *T49*, H_L = 0.235 m, '*zone B*'. (a) N = 200 rpm; (b) N = 400 rpm.

Matching the liquid free surface visual observations with the PIV results, the transition is clearly related to the liquid free surface, as a precise correspondence between the flow field variations and the wave mode exhibited by the liquid free surface exists at any value of H_L.

It can be concluded that the onset of the large-amplitude liquid sloshing in T49, occurring at specific values of impeller speed, triggered the flow transition, and thus it was the origin of the changes detected in the velocity flow patterns.

A deeper characterization of the stirred tank is presented in the following, due to the extensive influence of the free surface motion on the system fluid dynamics and to its potential huge impact on mixing performances.

4.3.3 Characteristics of the flow transitions: the discharge angle of the impeller stream

The inclination of the impeller discharge flow with respect to the horizontal axis, Θ, was calculated by collecting detailed PIV data close to the lower impeller varying the impeller speed. Starting from the condition of N = 200 rpm, the impeller rotational speed was increased stepwise up to N = 400 rpm. Afterwards, the impeller speed was reduced back to N=200rpm. For each condition, the value of Θ was estimated after the attainment of the steady state. Based on the visual observation, a time of approximately 45 minutes after any change of the agitation speed was considered appropriate to achieve the steady state condition.

The result for H_L = 0.235 m are shown in Figure 4.6. As can be observed, up to N = 300 rpm the angle Θ is almost constant and equal to 65° (‘*configuration 1’*). Above N=300 rpm, for a small increase of N a sudden drop of Θ to 25° is apparent (‘*configuration 2’*). This condition corresponds to the deflection of the lower impeller discharge stream towards the radial direction and to the onset of the peculiar free surface oscillations observed visually (Figure 4.2 b). Negligible variations of Θ were detected increasing the rotational speed above N=350 rpm, while reducing it backwards, for N < 250 rpm, the inclination of the impeller discharge stream rises again to about 65°, meaning that the velocity flow pattern and the free surface returned to their initial configurations.

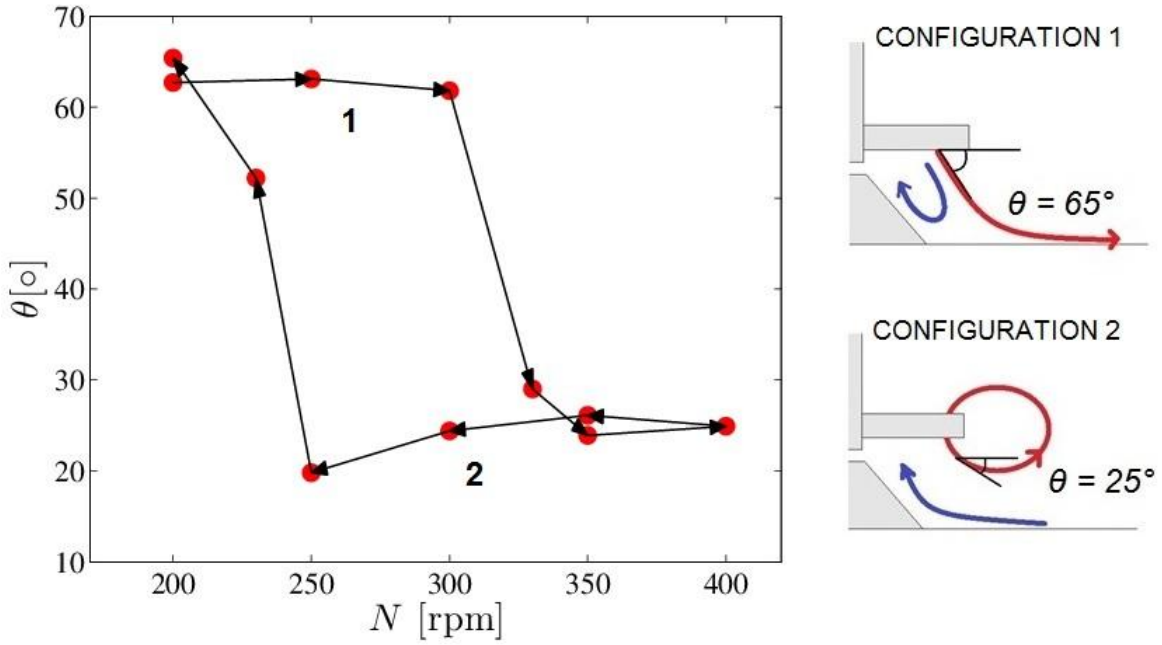

Figure 4.6: Inclination of the lower impeller discharge stream *vs N*. H_L = 0.235 m, *T49*.

It is worth observing that the flow transition exhibits an hysteresis, since the angle returns to 65° at around 230 rpm instead of at 330 rpm, thus having a delay of ΔN_{delay} = (330-230) rpm = 100 rpm. This result suggests that once the transition has been triggered, it tends to persist even when the agitation power goes below the value needed to prompt it.

4.3.4 Frequency analysis of the velocity time series

A quantitative evaluation of the characteristic frequencies of the flow was performed from the FFT analysis of the velocity time series collected with the Pitot system. The results relevant to the latter method only will be presented in the following, due to the higher reliability of the technique discussed above. The signal time trace shown in Figure 4.7 was collected after the attainment of the steady state condition at r/T = 0.44 and z/T= 0.43 (*T49*, location '*P*' in Figure 4.1), for a liquid height H_L = 0.235 m and N = 350 rpm. The time scale is limited to a maximum of 3 s for a clearer visualization.

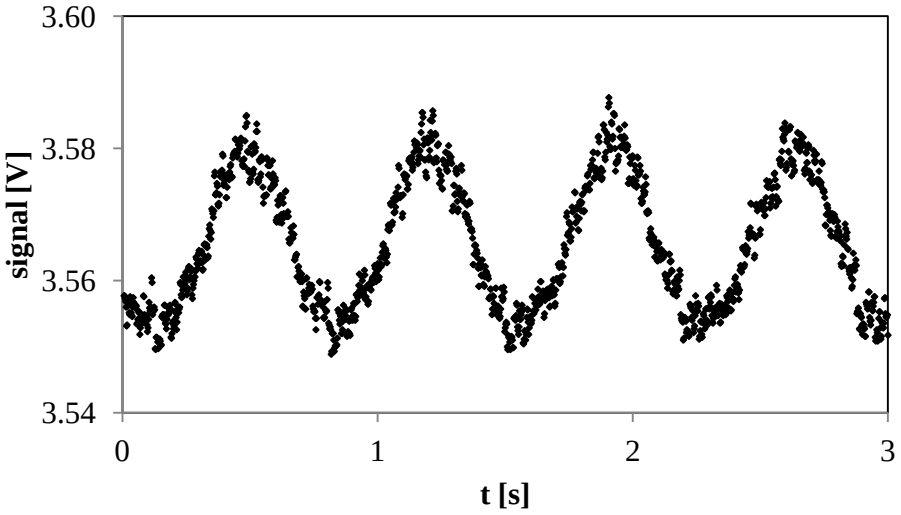

Figure 4.7: Time series of the voltage signal in the location '*P*' in *T49* (moving window averaged data on 0.01s). H_L = 0.235 m, N = 350 rpm (Re = 5.6 x 10^4).

The signal shows a definite cyclic variation, whose characteristic period is approximately equal to 0.7 s, corresponding to a frequency $f \approx 1.4$ Hz, which is lower than the blade passage frequency (f_{blade}=1.94Hz), but much closer to it with respect to the MIs detected so far. It is worth noticing that for N lower than 200 rpm, when the impeller discharge stream in axially oriented, the cyclic variation is not noticeable in our experimental data.

The frequency spectrum obtained at N = 300 rpm, thus before the appearance of the wide free surface oscillations and the modification of the impeller discharge stream from strongly axial to mainly radial, is shown in Figure 4.8a. The spectrum exhibit many peaks of small amplitude (order of magnitude 10^{-3}), but none of them is deemed prevailing. The shaft and the blades frequencies do not show a marked impact on the spectrum, and this can be explained considering that the measurement point was located far away from the impeller, at r/D = 2.2.

Different results were obtained when the rotational speed was set to a value that ensured the flow transition. This is the case depicted in Figure 4.8b, for N = 350 rpm.

As can be observed, the spectrum exhibits a clearly pronounced and narrow peak at f = 1.4 Hz, suggesting that well-defined periodic fluctuations manifest in the flow with this characteristic frequency.

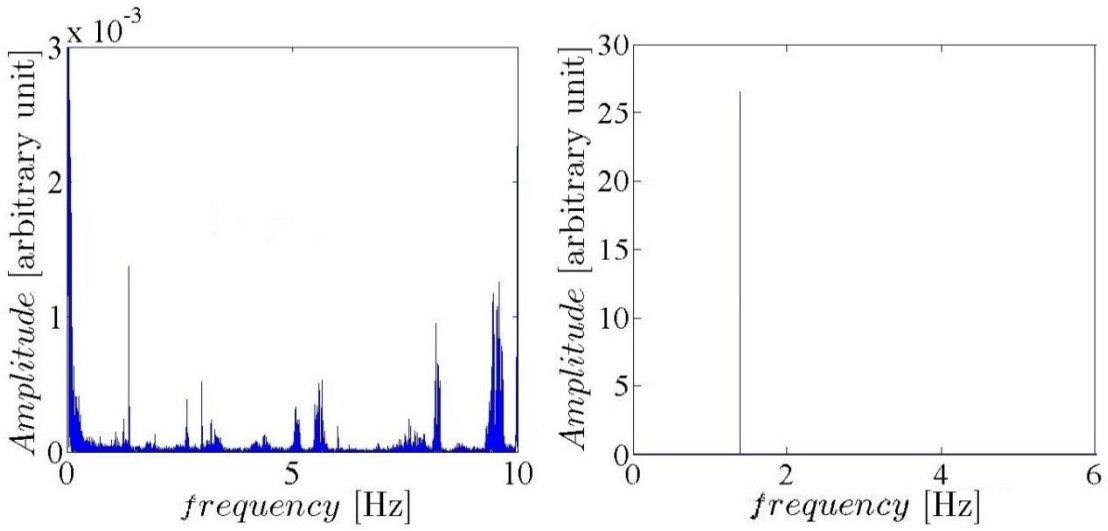

(a) (b)

Figure 4.8: Frequency spectrum of the voltage signal in the location '*P*'. *T49*, H_L = 0.235 m in T49. (a) N = 300 rpm (Re = 4.8 x 10^4); (b) N = 350 rpm (Re = 5.6 x 10^4).

To characterize further the periodic oscillations of the free surface, a Wavelet Transform (WT) analysis was applied to the dynamic signal, in order to provide the temporal distribution of the frequencies detected by FFT (Torrence and Compo, 1997). Hence, WT is suitable to identify if a periodic event has a transient or a stationary behavior in the time-span considered. In practice, the Morlet wavelet was selected as "mother wavelet", ψ, as in previous works it has been successfully employed to analyze oscillatory phenomena, similar to that under investigation (Galletti et al., 2003). The input signal is decomposed into a series of functions obtained from the scaling and the shifting of ψ. Figure 4.9 provides the time-frequency map of the voltage signal at N = 350 rpm in the location '*P*', together with the contour plot of wavelet power.

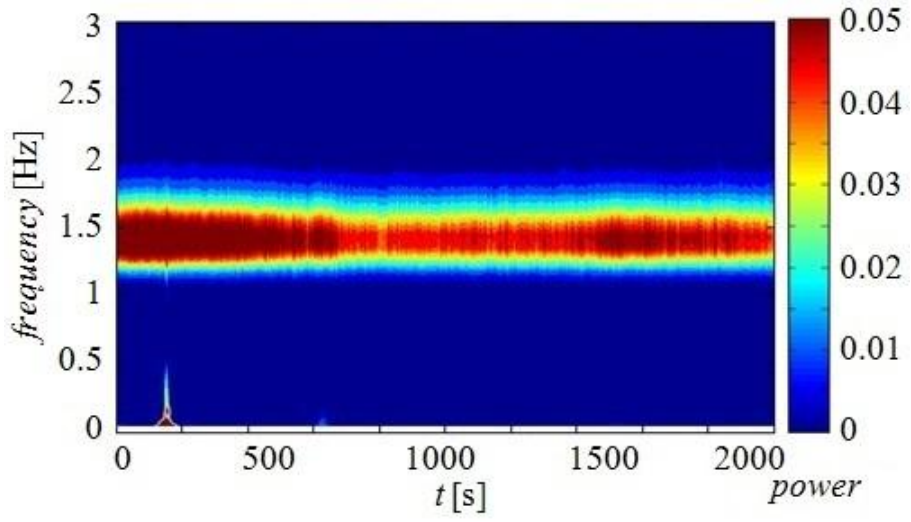

Figure 4.9: Time-frequency map and wavelet power (arbitrary units) of the voltage signal obtained in the location '*P*'. *T49*, H_L = 0.235 m, *N*= 350 rpm.

The wavelet power is high for values of *f* in the range 1.3-1.5 Hz over the whole time span, confirming that the oscillatory phenomenon detected is stationary. This dominant periodic event is clearly associated with the wide oscillations of the liquid free surface occurring approximately every 0.7 seconds at *N* = 350 rpm.

The frequency analysis was repeated varying the operating conditions, with the aim of determining the influence of the impeller speed on the characteristic frequencies. The system was studied with different liquid heights, in a range of rotational speeds ensuring the oscillatory motion of the interface. The results shown in Figure 4.10 reveal that the frequencies of the free surface instability obtained at different impeller speeds increases weakly for increasing values of H_L. For all the liquid heights considered, the frequency increases almost linearly with *N*. The solid lines in Figure 4.10, which follow very closely the experimental data trend, are almost parallel being represented by the equation: $f = k_1 + k_2 N$, with k_1 = 0.01 - 0.016 Hz and $k_2 \approx 1.3$, for *N* = 5.8 - 10 rps (*Re* = 5.6 10^4- 9.6 x 10^4). Overall, *f* is slightly affected by the impeller speed, but it mostly depends on a constant value, suggesting that the role of the geometrical characteristics of the system is more important than the agitation condition. This finding proves that the flow instability detected in *T49* differs from the Macro-Instabilities identified in the past. In fact, opposite to the results reported in Figure 4.10, a linear dependency of the MIs frequency on *N* with nil or very low value at *N*=0 has been typically reported within baffled stirred tanks (Nikiforaki et al., 2003) and unbaffled systems stirred with eccentrically-located impeller (Galletti et al., 2009).

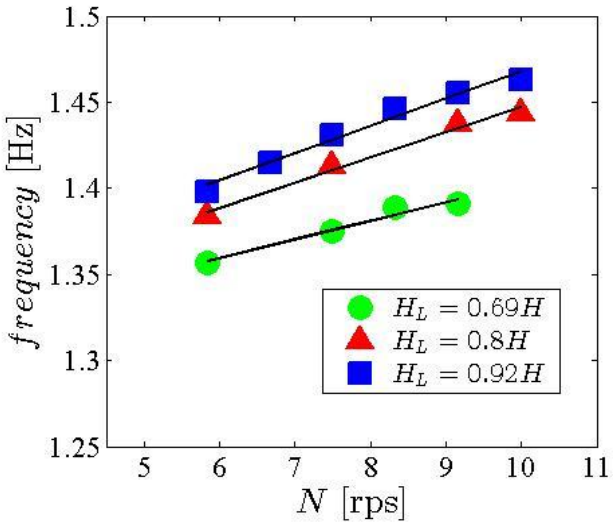

Figure 4.10: Influence of *N* on the instability frequency, *f*. *T49* with different liquid heights, H_L.

Additional results relevant to T23 are shown in Figure 4.11. The spectral distributions of the signal time series with H_L = 0.17 m for *N*=250rpm (Figure 4.11a) and *N*=300 rpm (Figure 4.11b) correspond to the symmetric vortex and saddle-like waves, respectively. Two relevant peaks occur in the spectrum for the lower impeller speed: the highest of 4.16 Hz corresponds to the shaft frequency, while the other, f_1 = 2.76 Hz is most likely associated to the free surface frequency. It is worth observing that, as a difference with T49, the shaft frequency can be clearly detected in the spectrum, and this is due to the fact that the measurement point was located closer to the impeller (*r/D* = 0.97), than in the case of T49 (*r/D* = 2.2). For *N* = 300 rpm, the spectrum exhibits a dominant peak at f_2 = 2.36 Hz, suggesting that a well-defined periodic phenomenon occurs. Also, the shaft frequency, 5 Hz, and the first resonant mode of f_2, 4.71 Hz, appear in the spectrum with a much lower magnitude.

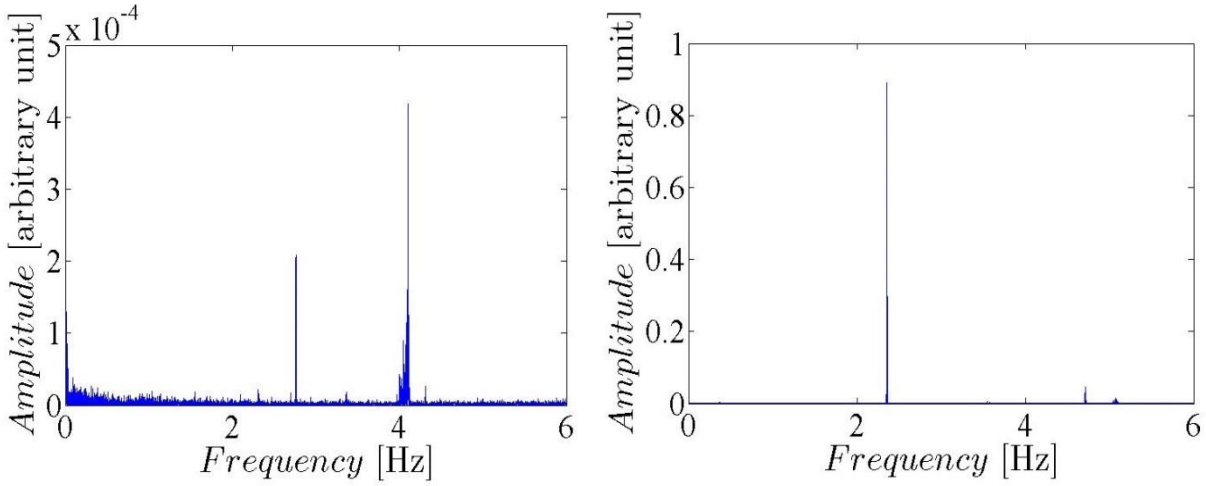

(a) (b)

Figure 4.11: Frequency spectrum of the pressure signal. H_L = 0.17 m. (a) N = 250 rpm; (b) N = 300 rpm.

A specific analysis is therefore required to identify the origin and the features of the instability associated with the oscillation of the liquid free surface.

4.3.5 Analysis and prediction of the surface wave frequencies

In the following, the characteristics of the surface instabilities are interpreted with a model previously developed for describing the free surface flows of partially filled vessels subject to external forces (Ibrahim, 2005). Depending on the characteristics of the disturbance and on the geometry of the tank, the model leads to the identification of different types of motion of the free surface, in the form of linear or nonlinear waves, with a periodic or chaotic nature. In addition, through the modal analysis of the free surface motion, the natural frequencies of oscillations and the corresponding wave modes can be determined.

For an upright partially filled cylindrical vessel, the standard theoretical approach reported by Ibrahim (2005) assumes that the liquid free surface intersects the vertical walls orthogonally and that the contact line is freely slipping. With this assumption, the angular natural frequencies of oscillation of the liquid free surface, f_{mn}, are given by the following equation (Equation 4.2):

$$f_{mn} = \frac{1}{2\pi}\sqrt{\left[\frac{g\xi_{mn}}{T/2} + \frac{\sigma\xi^3{}_{mn}}{\rho(T/2)^3}\right] tanh\left(\frac{\xi_{mn}H_L}{T/2}\right)} \qquad (4.2)$$

where g is the gravity constant, σ the liquid surface tension, ρ the liquid density, T the tank diameter and H_L the liquid height. The values ξ_{mn}, are the roots of the first derivative of the Bessel-function of the first kind and m^{th} order, and represent a series of modes in the tangential and radial directions. They are usually identified by the number of nodal diameters m and nodal circles n, respectively, and were calculated in detail by Bauer (1964). The natural frequencies depend only on the geometrical features of the apparatus and on its filling ratio. Each frequency corresponds to a wave pattern of the free surface. This means that, if any disturbance excites the system near one of its natural frequencies, the free surface will exhibit the correspondent oscillation mode as dominant, plus other low-amplitude secondary modes.

Following the approach adopted for the analysis of orbital shaken bioreactors by Reclari (2013), in Figure 4.12 different shapes of the free surface are schematically shown, depending on the number of nodal diameters m and nodal circles n. The analysis has been limited to the lowest few modes, i.e. m=0,1, 2 and n=1. It is worth observing that previous experimental investigations have revealed that these modes are most likely to be excited and that they produce the most effective dynamic forces (Pal et al., 2001).

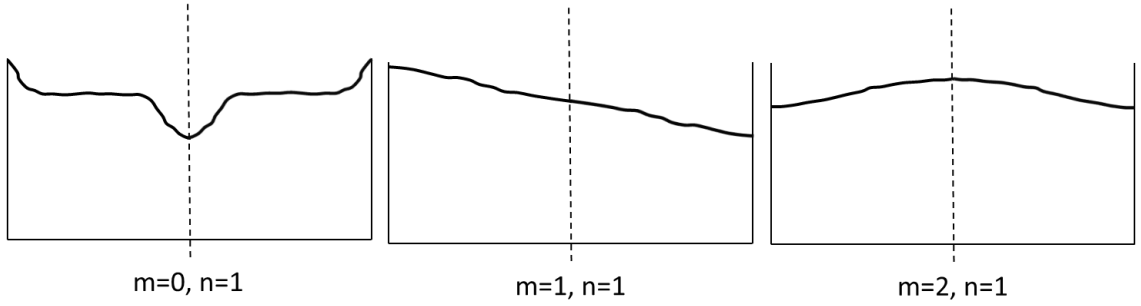

Figure 4.12: A schematic visualization of the free surface shape under main natural sloshing modes in a partially filled cylindrical vessel for m=0, 1, 2 and n=1.

The sloshing model results schematically reported in Figure 4.12 and the experimental observations shown in Figure 4.2 matches quite well. Indeed, vertical pulsation usually generates m = 0 modes and a symmetric motion of the free surface about the vessel axis, as is the case of the axially oriented impeller jet (Figure 4.2a). Lateral acceleration is expected to excite m = 1 as dominant modes and to produce asymmetric waves (Figure 4.2b), that is the case of the impeller jet when it assumes a radial orientation. The liquid free surface shape of *T23*, exhibiting a centrally located vortex for N <270rpm, is obtained with m=0 and n=1. As soon as the rotational speed increases over N=270 rpm, the saddle-like waves start developing around the vessel axis and this kind of surface oscillation can be predicted with m=2 and n=1.

Based on the visual evidence, there is a correspondence between the natural oscillation modes of the free surface in a confined vessel and the behaviour of partially filled stirred tanks. In the following, the liquid sloshing potential model is applied to the analysis of the fluid dynamic behavior of T49 and T23 to check if it can interpret the characteristic frequencies of partially filled cylindrical stirred tanks. Equation 4.2 was used to compute analytically the natural frequencies of both T23 and T49. The outcomes are reported in Figure 4.13, where the influence of H_L on the measured frequency is shown, together with three solid lines representing the outputs of the model for the two vessels and for the three natural frequencies corresponding to the observed behavior of the liquid free surface. It is worth noticing that while for the *T49* the measuring point was far from the impeller, for T23 the measuring point was close to the center of the stirred tank. As a result, in T49 only the frequencies corresponding to the (1,1) mode were detected, while in T23 also the (0,1) oscillation mode frequencies were clearly identified in the spectrum.

As can be observed, for T49 the theoretical curve follows the experimental frequencies for any *N*. Also, for the *T23* case, the measured values of f_1 and f_2 are in good agreement respectively with the zero and second modes of the natural oscillation frequencies, f_{01} and f_{21}. Hence, the liquid sloshing model seems appropriate to describe the flow developing in partially filled unbaffled stirred tanks, and suggests that the peculiar free surface instability arising within these apparatuses for selected ranges of operational conditions, mainly depend on the geometry of the system (T, H_L), although being triggered by the impeller motion. This experimental observation can explain also the reason why, after being established, the oscillatory phenomenon tends to maintain its features unaffected, even if the upper impeller is completely flooded, as happens in T49 at H_L = 0.175 m and N = 600 rpm. The prevailing effect of the tank geometry with respect to the impeller is further confirmed by previous results obtained for the A310 in standard tanks, where negligible effects of the MIs were found (Roussinova et al., 2000). The simplified approach proposed in this work can be particularly useful for the analysis of industrial apparatuses. Indeed, more advanced models based on Computational Fluid Dynamics, which were shown to successful predict the MIs (Roussinova et al., 2003; Hartmann et al., 2004) and the liquid free surface shape (Jahoda et al., 2011) in standard vessels, would be unaffordable for the stirred tanks considered in this work due to the very long transient time to achieve the steady state conditions.

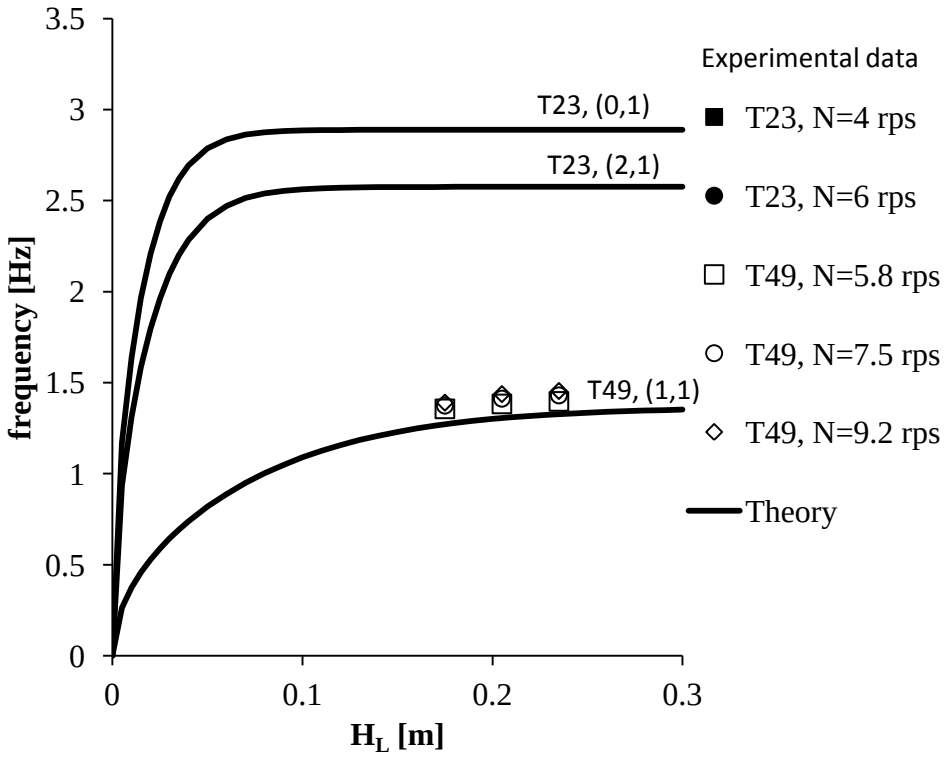

Figure 4.13: Influence of the liquid height, H_L, on the free surface frequency, f. The solid line represents the theoretical frequency evaluated using Eq. 2.

4.4 Conclusions

The occurrence of liquid free surface oscillations of different shapes and the consequent flow instabilities in partially filled stirred tanks of low height-to tank diameter ratio is reported for the first time. A deep insight on the origin and the features of this phenomenon is also provided. The simultaneous determination of the velocity flow field by PIV and of the liquid free surface behavior, by visual observation and Pitot measurements, proved that a sharp correspondence between the flow field instabilities and the wave mode exhibited by the liquid free surface exists.

Specifically, for selected combinations of N and H_L, a flow transition was found, manifesting with the modification of the impeller discharge stream inclination from typically axial to radial. As a result, relevant changes on the free surface oscillation pattern occur.

From a quantitative analysis of the phenomenon, the detected free surface instabilities differ from any of those identified in the past, as their frequency was found mostly dependent on the geometrical characteristics of the system and slightly on N, although being triggered by the impeller motion. A liquid sloshing model in a confined vessel was used to interpret the outcomes of the experimental analysis and very good agreement was found between the measured frequency data and the natural frequencies estimated analytically for partially-filled cylindrical containers.

These findings are of great relevance for the identification of the correct operative conditions for partially filled cylindrical stirred tanks. In fact, the occurrence of wide free surface oscillations within these apparatuses has to be carefully avoided, as it may lead to structural damages and/or to leakage of liquid, e.g. fermentation broth in the gas collection pipes.

4.5 References

J. J. Derksen, Numerical simulation of solids suspension in a stirred tank, AIChE J. 49 (2003) 2700-2714.

Brown D.A.R., Jones P.N., Middleton J.C., Papadopulos G., Arik E.B., 2004, Experimental Methods, in Handbook of Industrial Mixing, edited by E.L. Paul, V. A. Atiemo-Obeng, S.M. Kresta, Ch.4, p.157.

T. Hörmann, D. Suzzi, J. G. Khinast, Mixing and dissolution processes of pharmaceutical bulk materials in stirred tanks: experimental and numerical investigations, Ind. Eng. Chem. Res. 50 (2011) 12011-12025.

M. Assirelli, W. Bujalski, A. Eaglesham, A. W. Nienow, Macro- and micromixing studies in an unbaffled vessel agitated by a Rushton turbine, Chem. Eng. Sci. 63 (2008) 35–46.

L. E. Aloi, R. S. Cherry, Cellular response to agitation characterized by energy dissipation at the impeller tip, Chem. Eng. Sci. 51 (1996) 1523–1529.

D. J. Lamberto, F. J. Muzzio, P. D. Swanson, A. L. Tonkovich, Using time dependent RPM to enhance mixing in stirred vessels, Chem. Eng. Sci. 51(1996) 733–741.

J. M. Rousseaux, H. Muhr, E. Plasari, Mixing and micromixing times in the forced vortex region of unbaffled mixing devices, Can. J. Chem. Eng. 79 (2001) 697–707.

P. Armenante, C. Luo, C-C Chou, I. Fort, J. Medek, Velocity profiles in a closed, unbaffled vessel: comparison between experimental LDV data and numerical CFD predictions, Chem. Eng. Sci. 52 (1997) 3483-3492.

R. Alcamo, G. Micale, F. Grisafi, A. Brucato, M. Ciofalo, Large-eddy simulation of turbulent flow in an unbaffled stirred tank driven by a Rushton turbine, Chem. Eng. Sci. 60 (2005) 2303–2316.

S. Motamedvaziri, P. M. Armenante, Flow regimes and surface air entrainment in partially filled stirred vessels for different fill ratios, Chem. Eng. Sci. 81 (2012) 231–250.

G. Montante, A. Paglianti, Fluid dynamics characterization of a stirred model bio-methanation digester, Chem. Eng. Sci. 93 (2015) 38-47.

L. Nikiforaki, G. Montante, K. C. Lee, M. Yianneskis, On the origin, frequency and magnitude of macro-instabilities of the flows in stirred vessels, Chem. Eng. Sci. 58 (2003) 2937–2949.

Guillard, F., Trägårdh, C., Fuchs, L. Study on the instability of coherent mixing structures in a continuously stirred tank. Chem. Eng. Sci. 55 (2000), 5657-5670.

Ducci, A., Yianneskis, M. Vortex tracking and mixing enhancement in stirred processes, AIChE Journal, 53 (2007), 305-315.

S. M. Kresta, P. E. Wood, The mean flow field produced by a 45° pitched-blade turbine: Changes in

the circulation pattern due to off-bottom clearance, Can. J. Chem. Eng. 71 (1993) 42–53.

C. Galletti, E. Brunazzi, M. Yianneskis, A. Paglianti, Spectral and wavelet analysis of the flow pattern transition with impeller clearance variations in a stirred vessel, Chem. Eng. Sci. 58 (2003) 3859-3875.

C. Galletti, A. Paglianti, K. C. Lee, M. Yianneskis, Reynolds number and impeller diameter effects on instabilities in stirred vessels, AIChE J. 50 (2004) 2050–2063.

M. Yianneskis, Z. Popiolek, J. H. Whitelaw, An experimental study of the steady and unsteady flow characteristics of stirred reactors, J. Fluid Mech. 175 (1987) 537–555.

Paglianti, G. Montante, F. Magelli, Novel experiments and mechanistic model for macroinstabilities in stirred tanks, AIChE J. 52 (2006) 426–437.

Galletti, C., Pintus, S., Brunazzi, E. Effect of shaft eccentricity and impeller blade thickness on the vortices features in an unbaffled vessel, Chemical Engineering Research and Design, 87 (2009), 391-400.

R. A. Ibrahim, V. N. Pilipchuk, T. Ikeda, Recent advances in liquid sloshing dynamics, Appl. Mech. Rev. 54 (2001), pp 133–199.

R. A. Ibrahim, Liquid Sloshing Dynamics, first ed., Cambridge University Press, New York, 2005.

N. C. Pal, S. K. Bhattacharyya, P. K. Sinha, Experimental investigation of slosh dynamics of liquid-filled containers, Exp. Mech. 41 (2001) 63-69.

Y. Yang, Z. W. Liu, W. X. Shi, X. F. Huang, Accurate Measurement of Nonlinear Liquid Sloshing, AIAA J. 53 (2015) 771-779.

T. Okamoto, M. Kawahara, Two-dimensional Sloshing Analysis by Lagrangian Finite Element Method, Int. J. Num. Methods Eng. 11 (1990) 453-477.

Liu, P. Lin, A Numerical Study of Three-Dimensional Liquid Sloshing in Tanks, J. Comput. Phys. 227 (2008) 3921–3939.

S. Rebouillat, D. Liksonov, Fluid–Structure Interaction in Partially Filled Liquid Containers: A Comparative Review of Numerical Approaches, Comput. Fluids 39 (2010) 739–746.

M. Reclari, Hydrodynamics of orbital shaken bioreactors, PhD Thesis, Ecole Polytechnique Federale de Lausanne, Lausanne, Switzerland, 2013.

Reclari, M., Dreyer, M., Tissot, S., Obreschkow, D., Wurm, F.M., Farhat, M. Surface wave dynamics in orbital shaken cylindrical containers Physics of Fluids, 26 (2014), art. no. 052104.

G. Montante, K. C. Lee, A. Brucato, M. Yianneskis, Numerical simulations of the dependency of the flow pattern on impeller clearance in stirred vessels, Chem. Eng. Sci. 56 (2001) 3751–3770.

S. Bugay, R. Escudié, A. Liné, Experimental analysis of hydrodynamics in axially agitated tank. AIChE J. 48 (2002) 463–475.

Gabriele, A. N. Tsoligkas, I. N. Kings, M. J. H. Simmons, Use of PIV to measure turbulence modulation in a high throughput stirred vessel with the addition of high Stokes number particles for both up- and down-pumping configurations, Chem. Eng. Sci. 66 (2011) 5862–5874.

Torrence, P. Compo, A practical guide to Wavelet analysis. Bull. Am. Meteorol. Soc. 79 (1997) 61–78.

H. F. Bauer, Tables of Zeros of Cross Product Bessel Functions J p'(ξ) Y p'(kξ)-J p'(kξ) Y p'(ξ)= 0, Math. Comput. 18 (1964) 128-135.

Roussinova, V.T., Grgic, B., Kresta, S.M. Study of macro-instabilities in stirred tanks using a velocity decomposition technique, Chem. Eng. Res. Des., 78, (2000) 1040-1052.

Roussinova, V., Kresta, S.M., Weetman, R. Low frequency macroinstabilities in a stirred tank: Scale-up and prediction based on large eddy simulations, Chem. Eng. Sci., 58 (2003), 2297-2311.

Hartmann, H., Derksen, J.J., Van Den Akker, H.E.A. Macroinstability uncovered in a Rushton turbine stirred tank by means of LES (2004) AIChE Journal, 50 (2004), 2383-2393.

Jahoda, M., Moštěk, M., Fořt, I., Hasal, P. CFD simulation of free liquid surface motion in a pilot plant stirred tank, Can. J. Chem. Eng., 89 (2011), 717-724.

5 Microcarriers' suspension and flow dynamics in orbitally shaken bioreactors

5.1 Introduction

Stem cells represent attractive therapeutic agents for a wide range of diseases due to their capacity to differentiate into a specialized cell type. The large number of cells required for clinical trials (up to millions cells/kg of body weight) demands a fast and reproducible expansion protocol. Stem cells are adherent-dependent cells, as they are able to grow and differentiate only if attached to an appropriate support. Two-dimensional (2D) static culture methods rely on the use of disposable multi-layer vessels and have rapidly become the most common route for stem cells expansion (Simaria et al., 2014). However, these methods do not seem appropriate for stem cell large scale production because of the limited cell productivity, labor intense handling procedures and long cultivation times. For example, recent studies proved that commercial requirements would be satisfied only with the production of up to 10^{13} cells per batch, and the use of 10^5 layered vessels per lot, which is not a feasible process (Simaria et al., 2014). In addition, these systems are not able to supply reproducible batch culture conditions (Mohamet et al., 2010). A cost-effective approach which has demonstrated to overcome many of the limitations of 2D cultures is represented by three-dimensional (3D) dynamic culture methods based on microcarriers suspension technologies (Frauenschuh et al., 2007; Sart et al., 2009; Storm et al., 2010). Microcarriers are generally spherical beads with an ideal size of 100-300 μm, and can be made of different materials (plastics, glass, silica dextran, collagen). Cell attachment is promoted through electrical charges or collagen coating. In microcarriers culture cells grow as monolayers on the surface of the beads or as multilayers in the pores of macroporous structures, that are usually suspended in culture medium by gentle stirring (GE Healthcare Life Sciences, 2013). With this technique the physiological microenvironment of stem cells can be easily monitored and reproduced, with significant advantages towards large scale production (King and Miller, 2007; Liu et al., 2014). The use of microcarriers in cell cultures allows an increase in the surface area (SA) per unit volume (cm^2 /mL), improving product consistency and decreasing costs (Frauenschuh et al., 2007; Sart et al., 2009; Schop et al., 2008, 2009; Ferrari et al., 2012).

Most studies have focused on investigating the optimal medium components, the microcarrier type and concentration, however only a few considered the engineering aspects, the quality of the

microcarriers suspension and their impact on the liquid phase flow and turbulence levels.

Conditions that promote efficient attachment and uniform distribution of the cells over the microcarriers population must be sought and optimized, and from this point of view, the flow and mixing dynamics occurring in the bioreactor must be thoroughly investigated and carefully selected. Efficient flow dynamics is crucial to achieve complete suspension of the microcarriers, thus preventing particle agglomeration and enhancing the available adherence area for the cells, while mixing is essential to promote mass transfer within the environment and to avoid spatial gradients in culture parameters (e.g. dissolved gases, nutrient concentration, pH), that can directly affect cell growth (Lara et al., 2006). At laboratory scale, adherent-dependent cell cultures are often grown on microcarriers in orbitally shaken reactors (OSRs), which offer an effective solution in the early stages of bioprocess development. Once the process is optimized, it is then scaled-up to traditional stirred tank reactors (STRs), where the velocity characteristics and turbulence levels are different from those found in shaken cultures. To overcome the scaling up/down limitations due to the different types of bioreactor, current bioprocess strategies have seen the development of miniature stirred tanks (for example the Ambr15 cell culture, 10-15 mL), to be employed in bioprocess development, while large scale shaken systems up to a scale of 1000 L have recently become available in the market, and studies have demonstrated their mixing effectiveness and oxygen transfer capabilities (Zhang et al., 2009).

Recently a few studies have focused on the mixing and fluid dynamics of shaken bioreactors. The works of Weheliye et al. (2013) and Ducci and Weheliye (2014) have provided a detailed understanding of the single-phase flow generated in an orbitally shaken bioreactor at different operating conditions (e.g. shaker rotational speed, N, and medium height inside the tank, h), geometrical characteristics (e.g. cylinder inner diameter, d_i, and orbital shaking diameter, d_o) and fluid viscosity, v. A *Fr-Re* flow transition map was derived, where four types of mean flow were identified depending on the combination of Froude and Reynolds numbers selected. A transition from a toroidal to a precessional vortex configuration was detected with increasing Froude number, *Fr*, for fluids of water-like viscosity close to those employed in cell culture (high *Re* range). At low *Fr* the free surface exhibited an elliptic shape in phase with the shaker table orbital movement, while an increasing degree of out-of-phase and a highly three-dimensional free surface characterized the high end of shaker speeds investigated (Weheliye et al., 2013). A flow scaling law was derived to predict the occurrence of this flow transition based on the Froude number, *Fr*, the fluid non-dimensional height, h/d_i, and the orbital to cylinder diameter ratio, d_o/d_i. More specifically it was found that for $\square/\boldsymbol{d_i} \leq \sqrt{\boldsymbol{d_o/d_i}}$ the critical Froude number can be obtained from Equation 5.1, and it is associated to the toroidal vortex reaching the bottom of the cylindrical bioreactor

before transition occurs, while for $h/d_i > \sqrt{d_o/d_i}$ transition takes place without the toroidal vortex expanding all the way to the reactor bottom, and the critical speed/Froude number can be found from Equation 5.2.

$$Fr_{d_o} = \frac{1}{a_{ow}} \frac{h}{d_i} \left(\frac{d_o}{d_i}\right)^{0.5} \tag{5.1}$$

$$Fr_{d_i} = \frac{1}{a_{ow}} \tag{5.2}$$

Where a_{ow} is a constant depending on the fluid employed (1.4 for water), and the Froude number is defined as the ratio of the centrifugal to the gravitational accelerations, $Fr_d = 2\pi^2 N^2 d/g$, with d being either the orbital ($d = d_o$, Equation 5.1) or cylinder ($d = d_i$, Equation 5.2) diameters.

The flow scaling law of Weheliye et al. (2013) was successfully applied to the mixing time experiments of Rodriguez et al. (2013, 2014) obtained by means of a base-acid colorisation technique in shaken bioreactors of cylindrical geometry. Rodriguez et al. (2014) compared their data to those obtained by Tissot et al. (2010) for very different operating conditions (d_o , V_f) and bioreactor sizes (d_i), and found out that the two sets of data scaled well when the mixing number was plotted against the ratio of Fr/Fr_{cr} , and achieved a constant value after flow transition occurred ($Fr > Fr_{cr}$).

Recently Mancilla et al. (2015) compared the mean flow and turbulence levels in orbitally shaken flasks with conventional, coiled, 1 and 3 baffle geometries. The 2D-PIV results obtained on a horizontal plane of measurements for increasing rotational speed, N, indicate that the configuration with a single baffle is characterised by turbulence levels 25% higher than in the other configurations investigated, and should be employed for production of bacterial cultures. Numerical simulation studies of the flow dynamics in shaken systems have been carried out by Zhang et al. (2005) and Zhang et al. (2008) for 250-mL Erlenmeyer flasks and for 24-well and 96-well bioreactors with water-like viscous fluids, respectively, while Kim and Kizito (2009) simulated the flow in a cylindrical shaken bioreactor for different fluid viscosity. Discacciati et al. (2012) developed a pressure correction method to best capture the free surface deformation and assess the shear stress levels in an orbitally shaken cylindrical container for a high viscous fluid, while Reclari et al. (2014) compared the free surface wave measurements in a shaken cylinder against those predicted by a potential sloshing model, and identified the presence of different modal responses inducing different flow regimes.

Little information can be found in the literature regarding the flow and mixing dynamics taking place in bioreactors when microcarriers suspensions are considered. Collignon et al. (2010) investigated the suspension of microcarriers for TTP Mixel, A325-A320 Lightnin, three streamed-blades VMI-Rayneri, and Elephant Ear Applikon impellers in a stirred tank reactor, and compared the flow characteristics, shear rate and power consumptions of the different impellers at the corresponding just suspended speed, N_{js} . Their results indicated that the TTP Mixel and the Ear Elephant Applikon impellers produced the lowest mechanical constraints at their just suspended speed. PIV measurements in a spinner flask were carried out by Ismadi et al. (2014) to assess to what extent flow shear stresses can affect cell culture of mouse induced pluripotent stem cells (iPSC) attached to microcarriers. They show that optimum number of cells was achieved over 7 days in 25 RPM suspension culture, corresponding to a maximum shear of 0.0984 Pa. Nienow et al. (2014) developed a new method for the harvesting of human mesenchymal stem cell (hMSC) in a spinner flask. The cells were cultured in dimple-bottomed spinner flasks equipped with a magnetic horizontal stir bar and a vertical paddle at a working volume of 100 mL and at 30 RPM (N_{js}). After expansion, harvesting was implemented by adding trypsin-EDTA and agitating the microcarriers suspension for 7 min at 150 RPM. Their study indicates that intense agitation for a short period (7 min) under the presence of a suitable enzyme can promote cell detachment without damaging the cells or affecting their attributes. The overall harvesting efficiency was above 95 %.

Recently Olmos et al. (2015) determined the critical agitation speed for microcarriers' suspension in orbitally shaken Erlenmeyer flasks and cylindrical reactors. They stained the microcarriers with Trypan blue and used a camera rigidly moving with the shaker table to assess their suspension at increasing speed. The Vachy-Buckingham theorem was employed to obtain the non-dimensional model of Equation 5.3.

$$\frac{N_s}{\sqrt{g/d_o}} = \sqrt{\frac{Fr_s}{2\pi^2}} = A \left(\frac{h}{d_i}\right)^{0.5} \left(\frac{d_o}{d_i}\right)^{0.25} (\rho^*) \left(\frac{d_p}{d_i}\right)^{-0.07} \tag{5.3}$$

Where A is a constant depending on the type of geometry used (1.39 for cylinder, 0.12 for Erlenmeyer flask), and ρ^* and d_p are the relative density and diameter of the microcarriers, respectively. It should be noted that in Equation 5.3 they considered a Froude number which is defined as a velocity ratio, and it is related to the one defined in this work by the square root of Fr. Direct comparison of Equations 5.1 and 5.3 shows that the critical Froude number, Fr_{cr} , associated to the flow transition reported by Weheliye et al. (2013), is related to the suspension Froude number, Fr_s , obtained from the model of Olmos et al. (2015), with the non-dimensional fluid height, h/d_i

and orbital to cylinder diameter ratio, d_o / d_i , terms having the same exponents. It is interesting to point out that their model showed a very good agreement also for Erlenmeyer flasks, implying that a similar flow transition to the one reported by Weheliye et al. (2013) could take place also in this geometry.

In the present study a different approach has been developed, where the "just-suspended" speed is estimated from the light scattered by the microcarriers on a laser plane parallel to the bottom of the cylindrical bioreactor, while vertical plane measurements were obtained to assess the homogeneity of microcarriers across the tank volume. Furthermore, two-phase Particle Image Velocimetry experiments were carried out to better comprehend the flow and mixing dynamics in the presence of microcarriers, and to assess how their concentration affects the mean flow characteristics.

5.2 Materials and methods

Depending on the measurements being carried out, two different experimental rigs were employed. Figure 5.1 a shows the experimental set-up used to obtain the "just suspended speed", where a 300 mW continuous diode laser, a mirror, a Net iCube camera with Macro Lens, and a cylindrical bioreactor with a flat bottom, were all rigidly mounted on a Lab LS-X Kühner shaker table. The laser-light was directed horizontally in order to illuminate the plane located immediately over the vessel bottom, while a camera gained optical access to the measurement plane through a mirror located underneath the bioreactor. The camera was equipped with a macro lens with a shallow depth-of-field, that allowed to capture any small variation of the image brightness, which was directly related to the light scattered by the microcarriers sitting at the bottom of the bioreactor, as the shaking speed was varied. For each orbital speed investigated, 50 images were captured, and analysed by home-built Matlab routines to obtain a quantitative average result of the suspension conditions of the system. Before capturing a set of images a sufficient time was given to ensure steady-state condition was achieved at each speed investigated. Experiments were carried out in a borosilicate glass cylindrical bioreactor of size d_i = 7 cm, for different ranges of orbital diameters, d_o = 1.5 − 5 cm, and shaker speeds, N = 60 − 140 RPM. The working liquid was distilled water with a fluid height h = 3 and 5 cm (V_f = 115.5, 192.5 mL). Commercial microcarriers, GE Cytodex 1 (ρ = 1.03 kg/L, d_{50} = 190 μm) and GE Cytodex 3 (ρ = 1.04 kg/L, d_{50} = 175 μm), were employed at concentrations typically adopted for stem cell cultures: 2.5, 7.5, 12.5 g/L (0.25, 0.75, 1.25 wt%). Their settling velocity was approximately 0.6 mm/s. More information on the characteristics of the microcarriers employed can be obtained in GE Healthcare Life Sciences (2013).

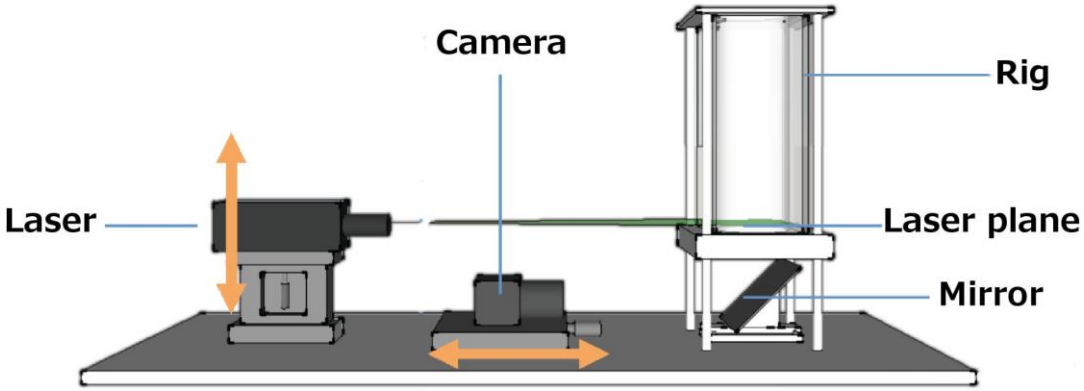

(a)

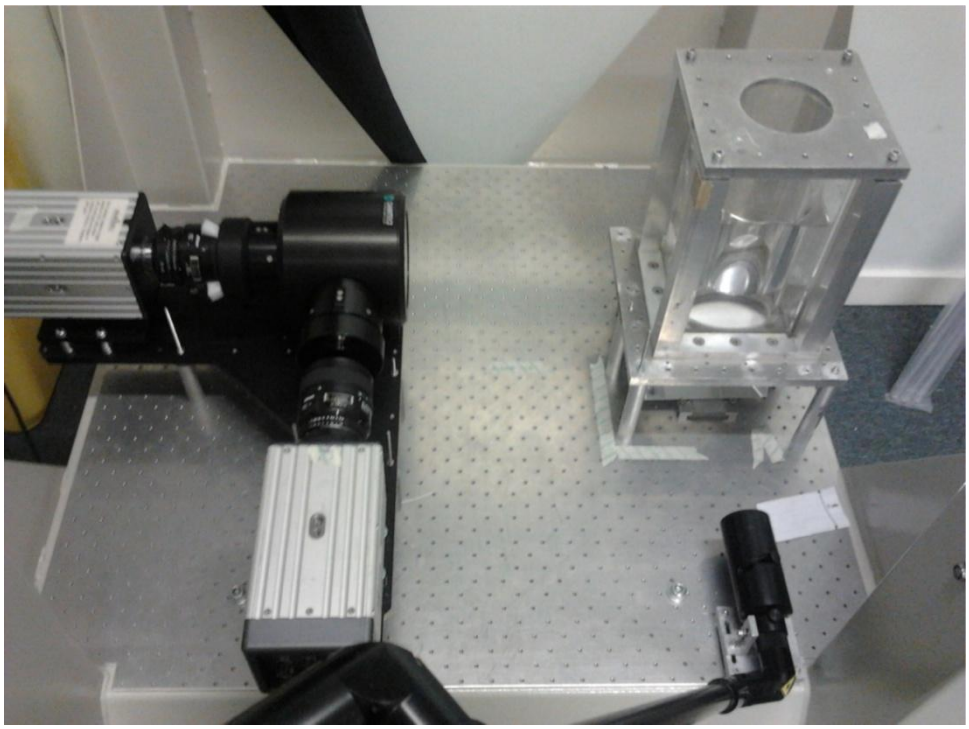

(b)

Figure 5.1 Experimental set-ups: (a) suspended speed; (b) two-phase PIV.

The two-phase PIV system is shown in Figure 5.1 b, where a larger Kühner shaker table (1 × 1 m^2, SR200-X shaker) is used to hold two cameras sharing the same field of view by a 50 %-transmission/50 %-reflection mirror and an optical guiding arm shining the laser onto a mirror positioned underneath the reactor. Contrary to the suspension speed experiments, in this case the measurement region consisted on the vertical plane bisecting the bioreactor into two halves. Each camera was equipped with a different light filter (either green, λ = 532 nm, or orange λ = 570 nm) to distinguish between the solid and liquid phases. To improve the image quality of the solid phase, fluorescent Rhodamine B isothiocyanate was employed to stain GE Cytodex 3 microcarriers, by exploiting the strong bond occurring between the dye and the thin collagen layer that coats the

microcarriers' surface. The staining protocol consisted in mixing 2 mg of Rhodamine in 50 mL of deionized water for a 200 mg sample of GE Cytodex 3. Staining was done at room temperature for 12 hrs and a 45 μm sieve was used to filter the stained particles. After this procedure the two-phase measurements could be carried out up to a solid concentration of 0.75 g/L (0.075 wt%). Above this threshold the image quality decreased due to the laser attenuation across the measurement plane induced by the presence of the microcarriers. Distilled water seeded with 1-40 μm flakes of painting was used as the continuous phase. Experiments were performed in a glass cylindrical bioreactor of size d_i = 10 cm, with an orbital diameter, d_o = 5 cm, and a fluid height h = 5 cm (V_f = 392 mL) for different shaker speeds, N = 80−130 RPM.

Phase-locked measurements were obtained by a magnetic encoder coupled to the Kühner shaker table. The origin of the angular coordinate, φ, was set when the system reaches its position furthest to the left as the clockwise orbit is viewed from above. To fully resolve the large scale flow structures the measurement spatial resolutions of the liquid and solid phases were Δx_i =1.66 mm and 1.84 mm, respectively, while the time interval between PIV image pairs was Δt =1-2 ms. The time interval, Δt, was selected according to the optimisation protocol developed by Gomez et al. (2010). In the rest of the article a cylindrical coordinate system r, φ, z is employed with the origin positioned on the cylinder axis at the bioreactor base. As mentioned in the introduction the Froude number based on the orbital diameter is an essential parameter to control the flow dynamics inside the bioreactor, and will be referred to here after either as Fr_{do} or, to simplify, as Fr. A comprehensive list of the operating conditions investigated for the suspension speed and PIV experiments is provided in Table 5.1.

SUSPENDED SPEED	***SOLID-LIQUID PIV***
d_i = 7 cm	*d_i = 10 cm*
d_o = 1.5, 2, 2.5, 3, 4, 5 cm	*d_o = 5 cm*
N = 0 - 200 RPM	*N = 80, 90, 96, 110, 130 RPM*
h = 2, 3, 4, 5 cm (V_f = 76.9 - 192.5 mL)	*h = 5 cm (V_f = 392.5 mL)*
c = 2.5, 7.5, 12.5 g/L (0.25, 0.75, 1.25 wt %)	*c = 0.25, 0.5, 0.75 g/L (0.025, 0.05, 0.075 wt %)*

Table 5.1: Geometrical details of the shaken systems and operational conditions investigated for the two-phase measurements.

5.3 Results and discussion

In the following sub-sections the three parts of the investigation, that is, microcarriers' suspension speed, microcarriers' dispersion, and two-phase flow dynamics, are discussed in sequence. In brief, the rationale for the selection of these three parts of the work was to identify the range of speeds over which suspension occurs for different operating conditions, to assess the microcarriers' suspension and dispersion mechanisms as the shaker speed is increased, and to determine the flow dynamics and transition of the two-phase system as well as compare them against those obtained for a single-phase (Weheliye et al., 2013).

5.3.1 Microcarriers suspension speed

The just suspended speed was estimated from the brightness of the images taken on the horizontal measurement plane, which is directly proportional to the amount of particles sitting at the bottom of the reactor. The image brightness, I_B (N), at a given shaking speed, N, is defined in Equation 5.4 by adding the pixel greyscale, p_{ij} , across the area delimited by the bioreactor walls on the horizontal plane of measurement:

$$I_B = \sum_{N_{tot}} p_{ij} \tag{5.4}$$

where N_{tot} is the total number of pixels across the area.

The microcarriers' suspension process and its correlation to the brightness percentage index, $I_B(N)/I_B(0)$, for increasing shaking speed, N, can be gained from Figure 5.2, where steady-state images of the microcarriers' concentration over horizontal planes are coupled to the $I_B(N)/I_B(0)$curve at key speeds. This set of experiments was carried out for an orbital diameter d_o = 2.5 cm and a microcarriers' concentration c = 2.5 g/L. At low shaking speeds the microcarriers are uniformly distributed over the vessel bottom, and the brightness index is approximately constant up to a speed of 110 RPM, when the particles start being arranged in a spiral pattern on the bioreactor base and a drop of $I_B(N)/I_B\ (0)$occurs. As the orbital speed is further increased a nearly constant value of the brightness index is attained above 150 RPM, implying that the "just-suspended" condition is achieved.

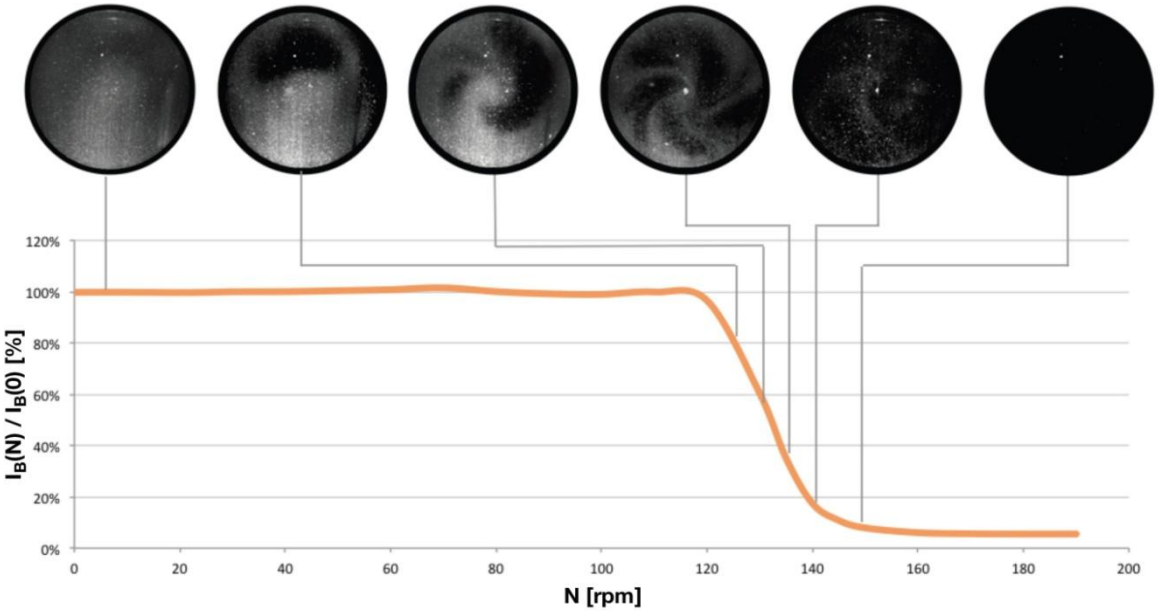

Figure 5.2: Visualization of the suspension mechanism and variation of the brightness percentage index, $I_B(N)/I_B(0)$, with shaking speed (d_o = 1.5 cm, h = 5 cm, c = 2.5 g/L).

To better compare the results obtained for the different conditions analysed, the normalised brightness index, I^*, of Equation 5.5, which is scaled with the zero-speed, $I_B(0)$, and final-speed, $I_B(\infty)$, brightnesses, is used in the rest of the work.

$$I^* = \frac{I_B(N) - I_B(\infty)}{I_B(0) - I_B(\infty)} \tag{5.5}$$

The suspended speed is associated to a 95 % decrease of the brightness index with respect to the zero-speed condition, and it is identified as the speed at which I^* = 5%. Based on the statistical error of the brightness index, ≈ 3 %, and the non-linear regression method used to fit the data points, the uncertainty affecting the just suspended speed was found to be ≈ 5 %.

A video showing the particle suspension dynamics is also provided in the supplementary materials (JS-Video.avi). In this case however the shaker table was started from still conditions and, similarly to standard operating procedures, was gradually accelerated to a final speed of 140 RPM by the controller mounted on the shaker system (i.e. steady-state conditions were not achieved at intermediate speeds). As a consequence the instantaneous velocity associated to each frame is unknown, and the following discussion is made in terms of number of revolutions of the shaker tray (i.e. the encoder was used to acquire a frame per revolution). In agreement with the data reported in Figure 5.2, darker zones start appearing at the periphery of the bioreactor (t = 3 − 5 s of the video),

with microcarriers being more concentrated at the centre for increasing speed.

This is well captured in Figure 5.3 a, where the radial profiles of the normalised brightness index, $I^*(r)$, are shown for selected time instants, counted in number of revolutions, n, of the shaker tray, and corresponding to increasing shaking speed. After 100 revolutions, the shaker table has not gained a speed high enough to lift the particles, and the index I^* is nearly constant across the bioreactor diameter and close to unity. As the shaker table is accelerated a drop of I^* occurs after 110 revolutions, with the micriocarriers being suspended for $r/R \geq 0.6$, while the center of the bioreactor, $r/R \leq 0.3$, is still unaffected after 130 revolutions. It is worth noticing that also the rate of suspension is lower in proximity of the bioreactor axis. For example, a 10 revolutions increment ($n = 120 - 130$) for $r/R \geq 0.6$ determines a variation of the normalised brightness index of $\Delta I^* \approx 0.45$, while a similar drop (≈ 0.5) occurs at $r/R = 0.3$ over a larger range of shaker revolutions, $\Delta n = 30$ ($n = 140 - 170$).

The spiral pattern, described in Figure 5.2 and shown in the supplementary video, is further analysed in Figure 5.3 b, where the azimuthal profiles of I^* are plotted at $r/R = 0.8$ for an increasing number of shaker table revolutions ($n = 100-135$). It is evident that for $n = 110-122$ the profiles show a cyclic variation in the azimuthal direction, with 5 peaks over the range of θ considered. As expected the intensity of the profiles is decreasing as more microcarriers are lifted with increasing speed (i.e. number of revolutions), and the profiles are randomly shifted with respect to each other along θ, because the instants considered were taken far apart in time, and the spiral structure might have rotated with respect to the bioreactor. However an estimate of the spiral inclination can be gained from Figure 5.4 a, where a single cycle of I^* has been obtained through a phase-average, h_i, along the azimuthal direction with a period $\Delta\theta = 20^\circ$. This analysis was performed at different radii for a single frame, $n = 117$. The phase-averaged profiles were normalised by their maximum variation $<\Delta I_B>$, so that the final brightness parameter assumed a maximum absolute intensity of ≈ 1 for all the radii considered ($r/R = 0.6-0.9$).

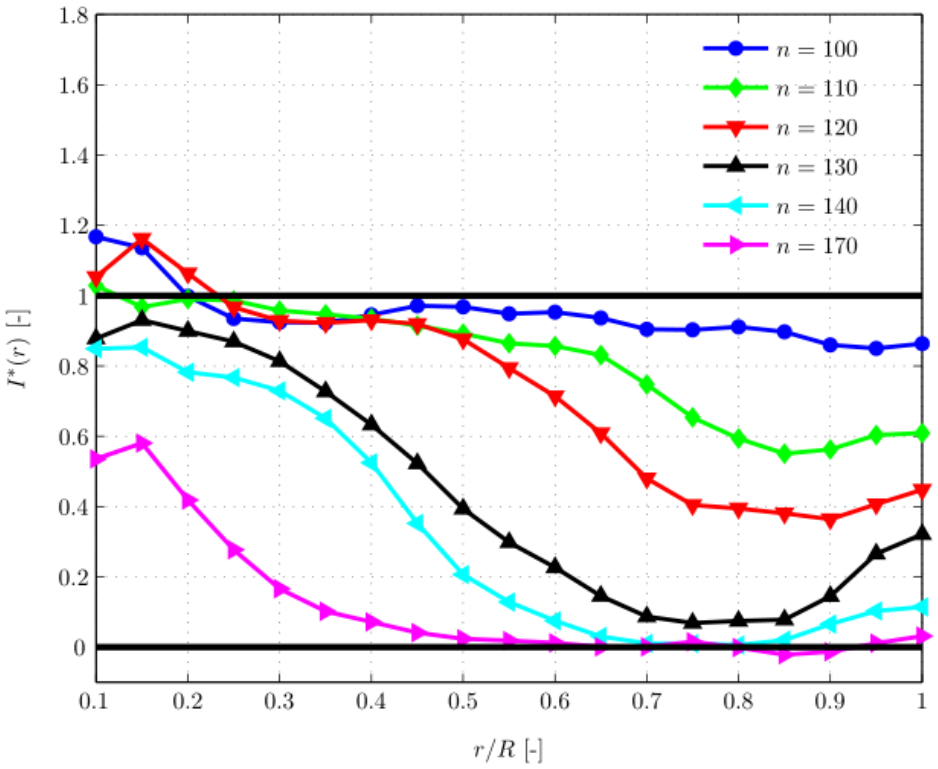

(a)

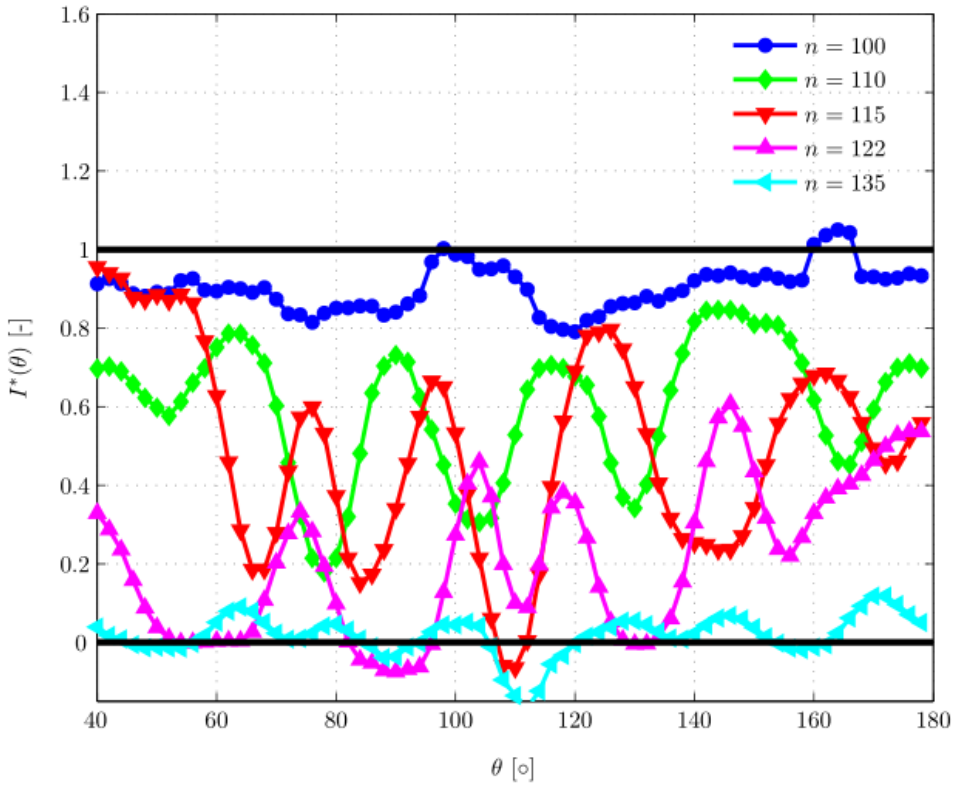

(b)

Figure 5.3: Profiles of the normalised brightness index I^* for increasing number of shaker revolutions (d_o = 2 cm, h = 3 cm, c = 2.5 g/L): (a) radial profiles; (b) azimuthal profiles (r/R = 0.8).

It should be noted that in Figure 5.4 a the flow direction is from right to left and opposite to that of θ. The peak shifts to the right as the radius increases, which means that the spiral is oriented towards the center in the direction of motion. The variation of the peak azimuthal coordinate, θ_{max} , against the radius is shown in Figure 5.4 b for two time instants, n = 117 and 120. The peak azimuthal coordinate, θ_{max} , shows a linear increase with r/R and the slope magnitude is nearly the same for both instants considered (i.e. 18.57° vs 18.86°). A visualisation of the spiral locus is provided in the inset diagram, where the arrow points in the flow direction.

The variation of I^* against the shaker tray speed is plotted in Figures 5.5 a and b for two orbital diameters, d_o = 1.5 and 2.5, respectively. Three different microcarriers' concentrations are considered, c = 2.5, 7.5 and 12.5 g/L, while the fluid height and vessel size are kept constant (h = 5 cm, d_i = 7 cm). It should be noted that by definition the index, I^* , can assume only values between 0 and 1 at high and low shaking speeds, respectively. Data points are fitted with the model of Equation 5.6, where in the remainder part of the work the variable x can either be the shaker speed, N, or the Froude number ratio, Fr/Fr_{cr} .

$$I^*(x) = \frac{1}{1 + e^{a(x-x_0)}} \tag{5.6}$$

The parameters x_0 and a position the curve along the x coordinate, and control its rate of decay, respectively. The plots of Figure 5.5 a cross the 5 % reference line within a relative small range of suspension speeds, N_s = 153 − 160 RPM, and a correlation between the concentration and the suspension speed seems to be present (i.e. lower suspension speeds occur for lower concentrations). However this correlation is not present in the data of Figure 5.5 b for d_o = 2.5 cm, where an opposite behaviour is observed (i.e. lowest suspension speed for greatest concentration considered). Also in this case the range of variation of the suspended speed is relatively small, N = 145 −152 RPM, and it is within the error of the measurement technique employed. Based on this consideration it was concluded that the concentration should not affect to a large extent the suspension of the microcarriers, at least within the range of concentration considered in this study, which includes those commonly employed in the bioprocess industry.

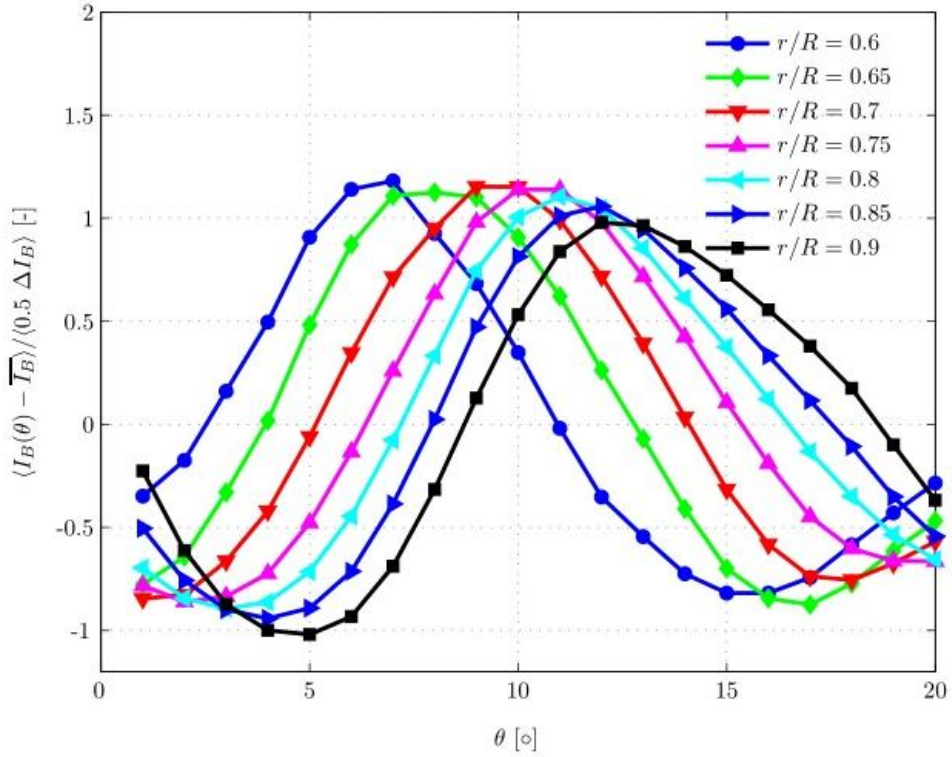

(a)

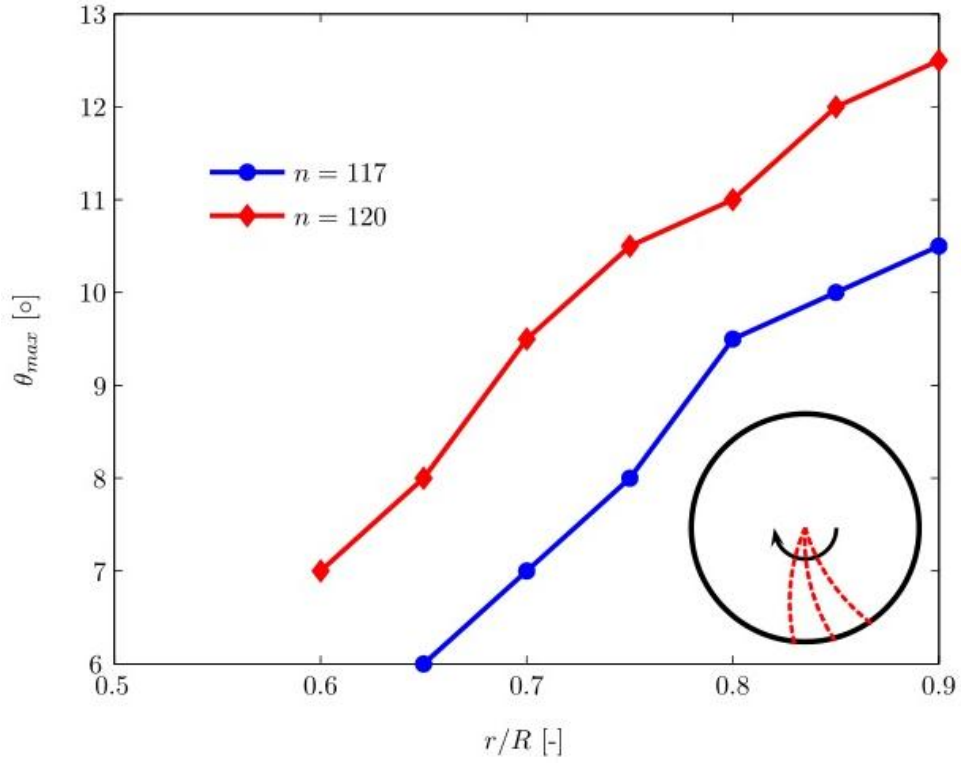

(b)

Figure 5.4: (a) Phase-averaged azimuthal profiles of the image brightness at n = 117 for different radii (r/R = 0.6 − 0.9); (b) Radial and azimuthal coordinates of the brightness peak for n = 117 and 120 (d_o = 2 cm, h = 3 cm, c = 2.5 g/L).

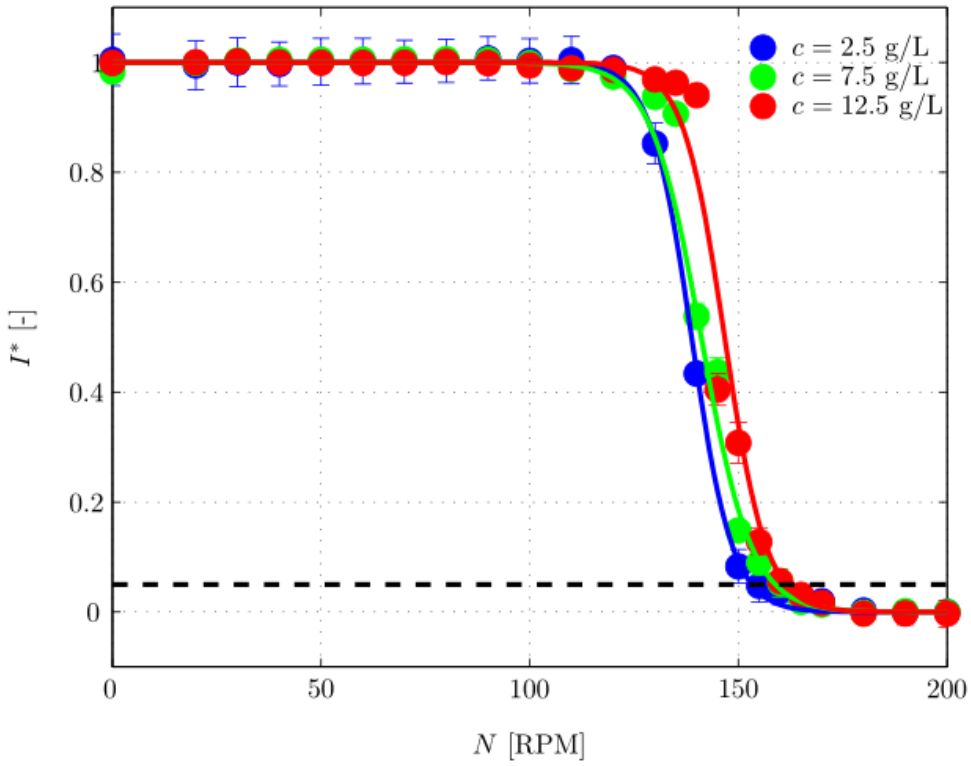

(a)

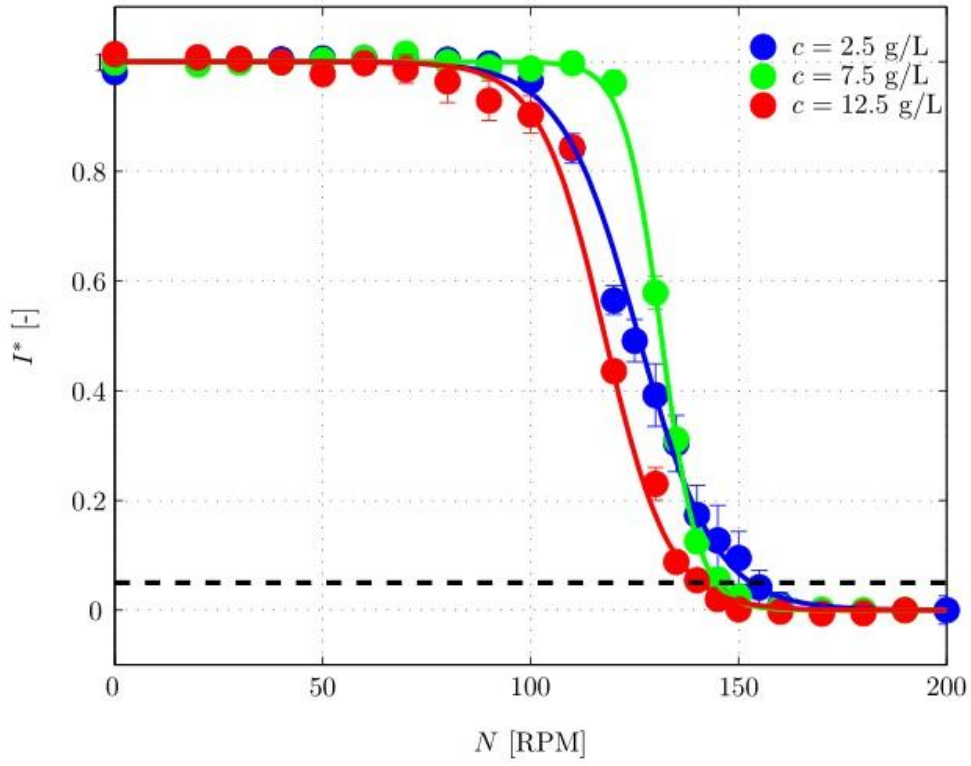

(b)

Figure 5.5: Variation of I^* with shaker speed for different microcarriers' concentrations (h = 5 cm, d_i = 7 cm): (a) d_o = 1.5 cm; (b) d_o = 2.5 cm.

On the contrary the variation of the suspension speed with the orbital diameter is significant.

This is evident in Figure 5.6 a where the normalised brightness index, I^* , is plotted against the shaker speed for different orbital diameter, d_o = 1.5, 2.5 and 5 cm. As expected the suspension speed, N_s , increases with decreasing orbital diameter, and assumes values of 120 RPM, 144 RPM and 153 RPM for d_o =5 cm 2.5 cm and 1.5 cm, respectively. In Figure 5.6 b an attempt was made to assess whether the suspension mechanism would scale with the critical Froude number ratio, Fr/Fr_{cr} . In fact the three systems are associated to different d_o/d_i and therefore reach the flow transition at different speeds (Weheliye et al., 2013). However the plot of Figure 5.6 b does not support this scaling procedure with the lowest (highest) orbital diameter still being associated to the greatest (lowest) critical Froude number ratio. This was explained by considering that the fluid height (h = 5 cm) of two, d_o = 1.5 cm and 2.5 cm, out of the three systems investigated is too large for the flow to fully develop to the cylinder bottom before transition occurs. In both cases $h/d_i > \sqrt{d_o/d_i}$ (0.71 > 0.46 for d_o = 1.5 cm and 0.71 > 0.59 for d_o = 2.5 cm) and Equation 5.2 shall be used to determine the critical Froude number, Fr_{cr}. Based on these considerations a second set of measurements was carried out to assess the suspension process when $h/d_i \leq \sqrt{d_o/d_i}$, and a critical speed exists for the flow to extend to the bottom of the reactor. The variation of I^* with d_o is provided in Figures 5.7 a and b for increasing speed and critical Froude number ratio, respectively. In agreement with Figure 5.6 a the plots of Figure 5.7 a intercept the 5% reference line at increasing suspension speed for decreasing orbital diameter. In this case however when the brightness index is plotted against the critical Froude number ratio (see Figure 5.7 b) the data tend to collapse on a single curve, indicating that the parameter Fr/Fr_{cr} can be successfully used for scaling across different configurations (i.e. d_o/d_i), provided that the fluid height satisfies the condition $h/d_i \leq \sqrt{d_o/d_i}$.

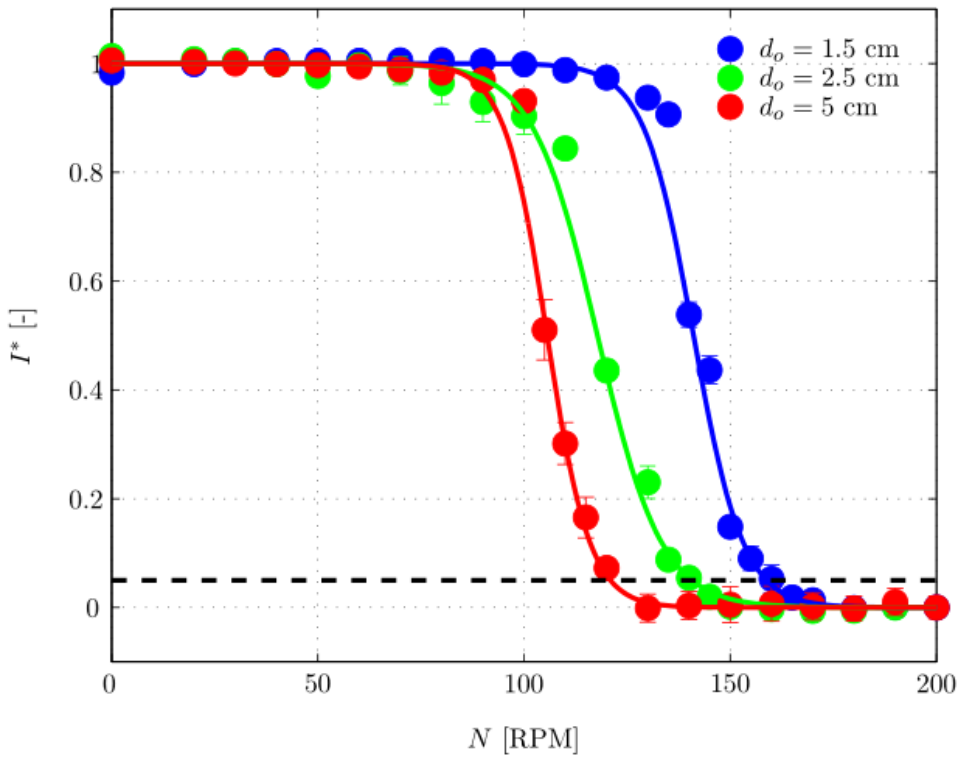

(a)

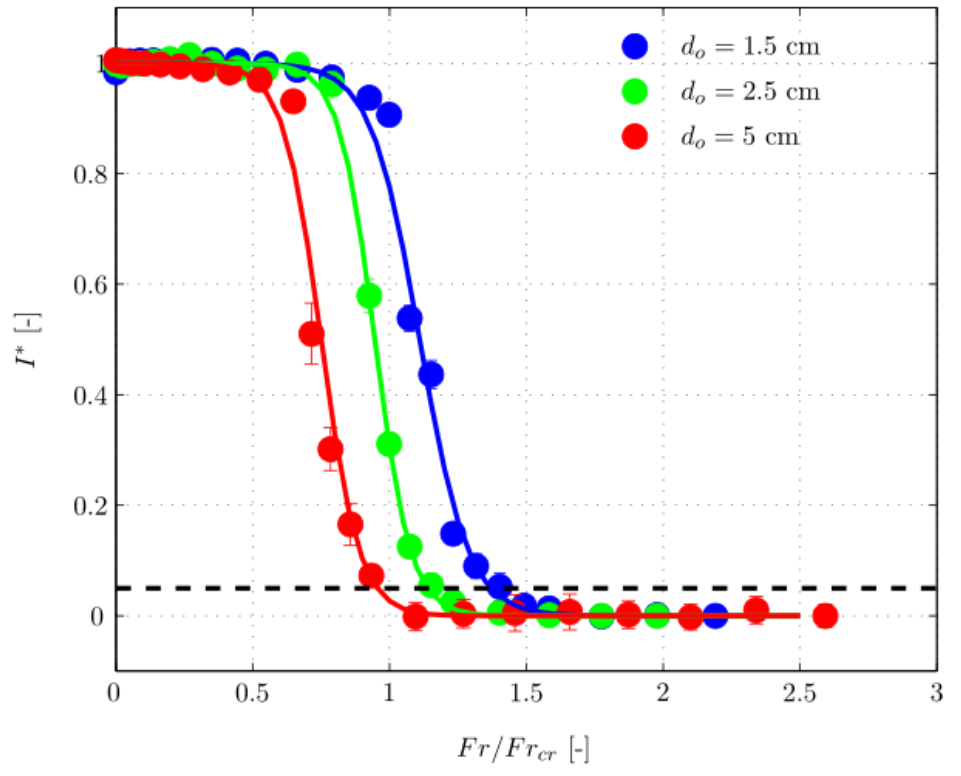

(b)

Figure 5.6: Variation of I^* for different orbital diameters (h = 5 cm, d_i = 7 cm, c = 2.5 g/L): (a) variation with shaker speed, N; (b) variation with Fr/Fr_{cr}.

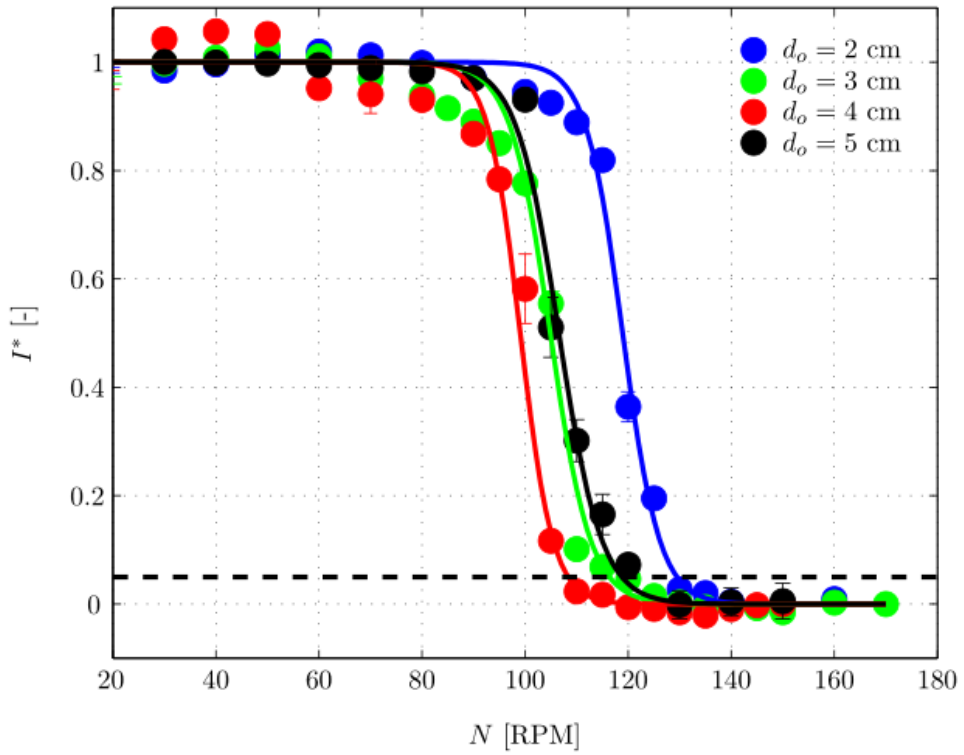

(a)

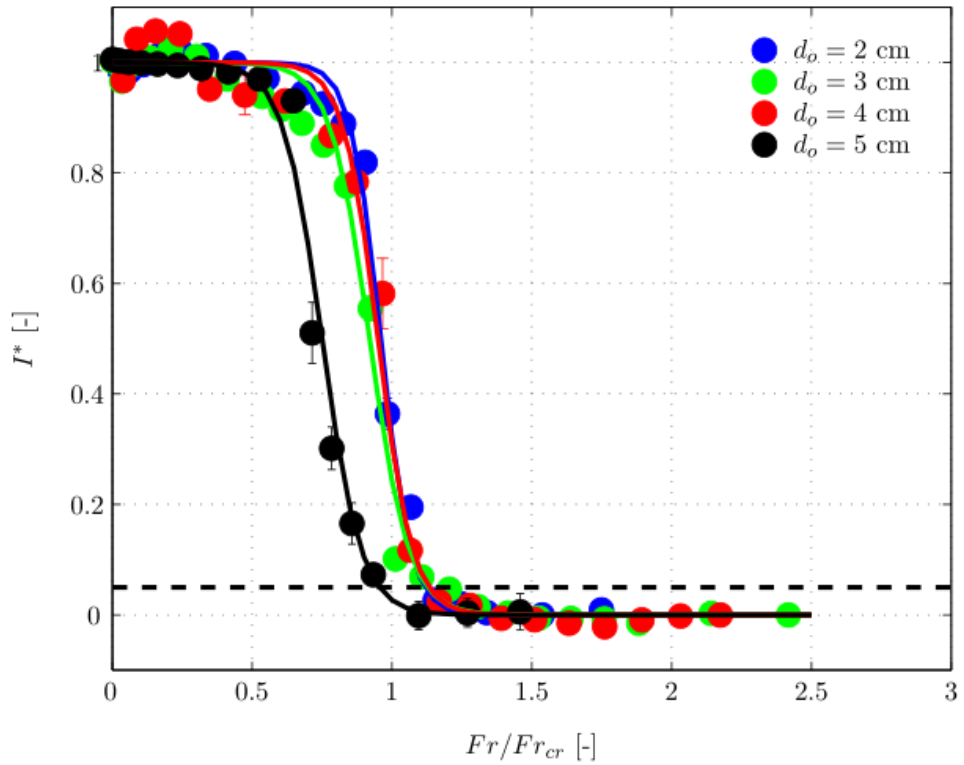

(b)

Figure 5.7: Variation of I^* for different orbital diameters (h = 3 and 5 cm, d_i = 7 cm, c = 2.5 g/L): (a) variation with shaker speed, N; (b) variation with Fr/Fr_{cr}.

The data presented in Figures 5.6 and 5.7 are summarised in Figure 5.8, where the suspended to critical Froude number ratio is plotted against the parameter $h/d_i \,/\, \sqrt{d_o/d_i}$. As indicated by the inset schematics values of $h/d_i \,/\, \sqrt{d_o/d_i} < 1$ identify those configurations for which the toroidal vortices extend to the bottom of the bioreactor when the critical speed is achieved, while this does not occur for $h/d_i \,/\, \sqrt{d_o/d_i} > 1$, and flow transition takes place without the flow developing to the reactor base. The error bars in Figure 5.8 are supposed to provide a reference, and correspond to a 2 RPM variation in the suspension speed N_s (i.e. $dFr_s/Fr_{cr} = 2 \times (N_s/N^2_{cr})dN_s$). From Figure 5.8, the 95 % suspension condition is achieved for $Fr_s/Fr_{cr} \leq 1.1$ when $h/d_i \,/\, \sqrt{d_o/d_i} < 1$, while the suspended to critical Froude number ratio tends to drift further away from the dashed reference line at $Fr_s/Fr_{cr} = 1.1$ as $h/d_i \,/\, \sqrt{d_o/d_i}$ increases above 1. It is interesting to note that the suspension speed data obtained by Olmos et al. (2015) in Erlenmeyer flasks showed a good scaling with the critical speed, N_{cr} , also for $h/d_i \,/\, \sqrt{d_o/d_i} > 1$.

The coefficients a and x_0 of Equation 5.6, used to determine the suspended to critical Froude number ratio (i.e. $Fr_s/Fr_{cr} = \log(19)/a + x_0$ for 95% suspension), are provided in Table 5.2. It is worth pointing that the range of variation of the decay coefficient for data associated to $h/d_i \,/\, \sqrt{d_o/d_i} > 1$ ($7 < a < 14.3$) is lower than that for $h/d_i \,/\, \sqrt{d_o/d_i} < 1$ ($14 < a < 17.8$). This implies that for $h/d_i \,/\, \sqrt{d_o/d_i} < 1$ suspension occurs more sharply with increasing speed.

	$h = 5$ cm								$h = 3$ cm		
	$d_o = 1.5$ cm			$d_o = 2.5$ cm			$d_o = 5$ cm		2 cm	3 cm	4 cm
	2.5 g/L	7.5 g/L	12.5 g/L	2.5 g/L	7.5 g/L	12.5 g/L	7.5 g/L	12.5 g/L	$c = 2.5$ g/L		
a	13.1	9.8	12.8	7.1	14.3	10	14	14.13	17.57	15.39	17.83
x_0	1.05	1.05	1.19	0.87	0.98	0.87	0.72	0.74	0.95	0.92	0.94
	$h/d_i/\sqrt{d_o/d_i} > 1$						$h/d_i/\sqrt{d_o/d_i} < 1$				

Table 5.2: Coefficients a and x_0 obtained for all the sets of data analysed in this work.

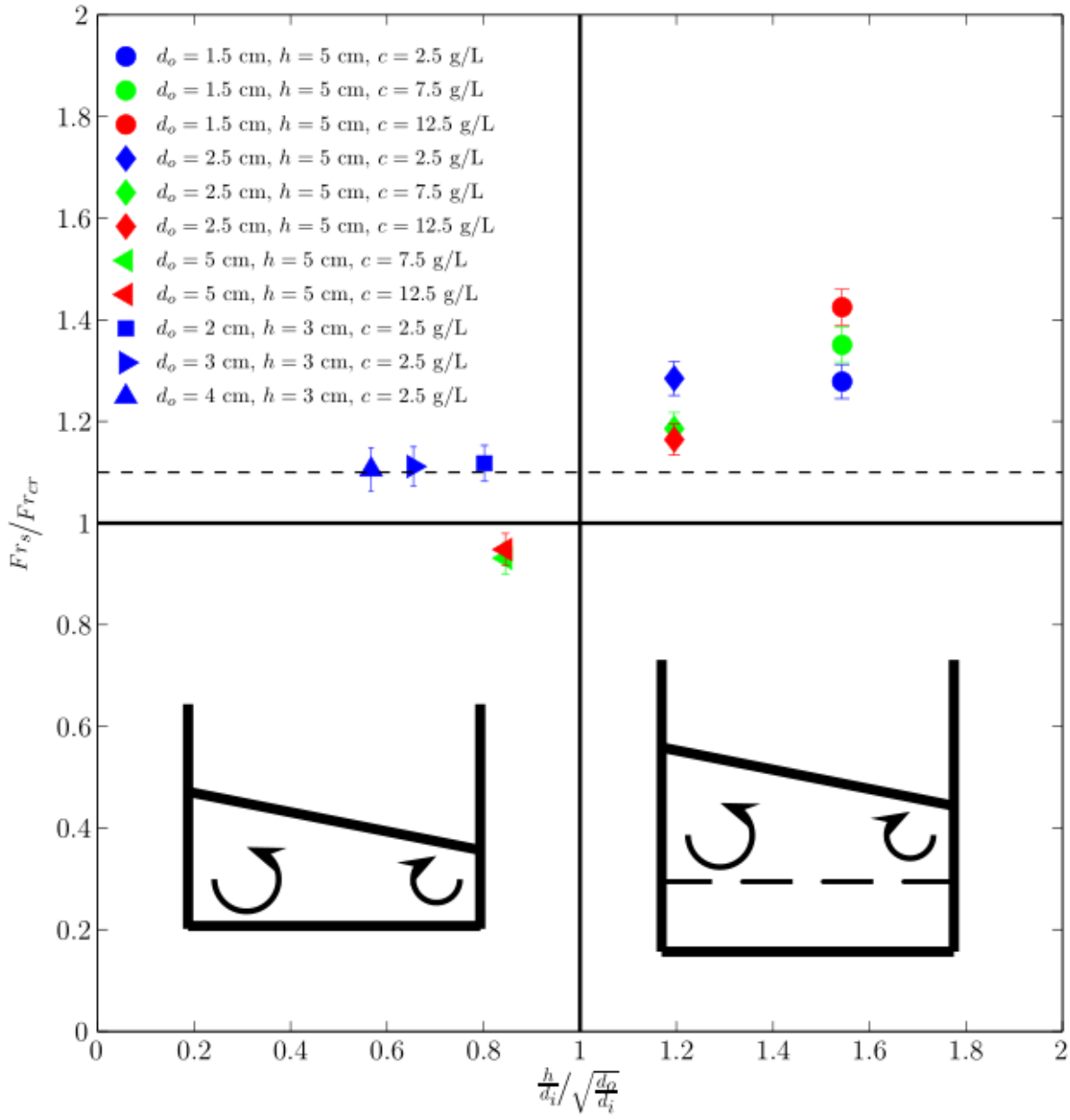

Figure 5.8: Variation of the suspended to critical Froude number ratio, Fr_s / Fr_{cr} , with critical height ratio, $h/d_i / \sqrt{d_o/d_i}$,for all the conditions investigated.

5.3.2 Microcarriers' dispersion

A similar analysis to that employed in the previous section was carried out over vertical planes of measurement to assess the dispersion across the bioreactor of the microcarriers' suspension. In this case the normalisation of the brightness index was done according to Equation 5.7, where the coefficient varies from 0 (low concentration of microcarriers' over the volume) to 1 (homogenous concentration across the bioreactor volume).

$$I^* = \frac{I_B(N) - I_B(0)}{I_B(\infty) - I_B(0)} \tag{5.7}$$

The variation of I^* with the critical Froude number ratio, Fr/Fr_{cr} , is provided in Figure 5.9, where inset snapshots provide a visual reference of the degree of dispersion. Data refer to a system with d_i = 13 cm, d_o = 5 cm and h = 6.5 cm ($h/d_i \,/\, \sqrt{d_o/d_i} < 1$). The vertical and horizontal lines provide a reference of the suspended to critical Froude number ratio, Fr_s /Fr_{cr} = 1.1, found in the previous section, and of the 95 % degree of homogeneity, respectively. From Figure 5.9 it can be concluded that complete dispersion is achieved at a speed slightly higher than the suspended one, $\approx 1.2 \times Fr_{cr}$ (95 % threshold).

A closer view at the dispersion of microcarriers across the tank can be gained from the axial and radial cumulative brightness profiles of Figures 5.10 a and b, respectively (d_i = 10 cm, $d_o = h$ = 5 cm). The axial (radial) cumulative brightness was obtained by adding the image brightness along the radial (axial) direction. Before proceeding with the discussion, it is worth mentioning that a limitation of adopting the brighness index as a reference for microcarriers' concentration is that in the vertical plane of measurements the laser enters the bioreactor from the base, and therefore complete brightness homogeneity is impossible to achieve due to reflections. This explains why brightness maxima are always located at z = 0, even at the higher speed investigated, when microcarriers' suspension has certainly occurred. Despite this the current data provide a reliable description of the suspension over a vertical plane for increasing speed.

Bearing this in mind, the plot of Figure 5.10 a shows that the axial distribution of microcarriers is poor for $N \leq 100$ with the normalised brightness index, $I_B\,(z,N)/I_B\,(0,N)$, being relatively low for $z/d_i \leq 0.04$, while, in agreement with the higher decay coefficients observed in Table 5.2 for $h/d_i \,/\, \sqrt{d_o/d_i} < 1$, a sharp change in $I_B\,(z,N)/I_B\,(0,N)$ occurs over a relatively small range of shaker speeds, N = 100−105 RPM. The curves of N = 105 RPM and N = 130 RPM are nearly parallel for

$z/d_i \geq 0.06$ indicating that a similar degree of dispersion along the axial direction has been achieved for both, while the lower intensity of $I_B\ (z,N)/I_B\ (0,N)$ indicates that fewer microcarriers are suspended for the lower speed considered.

Similarly to the axial profiles, the radial profiles of the cumulative brightness index, $(I_B\ (z,N) - I_B\ (0,N))/I_B\ (0,N)$, Figure 5.10 b, show little suspension for $N < 102$, while at greater speeds the radial distribution is characterised by double crested profiles, where the peaks capture the higher microcarriers' concentration already present in the top-right inset of Figure 5.9. The peaks are located close to the reactor axis and they occur in the region swept by the precessional vortex once flow transition has occurred. Based on these results and those in the previous section it can be concluded that microcarriers are pushed from the periphery towards the centre of the reactor base, and they are then sucked into the bulk flow by the depression created close to the axis of the bioreactor by the two-counter rotating and precessional vortices, before and after flow transition, respectively.

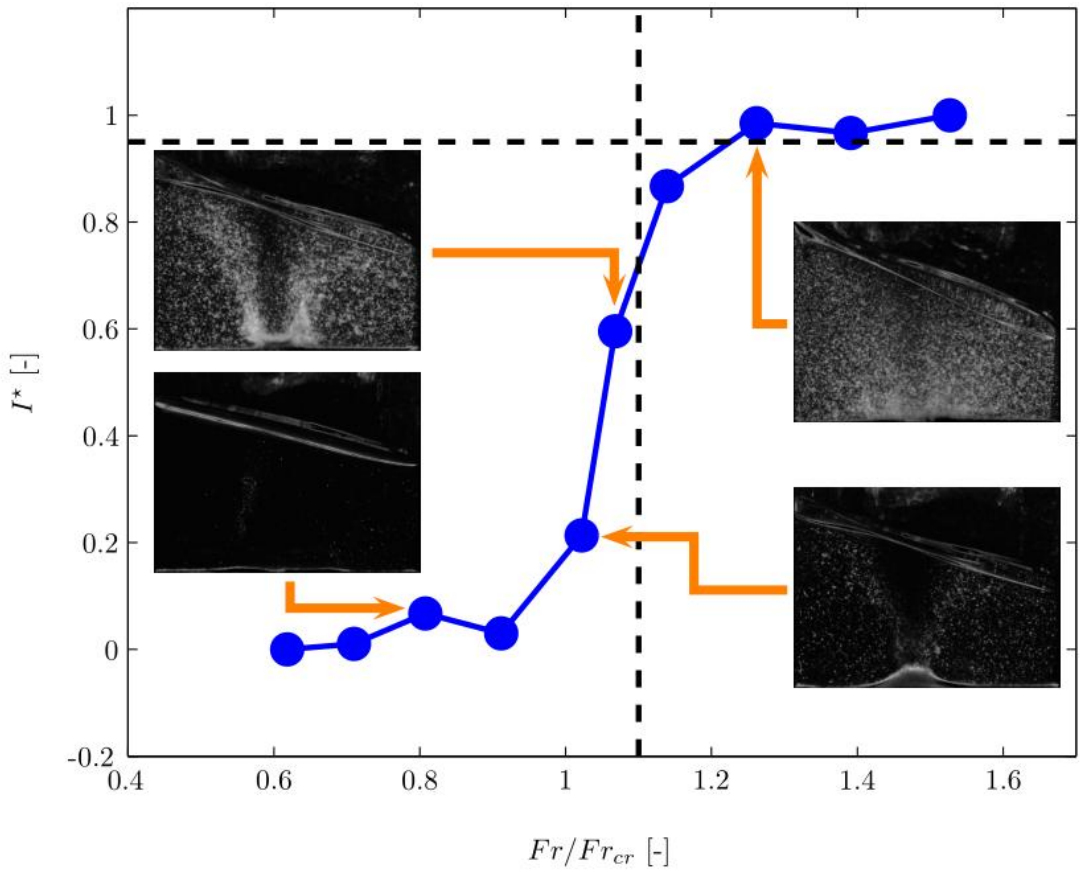

Figure 5.9: Variation of the normalised brightness index, I^* , with the Froude number ratio, $Fr\ /\ Fr_{cr}$, obtained from measurements on a vertical plane (d_i = 13 cm, d_o = 5 cm, h = 6.5 cm).

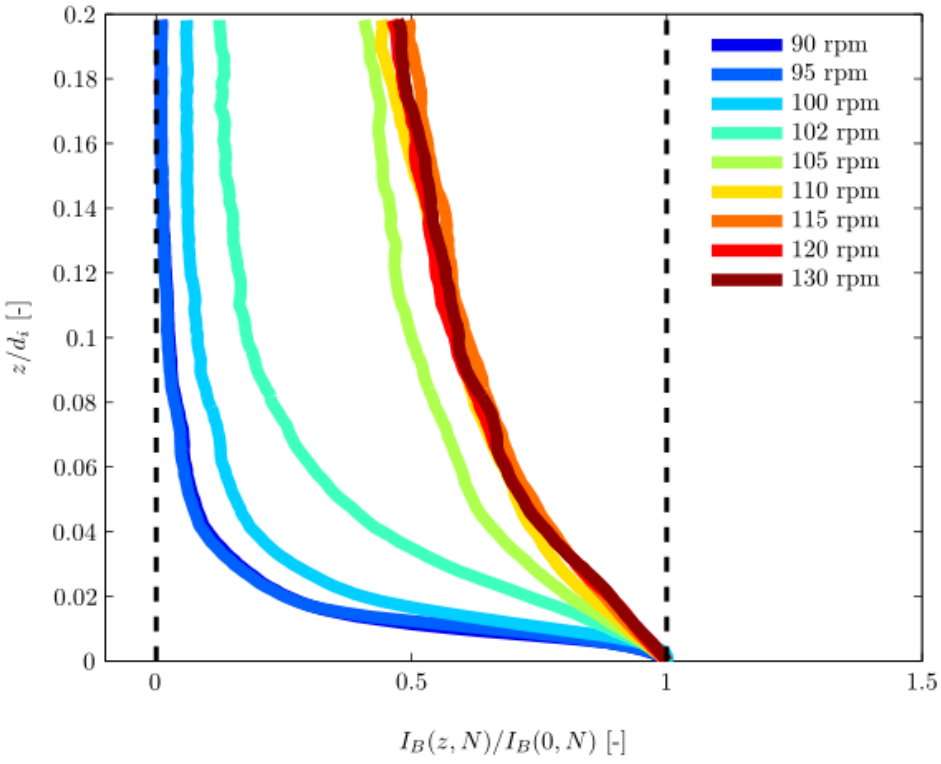

(a)

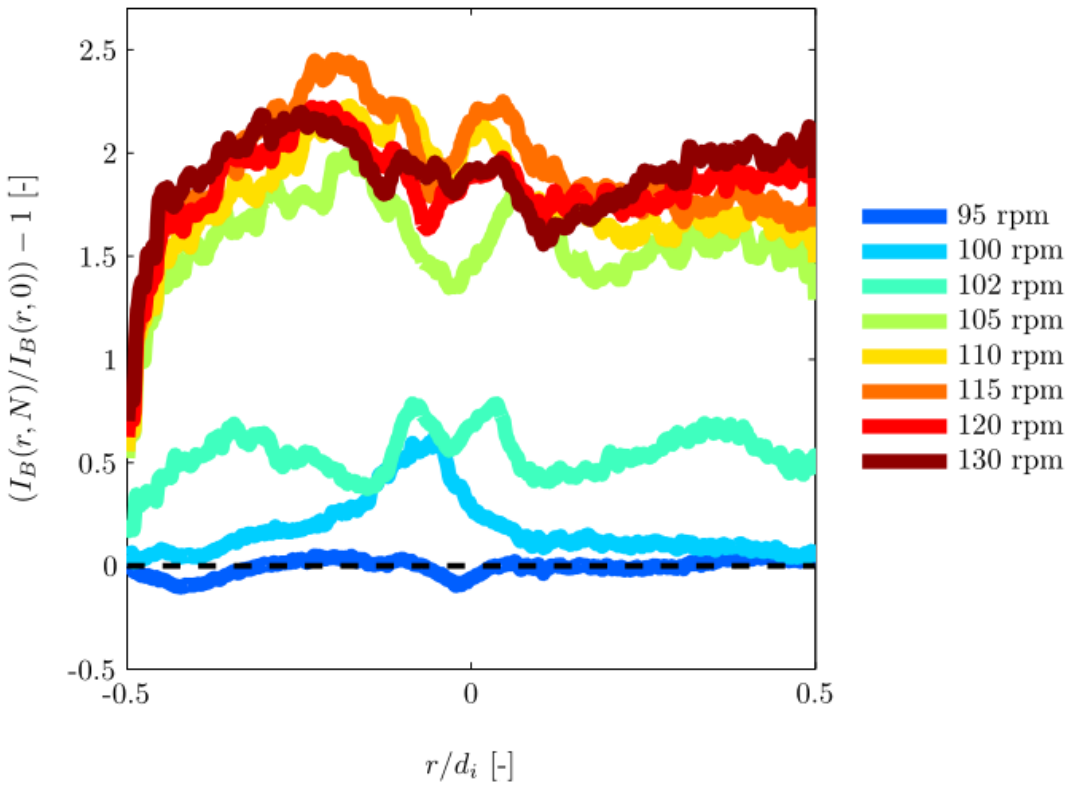

(b)

Figure 5.10: Profiles of the axial and radial cumulative brightness indices for increasing shaken speed (d_i = 10 cm, d_o = 5 cm, h = 5 cm): (a) Axial profiles; (b) Radial profiles.

5.3.3 Two-phase flow dynamics

Two-phase Particle Image Velocimetry experiments were carried out to better understand the influence of the solid phase on the mean characteristics of the flow, and to assess whether the flow transition reported by Weheliye et al. (2013) can be extended to the two-phase system. A preliminary analysis was carried out to assess whether the free surface wave, which is the flow driving mechanism, is affected by the microcarriers' concentration. The study of Weheliye et al. (2013) showed that for a single-phase system the nondimensional wave amplitude, $\Delta h/d_i$, is proportional to the Froude number, meaning that for selected combinations of N and d_o , the free surface will assume a fixed inclination, which is independent of the fluid height h and vessel diameter, d_i . The constant of proportionality, a_o , depends on the fluid considered, and is equal to 1.4 in the case of water, and decreases with increasing fluid viscosity (Ducci and Weheliye, 2014). The variation of $\Delta h/d_i$ against Fr ($0.25 < Fr < 0.5$) for different microcarriers' concentrations at $h/di = 0.5$, and $d_o /d_i = 0.5$ is provided in Figure 5.11. The data points are all located close to the reference line, which corresponds to a single-phase system with water as the working fluid ($a_{ow} = 1.4$). A small decrease of the slope might be seen for increasing microcarriers' concentrations, that is consistent with the behaviour reported by Ducci and Weheliye (2014) for increasing viscosity. This means that the flow dynamics of the two-phase system is not remarkably affected by the presence of microcarriers at the concentration considered, and that the applicability of the relation found by Weheliye et al. (2013) can be extended to the two-phase system. Lower values of the slope coefficient, a o , might imply that the critical Froude number for the two-phase system is slightly higher than that of the single-phase (see Equation 5.1), and therefore the suspended speed data points of Figure 5.8 might get closer to the horizontal reference line of $Fr/Fr_{cr} = 1$.

The phase-resolved velocity vector fields and tangential vorticity, $\omega_\theta/(\pi N)$, contour maps of the liquid and solid phases are shown in Figure 5.12 (a-b) and (c-d) for in-phase, prior to flow transition, and out-of-phase conditions, respectively. For both flow conditions the phase angle was $\varphi = 0$ and the microcarriers' concentration, $c = 0.5$ g/L. The velocity fields of the liquid and solid phases for in-phase flow (Figures 5.12 a and b) are qualitatively similar to each other, and are characterised by the two vortical cell configuration already identified by Weheliye et al. (2013) at the same speed for single-phase flow. However, in the toroidal vortex region, the vorticity of the solid phase assumes values slightly higher than for the liquid one (mainly on the left hand side vortex), indicating that a slip velocity is present between the two phases. Similar conclusions can be drawn when comparing the velocity fields for the out of phase flow (Figures 5.12 c and d). In this

case the axial slip velocity, $|u_{zS} - u_{zL}| < 0.02 \times \pi N d_o$ (0-6 mm/s). It is worth mentioning that this range of values is comparable to the average and maximum velocities of the liquid phase over the plane of measurement, 0.033 and $0.10 \times \pi N d_o$, respectively.

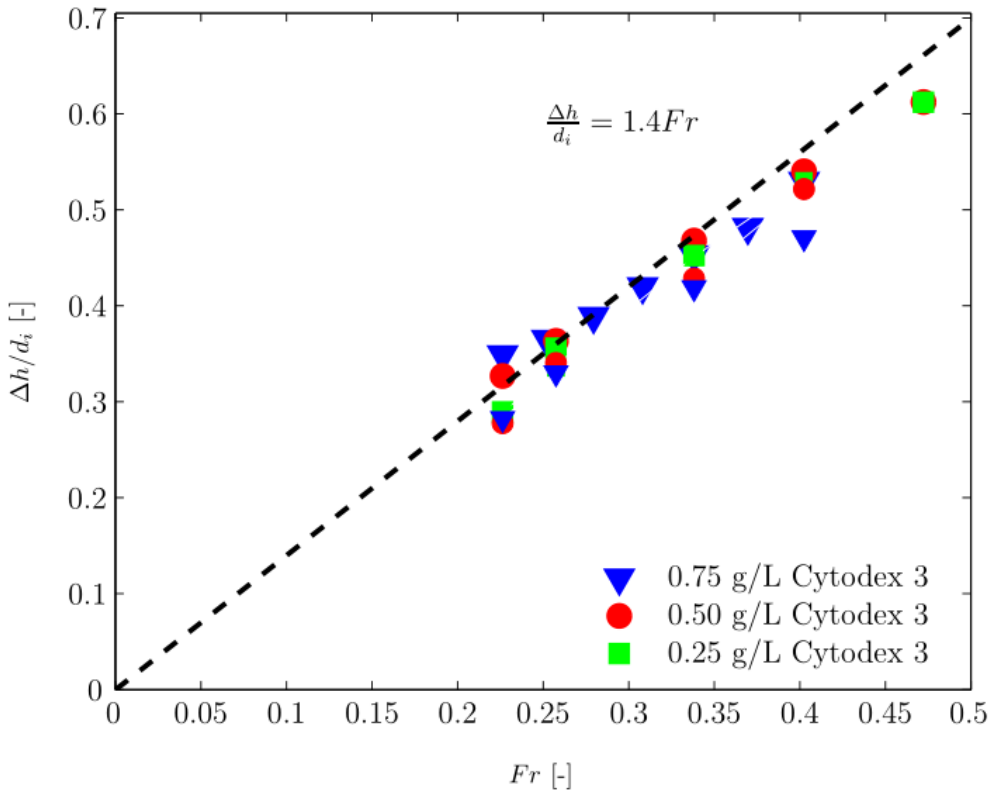

Figure 5.11: (a) Variation of the non-dimensional wave amplitude, $\Delta h/d_i$, with Froude number, $_{\mathrm{Fr,}}$ for different microcarriers' concentrations (h = 5 cm, d_i = 10 cm, d_o = 5 cm).

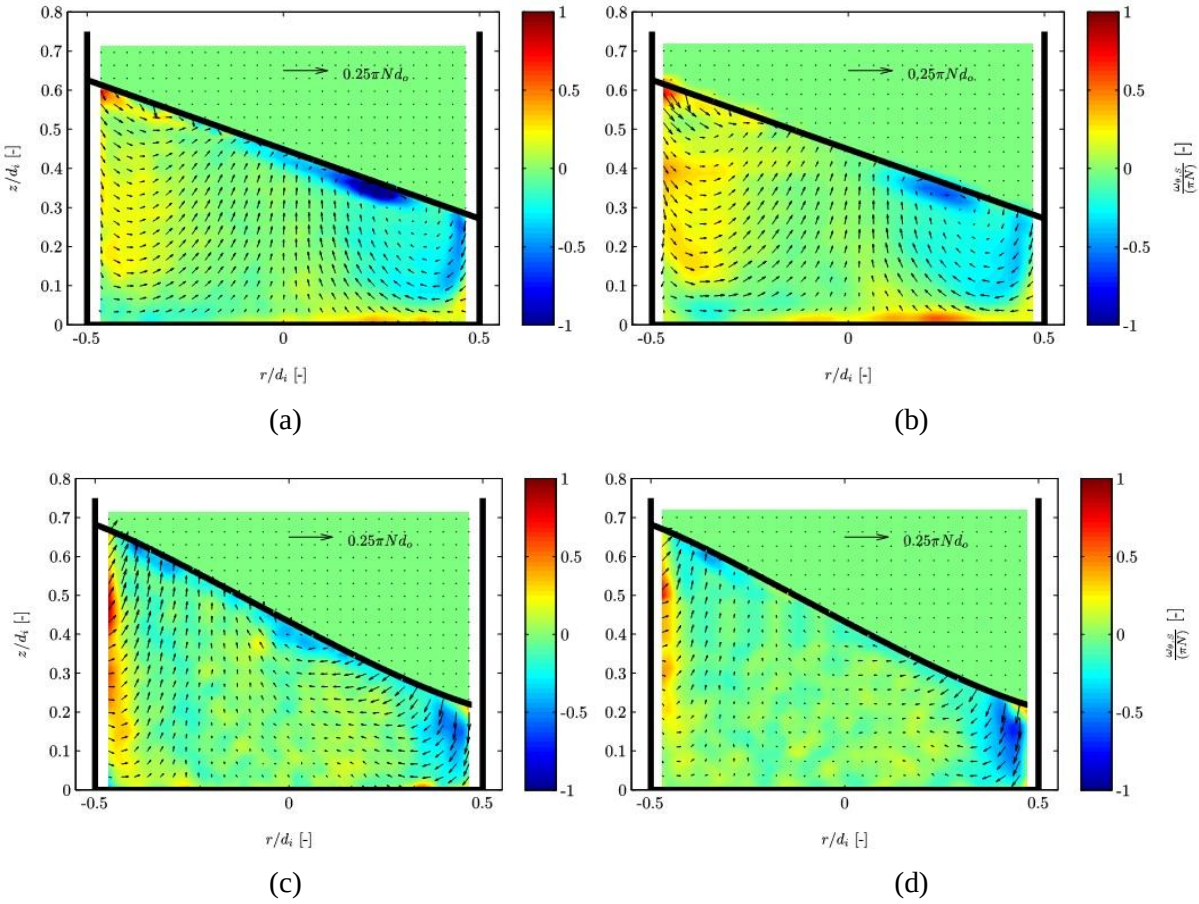

Figure 5.12: (a) Velocity vector fields and tangential vorticity contour maps of the liquid and solid phases before and after flow transition (h = 5 cm, d_i = 10 cm, d_o = 5 cm, c = 0.5 g/L): (a) Liquid phase, N = 90 RPM; (b) Solid phase, N = 90 RPM; (c) Liquid phase, N = 110 RPM; (d) Solid phase, N = 110 RPM.

5.4 Conclusions

This study is the first one to provide insight on the two-phase flow dynamics occurring in an orbitally shaken bioreactor when microcarriers are used in suspension under real process conditions. The suspension dynamics of the two-phase system was investigated using a visualization approach, which allowed to estimate the "just - suspended" shaking speed from the light scattered by the microcarriers on a laser plane parallel to the bottom of the cylindrical bioreactor. The shaking system was studied varying solid concentration and orbital diameter, and the results highlightened the correlation between the microcarriers suspension and the critical Froude number corresponding to the occurrence of the flow transition identified by Weheliye et al. (2013) for a single-phase system. It was found that for bioreactor configurations corresponding to $h/d_i \,/\, \sqrt{d_o/d_i} < 1$ the suspended Froude number, Fr_s , is nearly constant and equal to 1.1×Fr_{cr} , while for $h/d_i \,/\, \sqrt{d_o/d_i} > 1$ the suspended speed tends to increase, and suspension is delayed to higher speeds after flow transition. From this point of view the first type of configuration should be sought because it achieves full suspension and at the same time minimises power consumption and shear rates.

An analysis of the suspension mechanisms highlighted that microcarriers are pushed from the perisphery towards the centre of the reactor base along a spiral pattern, and then they are sucked into the bulk flow by the depression created close to the axis of the bioreactor by the two-counter rotating and precessional vortices, before and after flow transition, respectively. Vertical plane measurements were used to assess the homogeneity of the microcarriers across the reactor volume, and it was found that full dispersion is achieved at ≈ 1.2 × Fr_{cr} . A model was developed to fit the suspension data, and showed that suspension dynamics are faster and occur over a narrower range of speeds for $h/d_i \,/\, \sqrt{d_o/d_i} < 1$. The free surface experiments validated the relation found by Weheliye et al. (2013) between the non-dimensional wave amplitude of the cylindrical bioreactor, $\Delta h/d_i$, and the Froude number, and it was found that the presence of the microcarriers might reduce the constant of proportionality between the two parameters, and result in slightly higher critical Froude number, Fr_{cr}. The velocity fields of the liquid and solid phases were simultaneously measured over a vertical plane bisecting the vessel, and their mean flows were found to be very similar both for in-phase and out-of-phase conditions. This is in agreement with previous studies on stirred tank reactors where low solid concentrations are employed. The range of variation of the axial slip velocity, $|u_{z\,S} - u_{z\,L}| < 0.02 \times \pi N d_o$ (0-6 mm/s), was comparable in magnitude to the average and maximum velocities of the liquid phase over the plane of measurement, 0.033 and 0.10 × $\pi N d_o$, respectively.

Further studies are called for to investigate the suspension dynamics of the next generation of microcarriers. Biodegradable materials are increasingly used to make microcarriers for cell adherent applications in order to avoid the need for the cell detachment and recovery steps. However the materials used are often characterised by densities much heavier than water, thus requiring considerable energy to be suspended. The flow visualisation methodology established in this work, as well as the simultaneous measurement of the two-phase flow characteristics, could be implemented for other microcarriers' types to assess the quality of suspension, and its dependence on the bioreactor geometry and operating conditions.

5.5 References

Collignon, M.L.L., Delafosse, A., Crine, M., Toye, D., 2010. Axial impeller selection for anchorage dependent animal cell culture in stirred bioreactors: Methodology based on the impeller comparison at just-suspended speed of rotation. Chemical Engineering Science 65, 5929–5941.

Discacciati, M., Hacker, D., Quarteroni, A., Quinodoz, S., Tissot, S., Wurm, F.M., 2012. Numerical simulation of orbitally shaken viscous fluids with free surface. International Journal for Numerical Methods in Fluids , 1–14.

Ducci, A., Weheliye, W.H., 2014. Orbitally shaken bioreactors - Viscosity effects on flow characteristics. AIChE Journal 60, 3951–3968.

Ferrari, C., Balandras, F., Guedon, E., Olmos, E., Chevalot, I., Marc, A., 2012. Limiting cell aggregation during mesenchymal stem cell expansion on microcarriers. Biotechnology Progress 28, 780–787.

Frauenschuh, S., Reichmann, E., Ibold, Y., Goetz, P.M., Sittinger, M., Ringe, J., 2007. A microcarrier-based cultivation system for expansion of primary mesenchymal stem cells. Biotechnology Progress 23, 187–193.

GE Healthcare Life Sciences, 2013. Microcarrier Cell Culture-Principles & Methods. Technical Report.

Gomez, C., Bennington, C.P.J., Taghipour, F., 2010. Investigation of the Flow Field in a Rectangular Vessel Equipped With a Side-Entering Agitator. Journal of Fluids Engineering 132, 051106.

Ismadi, M.Z., Gupta, P., Fouras, A., Verma, P., Jadhav, S., Bellare, J., Hourigan, K., 2014. Flow characterization of a spinner flask for induced pluripotent stem cell culture application. PloS one 9, e106493.

Kim, H.M., Kizito, J.P., 2009. Stirring Free Surface Flows Due To Horizontal Circulatory Oscillation of a Partially Filled Container. Chemical Engineering Communications 196, 1300–1321.

King, J.A., Miller, W.M., 2007. Bioreactor development for stem cell expansion and controlled differentiation. Current Opinion in Chemical Biology 11, 394–398.

Lara, A.R., Galindo, E., Ram´ ırez, O.T., Palomares, L.A., 2006. Living with heterogeneities in bioreactors: understanding the effects of environmental gradients on cells. Molecular biotechnology 34, 355–381.

Liu, N., Zang, R., Yang, S.T., Li, Y., 2014. Stem cell engineering in bioreactors for large-scale bioprocessing. Engineering in Life Sciences 14, 4–15.

Mancilla, E., Palacios-Morales, C.A., Córdova-Aguilar, M.S., Trujillo-Rold´ an, M.A., Ascanio,G., Zenit, R., 2015. A hydrodynamic description of the flow behavior in shaken flasks. Biochemical Engineering Journal 99, 61–66.

Mohamet, L., Lea, M.L., Ward, C.M., 2010. Abrogation of E-cadherin-mediated cellular aggregation allows proliferation of pluripotent mouse embryonic stem cells in shake flask bioreactors. PloS one 5, e12921.

Nienow, A.W., Rafiq, Q.A., Coopman, K., Hewitt, C.J., 2014. A potentially scalable method for the harvesting of hMSCs from microcarriers. Biochemical Engineering Journal 85, 79–88.

Olmos, E., Loubiere, K., Martin, C., Delaplace, G., Marc, A., 2015. Critical agitation for microcarrier suspension in orbital shaken bioreactors: Experimental study and dimensional analysis. Chemical Engineering Science 122, 545–554.

Reclari, M., Dreyer, M., Tissot, S., Obreschkow, D., Wurm, F.M., Farhat, M., 2014. Surface wave dynamics in orbital shaken cylindrical containers. Physics of Fluids 26.

Rodriguez, G., Anderlei, T., Micheletti, M., Yianneskis, M., Ducci, A., 2014. On the measurement and scaling of mixing time in orbitally shaken bioreactors. Biochemical Engineering Journal 82, 10–21.

Rodriguez, G., Weheliye, W., Anderlei, T., Micheletti, M., Yianneskis, M., Ducci, A., 2013. Mixing time and kinetic energy measurements in a shaken cylindrical bioreactor. Chemical Engineering Research and Design 91, 2084–2097.

Sart, S., Schneider, Y.J., Agathos, S.N., 2009. Ear mesenchymal stem cells: an efficient adult multipotent cell population fit for rapid and scalable expansion. Journal of biotechnology 139, 291–299.

Schop, D., Janssen, F.W., Borgart, E., de Bruijn, J.D., van Dijkhuizen-Radersma, R., 2008. Expansion of mesenchymal stem cells using a microcarrier-based cultivation system: growth and metabolism. Journal of tissue engineering and regenerative medicine 2, 126–135.

Schop, D., Janssen, F.W., van Rijn, L.D.S., Fernandes, H., Bloem, R.M., de Bruijn, J.D., van Dijkhuizen-Radersma, R., 2009. Growth, metabolism, and growth inhibitors of mesenchymal stem cells. Tissue Engineering - Part A 15.

Simaria, A.S., Hassan, S., Varadaraju, H., Rowley, J., Warren, K., Vanek, P., Farid, S.S., 2014. Allogeneic cell therapy bioprocess economics and optimization: single-use cell expansion technologies. Biotechnology and bioengineering 111, 69–83.

Storm, M.P., Orchard, C.B., Bone, H.K., Chaudhuri, J.B., Welham, M.J., 2010. Three-dimensional culture systems for the expansion of pluripotent embryonic stem cells. Biotechnology and bioengineering 107, 683–695.

Tissot, S., Farhat, M., Hacker, D.L., Anderlei, T., Kühner, M., Comninellis, C., Wurm, F., 2010. Determination of a scale-up factor from mixing time studies in orbitally shaken bioreactors. Biochem. Eng. J. 52, 181–186.

Weheliye, W., Yianneskis, M., Ducci, A., 2013. On the Fluid Dynamics of Shaken Bioreactors - Flow Characterization and Transition. AIChE Journal 59, 334–344.

Zhang, H., Lamping, S.R., Pickering, S.C.R., Lye, G.J., Shamlou, P.A., 2008. Engineering characterisation of a single well from 24-well and 96-well microtitre plates. Biochem. Eng. J. 40, 138–149.

Zhang, H., Williams-Dalson, W., Keshavarz-Moore, E., Shamlou, P.A., 2005. Computational fluid-dynamics (CFD) analysis of mixing and gas-liquid mass transfer in shake flasks. Biotechnology and applied biochemistry 41, 1–8.

Zhang, X., Bürki, C.A.A., Stettler, M., De Sanctis, D., Perrone, M., Discacciati, M., Parolini, N., DeJesus, M., Hacker, D.L., Quarteroni, A., Wurm, F.M., 2009. Efficient oxygen transfer by surface aeration in shaken cylindrical containers for mammalian cell cultivation at volumetric scales up to 1000L. Biochem. Eng. J. 45, 41–47.

6 Appraisal of fluid flow in a shaken bioreactor with conical bottom at different operating conditions

6.1 Introduction

The pharmaceutical industry heavily relies on mammalian cells as host to manufacture biologics for the diagnosis and treatment of a variety of patient conditions, such as rheumatoid arthritis (Adalimumab), leukaemia (Ofatumumab), colonrectal cancer (Panitumumab) (Walsh, 2014; Zhang, 2010). Process development studies are typically performed at small scale in orbitally shaken reactors (OSRs), either in microwell plate format or Erlenmeyer flasks, offering an effective solution to screen several conditions in parallel using small volumes. Once the optimal parameters are identified, the process is commonly scaled up for manufacturing in larger stirred tank bioreactors (STRs). The scale translation from OSRs to conventional stirred tank reactors currently represents a bottleneck at the process development stage due to the significant differences in geometry and mixing dynamics, and has generated interest in large scale OSRs for facilitating bioprocess development. Production scale OSRs are now on the market (see for example Kühner OrbShake) allowing users to select the same bioreactor geometry at multiple scales, thus facilitating scaling-up and simplifying regulatory approval.

The flow dynamics inside OSRs were first studied by Gardner and Tatterson (1992), where dye visualization techniques were employed to assess the variation of the homogenization time with increasing Reynolds number, *Re*.

Büchs et al. (2001) were the first to report the 'out-of-phase' phenomenon present at certain conditions, when the liquid in the shaken flask does not move in synchronization with the shaker table. Recently, Weheliye et al. (2013), Ducci and Weheliye (2014) and Rodriguez et al. (2014, 2013) provided a thorough insight into the flow dynamics inside a cylindrical shaken bioreactor with a flat bottom. From their work phase-resolved velocity maps at low Froude number (*Fr*) showed the presence of two completely separated counter-rotating vortices when the free surface is at its maximum inclination on the vertical plane of measurement (ϕ = 0°). As the shaking speed, *N*, was increased, the counter-rotating vortices, often denoted as toroidal vortex to characterize the three dimensionality of the flow, were observed to extend towards the bottom of the cylindrical bioreactor and increase in magnitude. When *N* was further increased, a mean flow transition was observed, with the flow being dominated by an axial vortex precessing around the axis of the

bioreactor. It was also observed that, at conditions before the onset of the flow transition, the free surface could be approximated by an ellipse, whilst at greater *N*, after flow transition, the free surface was highly three dimensional. Weheliye et al. (2013) derived a scaling law, which allows to calculate the conditions at which flow transition occurs for different bioreactor sizes, orbital diameter, filling volume and fluid viscosity. The expansion of the toroidal vortical cell from the free surface to the bioreactor base with increasing shaker speed found by Ducci and Weheliye (2014) and Weheliye et al. (2013) provides an explanation for the results of Tissot et al. (2010) and Rodriguez et al. (2014, 2013), who reported the presence of faster mixing in regions close to the surface and a diffusion-dominated zone close to the cylinder bottom for low values of *N*. Rodriguez et al. (2013) investigated the effect of feeding location on mixing time, and reported slower mixing when feeding occured inside the toroidal vortex, whilst mixing time decreased when additions were performed elsewhere in the bioreactor.

The mentioned flow scaling law and fluid dynamics studies of shaken systems are limited to cylindrical and flask geometries, but several other designs have been proposed in the literature in an attempt to improve process mass transfer at different scales. For example, at small scale, a 6-petaled flower shape cross-section micro-titre plate geometry was found to be the most promising among all the proposed designs (Funke et al., 2009). At large scale, V_f = 50–1500 L Zhang et al. (2008) proposed a novel bioreactor configuration, where helical tracks were positioned on the cylindrical walls resulting in 10-fold increases in mass transfer in comparison to unbaffled cylinders. Monteil et al. (2013) investigated a shaker tube with a bottom equipped with a downward cone, reporting that a higher shaking speed was required to obtain the same mixing times as a flat bottom cylinder having a similar diameter.

The research of Tissot et al. (2010) and Rodriguez et al. (2014, 2013) highlighted the presence of poor mixing regions and low flow activity at the bottom of the vessel. This is a drawback for those applications based on microcarrier suspensions, which are essential for cultivation of cells not yet adapted to suspended cultures, such as legacy cell lines and stem cells. From this point of view the recent study of Pieralisi et al. (2015) has shown that microcarriers tend to accumulate at the centre of the bioreactor when a flat bottom geometry is considered.

Cells cultured in a bioreactor are subject to mechanical stresses due to the fluid dynamics developing within the system; however in the published literature no agreement has been reached on the qualitative and quantitative effects of flow shear stresses on mammalian cells and their metabolism.

High shear forces at the air/liquid interphase in sparged bioreactors were reported to be detrimental to cell growth (Cherry and Hulle, 1992). Recent works by Nienow et al. (2013) proved that density

and product titre of CHO cells were not affected by industrially relevant shear stress levels, both in laminar converging devices and turbulent bioreactors stirred by Rushton turbines. A low shear environment caused by the use of controlled agitation rates, on the other hand, has been reported to affect cell viability, growth and metabolism (Aloi and Cherry, 1996; Elias et al., 1995; Keane et al., 2003). The effect of sub-lytic shear stresses was evaluated for baby hamster kidney (BHK) cells in terms of cell morphology and viability (Ludwig et al., 1992) and critical shear stress levels of 0.8 to 1 N m^{-2} were reported. In the prospect of stem cells grown in 3-dimensional microcarrier cultures, flow shear becomes crucial with respect to cell proliferation and lineage selection (Li et al., 2011). Hydromechanical damage on microcarrier cultured cells arises from inter-particles collisions and from turbulent eddies whose characteristic dimension is similar to the microcarrier size (Cherry and Papoutsakis, 1988).

Ismadi et al. (2014) investigated the effects of flow shear stresses on mouse induced pluripotent stem cells attached on microcarriers cultivated in spinner flasks and reported an agitation of 25 RPM and 7 days culture time as the optimal conditions. Nienow et al. (2014) developed a new method for the harvesting of human mesenchymal stem cell (hMSC) in a spinner flask. Their study indicates that intense agitation for a short period (7 min) under the presence of a suitable enzyme can promote cell detachment without damaging the cells or affecting their attributes, with an overall harvesting efficiency above 95%. Studies on the effect of shear stresses on mammalian and stem cell culture are generally limited to global considerations where cell population properties, such as product titre and cell viability, are related to global flow characteristics based on volume average velocity and hear stress. From this point of view a rigorous quantification of local shear stresses and their distribution in the bioreactor are crucial to better understand their effect on the process, and be able to design suitable operating conditions. This is especially important for novel technologies like stem cells and cells for therapy where shear sensitivity has not been fully investigated, and where the direction and magnitude of shear stresses have been found to have a major impact on cell expansion and differentiation into cell lineages (Sargent et al., 2010; Stolberg and McCloskey, 2009).

Studies on the flow in orbital shaken reactors have focused primarily on simple geometries, such as Erlenmeyer flasks or flat-bottomed cylinders. Efforts have been made to improve bioreactor performance through geometry modifications. Aeration, for example, was improved by the addition of baffles and/or modifications to the bioreactor wall and such changes have proven successful in increasing mass transfer rates at the liquid/air interface. Very few designs have been proposed aiming at improving solids suspension in OSRs. The critical agitation speed required for microcarrier suspension in Erlenmeyer flasks and cylindrical vessels was determined by Olmos et

al. (2015). Pieralisi et al. (2015) measured just suspended speed in cylindrical OSRs and found microcarriers settled at the centre of the vessel. In an attempt to address the aforementioned drawbacks of orbital shakers, different conical bottom geometries were investigated in this work to assess/compare their mean flow characteristics and potentials for solid suspension. A conical shaped bottom was employed in a cylindrical OSR in order to minimize the volume associated to poor mixing and flow recirculation (Rodriguez et al., 2013). The shear rate levels were quantified for all bottom geometries considered as such levels are crucial to understand whether orbital shaken bioreactors can be successfully used for shear-sensitive cells, like stem cells and cells for therapy, either in suspension or adherent to microcarriers.

6.2 Materials and Methods

The experimental apparatus comprised a glass cylinder with a transparent Perspex bottom characterized by an inner diameter, d_i, height, H, and wall thickness, t_c , of 100 mm, 250 mm and 5 mm, respectively, as shown in Figure 6.1. The cylinder was placed in a square acrylic trough to minimize refraction. A steel structure enclosed the trough and cylinder leaving the
top of the cylinder open. The gap between the trough and glass cylinder was filled with water to minimize refraction at the cylinder curved wall. Three bottom geometries were investigated in this work: flat, conical A (cone height, h_{cone} = 5 mm; angle from the horizontal, α_{cone} = 6.3°) and conical B (cone height, h_{cone} = 15 mm; angle from the horizontal, α_{cone} = 18.4°).
All the geometry characteristics are listed in Table 6.1. It should be noted that the conical bottoms used in this work were truncated cones, with a 10 mm upper face diameter. The bioreactor bottoms were manufactured on a lathe from a solid piece of Perspex and designed to be interchangeable on the cylindrical vessel. The manufacturing and polishing process allowed good optical access to the measurement area. Distilled water ($\upsilon = 10^{-6}$ m^2 /s) was used as working fluid. For all the conditions investigated, a fixed fill volume, V_f = 393 mL, was employed, corresponding to fluid heights at rest of h = 50 mm, 52 mm and 56 mm for the flat, conical A and conical B geometries, respectively. The bioreactor was secured to a benchtop L-SX shaker (Kühner AG Shaker) equipped with a Hall effect incremental encoder. The origin of the phase angular coordinate, ϕ, corresponded to the shaker being at the point furthest to the left along its clockwise circular orbit when seen from above. A magnet placed on the shaker drive triggered the Hall effect sensor at each revolution, when the vessel was at the phase angle ϕ = 0. The shaker rotational speed was varied in a range N = 80–130 RPM. The orbital diameter was d_o = 25 mm. A two-dimensional particle image velocimetry system (PIV) was employed to determine velocity characteristics and estimate the kinetic energy distribution and shear rates on a vertical plane of measurement passing through the axis of the

cylindrical vessel. The PIV system comprised a green diode laser, a cylindrical lens, a mirror and an intensified camera, which were rigidly mounted on the tray of the shaker table. The laser had 532 nm wavelength and an output power of 300 mW. The intensifier in the camera amplified the photons entering the camera lens, allowing short exposure times (5 ms) with the low power laser. The cylindrical lens created a 1 mm laser sheet. The mirror was placed below the bioreactor at a 45° angle so to reflect the laser sheet and illuminate the base along the vertical plane orthogonal to the camera. The timing box and magnetic encoder allowed to synchronize the image acquisition, and to obtain phase-resolved velocity data. Rhodamine-coated Polymethyl methacrylate spheres (50 μm) were used for the PIV measurements in conjunction with a 570 nm orange cut-off filter to minimize reflections of the laser.

Different sets of measurements were taken at angular positions $\phi = 0°$ and $\phi = 270°$, which are the most effective to characterize the flow. The same set up as that of Weheliye et al. (2013) was employed in this work so that the field of view corresponded to the r–z plane bisecting the cylinder along its longitudinal axis (see Figure 6.1). The data recorded with the intensified camera was processed using Dynamic Studio (Dantec Dynamics) with an adaptive correlation analysis of the full image for an initial interrogation window of 256 × 256 pixel

and a final window of 32 × 32 pixel. The adaptive correlation method is a multi-scale correlation approach, where velocity vectors estimated from larger interrogation area are used

as input to the next correlation step. In this way a preliminary velocity direction is estimated to compute the final vector fields corresponding to the final interrogation area. In the current analysis a 50% window overlap was used for a final resolution of 16 × 16 pixel, corresponding to an area of $1.3 \times 1.3\ mm^2$. Five hundred image pairs were recorded for

each experimental condition with a time delay of 10–20 ms between the two images used to estimate the instantaneous vector field. Data processing was carried out using purposely

written Matlab routines.

Bottom Geometry	d_i *[mm]*	h_{cone} **[mm]**	α_{cone} *[deg]*	d_o *[mm]*	h **[mm]**	N **[RPM]**
Flat	100	0	0	25	50	80 - 130
Conical A		5	6.3		52	
Conical B		15	18.4		56	

Table 6.1: Summary of bioreactor geometric parameters and operating conditions.

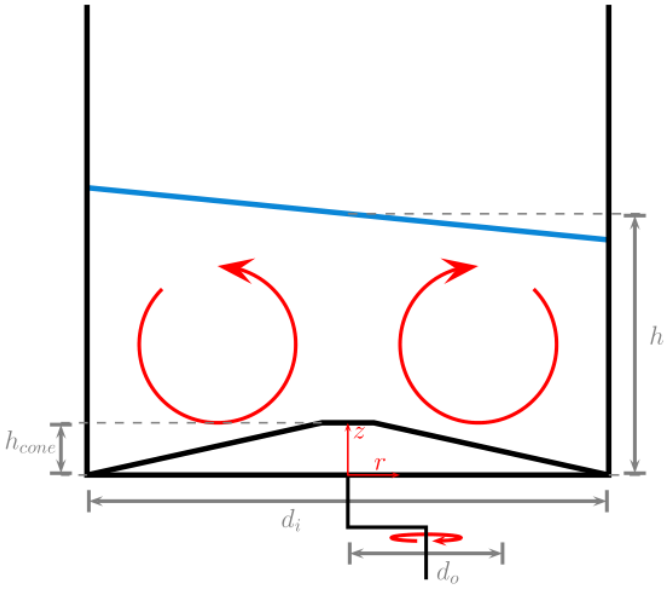

Figure 6.1: Cross-sectional view of the orbitally shaken cylindrical bioreactor with the novel cylindrical bottom.

6.3 Results and Discussion

The flow dynamics in a flat bottom cylindrical OSR have been described by Weheliye et al. (2013) and Rodriguez et al. (2013). This work builds upon those findings to investigate the effects of a conical bottom geometry on the flow in a cylindrical OSR. Section 6.1 investigates the impact of a conical bottom of two different heights on the development of the vortical structures described by Weheliye et al. (2013) and on the intensity of the space-averaged vorticity. The principal components of the strain rate tensor were estimated over the entire flow field for the flat and conical B bottom geometries and, together with the intensity and position of maximum strain rate, are reported in Section 6.2. Section 6.3 provides an account on how and to what extent conical bottom geometries affect the flow at a phase angle ϕ = 270°, which is characterized by a strong radial flow responsible for moving the fluid between opposite sides of the bioreactor (Rodriguez et al., 2013). Section 6.4 shows how the conical bottom geometry affects the intensity of kinetic energy for increasing Froude number. Different definitions of Froude number, based either on velocity or centrifugal acceleration, are available in the literature relevant to shaken systems. In this article the definition used by Büchs et al. (2001) and Ducci and Weheliye (2014), namely $Fr_{do} = 2\pi^2 N^2 d_o /g$, was adopted.

6.3.1 Effects of bottom design on flow dynamics and vorticity

Phase-resolved velocity fields and tangential vorticity contour maps were obtained for the three bottom geometries investigated. The velocity fields were measured at a phase angle ϕ = 0°. The vertical plane of measurement bisected the cylindrical bioreactor into two halves. The phase-resolved velocity fields were calculated using the following equation (Equation 6.1):

$$u\,(r,z,\phi) = \frac{\sum u\,(r,z,\phi)}{N_\phi} \tag{6.1}$$

where $u\,(r, z, \phi)$ is the instantaneous velocity field on the plane of measurement (r,z) and N_ϕ is the number of velocity fields obtained for each angular position, ϕ; in this work 500 image pairs were used to calculate the phase average u. The vorticity in the kth direction, ω_k, defined in Equation 6.2, was calculated from phase-averaged velocity fields on a two-dimensional grid using a central differentiation scheme:

$$\omega_k = \left(\frac{\partial u_i}{\partial x_j} - \frac{\partial u_j}{\partial x_i}\right) \tag{6.2}$$

where u_i and u_j indicate the velocity components in the ith and jth directions, respectively.

Velocity fields and vorticity contours are shown in Figure 6.2–4 for flat, 5 mm and 15 mm conical bottom cylinders, respectively. In all cases the data shown were obtained at shaking speeds N = 85, 100, 110 and 115 RPM and Fr = 0.10, 0.14, 0.17, 0.18 ((a)–(d)).

All vorticity contour maps were scaled according to the colour bar included in Figure 6.2–4(d). Regions with red hues indicate a positive value of vorticity and counter clockwise rotation, whilst those in blue are associated to negative vorticity and clockwise rotation.

Two counter-rotating vortical cells can be identified within the bulk of the fluid from all the vorticity contour maps considered. The cells represent a section of the toroidal vortex inclined below the free surface. In agreement with previous studies conducted using flat bottom bioreactors (Weheliye et al., 2013), the size of the vortical cells increases and expands from the free surface towards the cylinder bottom as Fr is increased.

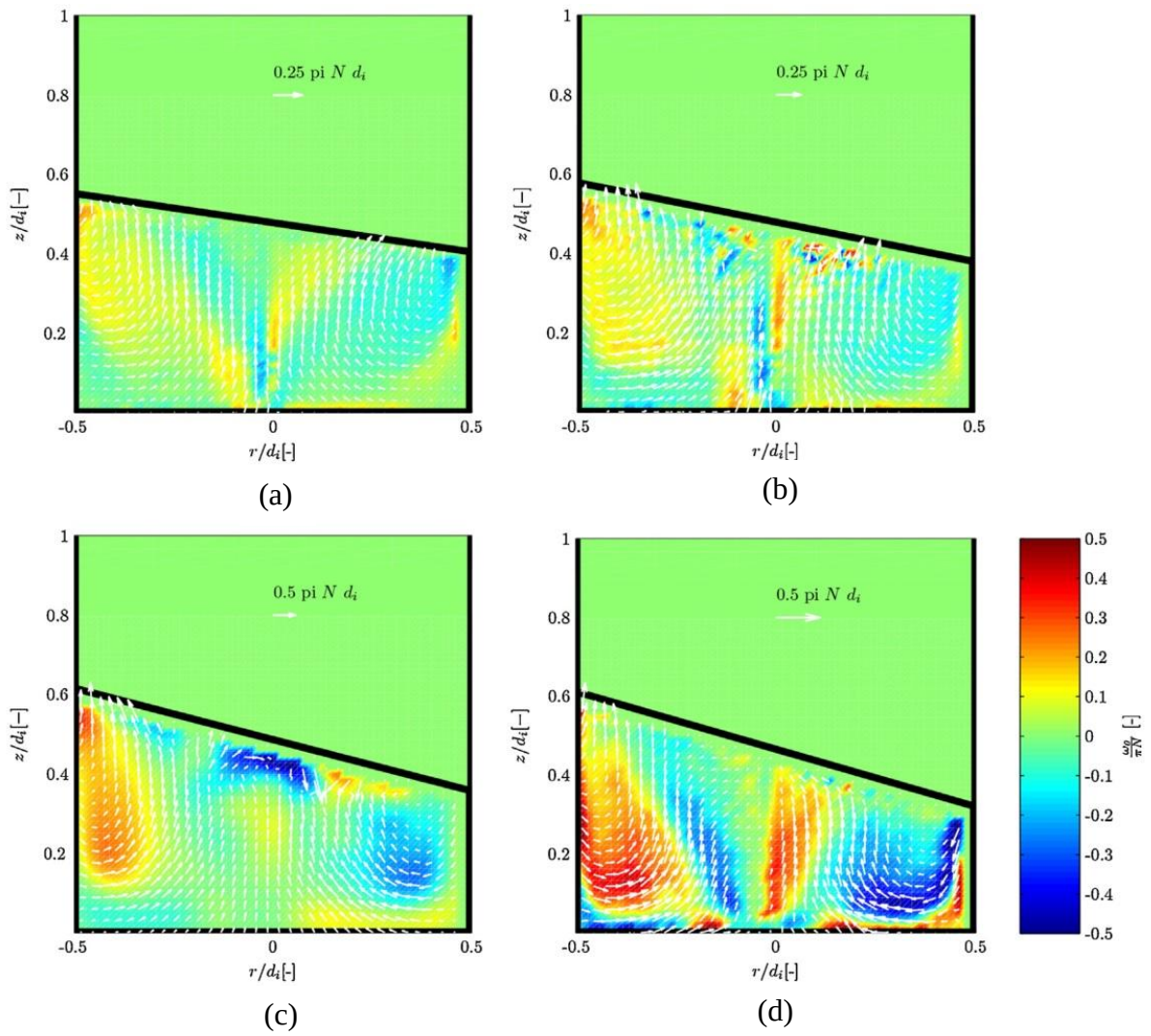

Figure 6.2: Phase-resolved non-dimensional velocity fields and contours of the tangential component of vorticity, ω_θ , for a flat bottom geometry at ((a)–(d)) Fr = 0.10, 0.14, 0.17, 0.18 (N = 85, 100, 110, 115 RPM).

Figure 6.2: (a) shows vortical cells present at a location close to the vessel walls and the free surface. As the shaking speed is increased the vortical cells increase in size and intensity, expanding towards the centre and bottom of the bioreactor (Figure 6.2 a–d), reaching the bottom at shaking speeds N > 110 RPM and Fr > 0.17 (Figure 6.2 d). The shaking speed at which flow transition occurs for the flat bottom bioreactor is in agreement with that indicated by Weheliye et al. (2013) for the geometrical configuration and operating conditions used in this study *(*h/d_i = 0.5 and d_o /d_i = 0.25).

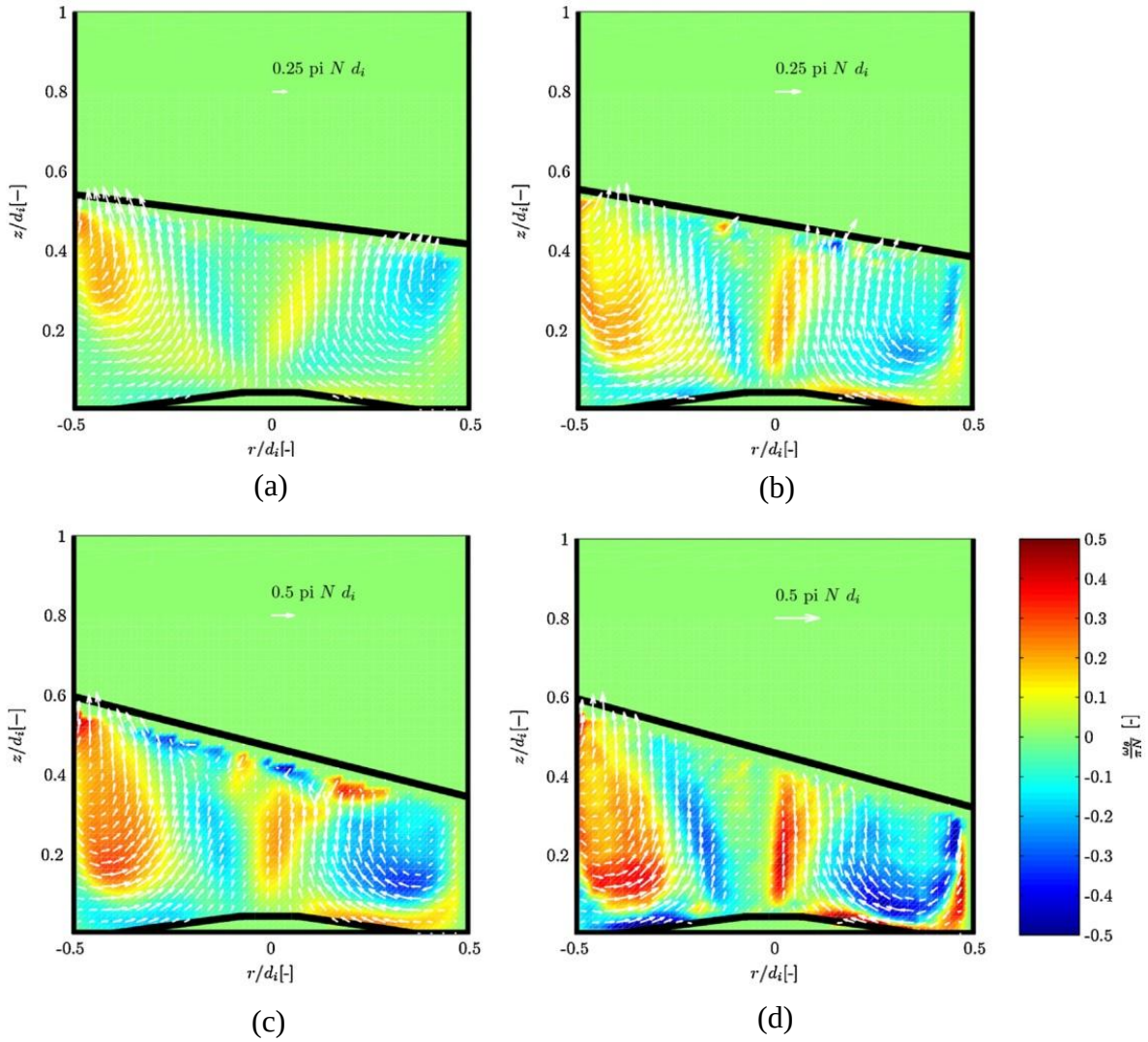

Figure 6.3: Phase-resolved non-dimensional velocity fields and contours of the tangential component of vorticity, ω_θ, for conical A bottom geometry at (a–d) Fr = 0.10, 0.14, 0.17, 0.18 (N = 85, 100, 110, 115 RPM).

A similar vortical cell expansion was observed for the conical bottom bioreactors investigated, however some differences with the flat bottom geometry can be noted from Figure 6.3 and 6.4. The shaking speed at which the vortices extend to the bottom decreases as the inclination of the conical bottom is increased. It is clear from Figure 6.4 a–d that the vortices reach the base of the bioreactor at a shaking speed N = 100 RPM for the most inclined conical bottom studied in this work, while the same phenomenon occurs at N = 110 RPM and 115 RPM for the conical A and flat bottom designs, respectively. Despite the fact that the fully extended vortex configuration occurs at lower speeds when conical bottom geometries are used, Figure 6.4 a–d suggest that the vortical structures

are still present at speeds higher than that associated to full vortex extension and the critical speed of the aforementioned mean flow transition is not affected by the bottom geometry. This could be due to the conical design influencing the shape of the vortical cells, pushing them closer to the vessel walls and away from each other reducing their interaction at the centre of the bioreactor.

Vorticity intensity increases as the shaking speed is increased for all bottom configurations investigated, as seen in Figure 6.2–6.4.

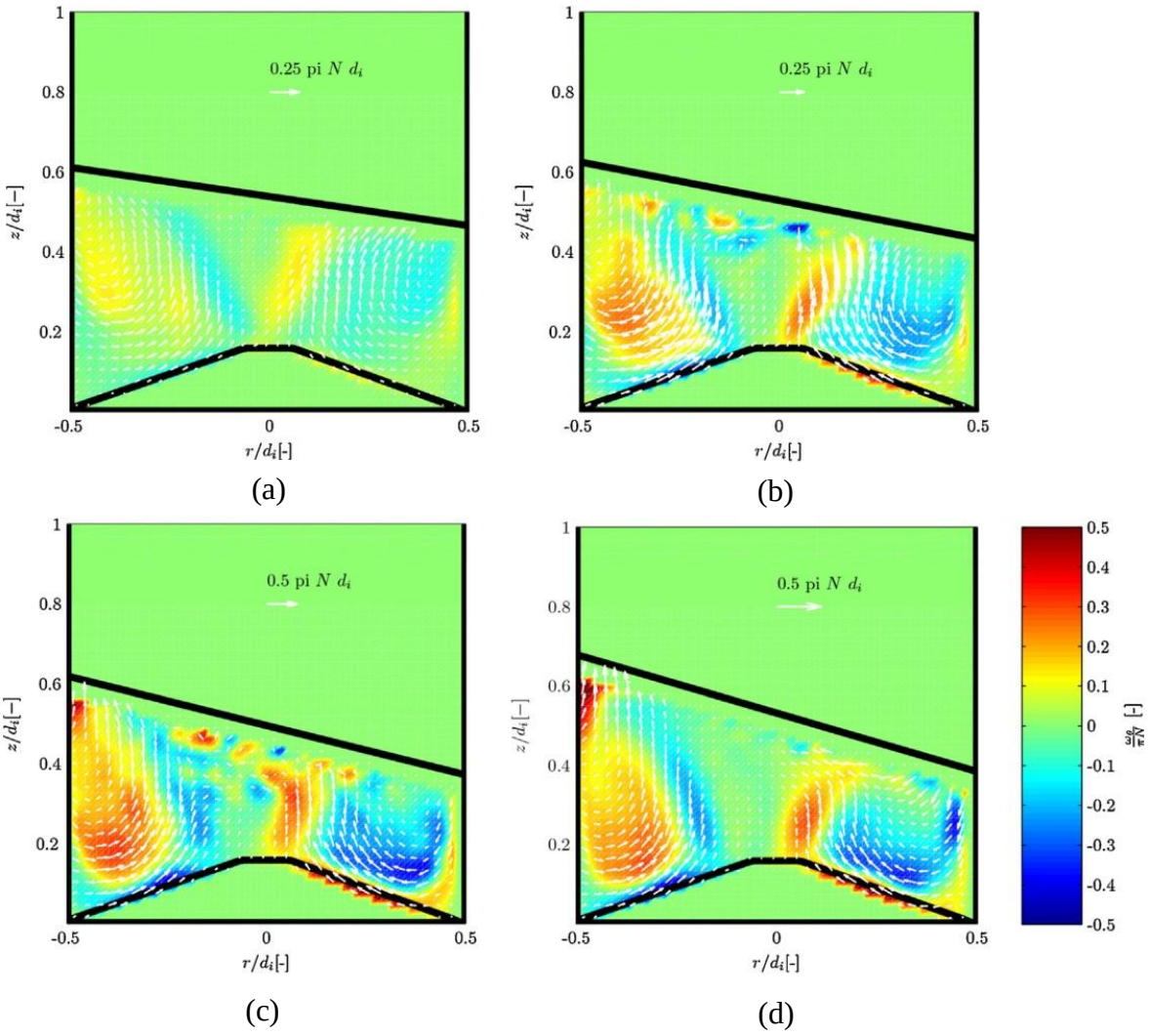

Figure 6.4: Phase-resolved non-dimensional velocity fields and contours of the tangential component of vorticity, ω_θ,, for conical B bottom geometry at (a–d) Fr = 0.10, 0.14, 0.17, 0.18 (N = 85, 100, 110, 115 RPM).

The space-averaged non-dimensional vorticity, ω_θ^*, is defined in Equation 6.3 and its variation with *Fr* is provided in Figure 6.5 a. The spaced-average was carried out inside the area delimited by a non-dimensional vorticity threshold of $\omega_\theta > 0.1\ \pi N$, which is shown for reference in Figure 6.5 b (conical A configuration, $N = 80$ RPM, $Fr = 0.09$).

$$\omega_\theta^* = \frac{\int_{A_\omega = 0.1\pi N} |\omega_\theta|\, dA_\omega}{A_\omega} \tag{6.3}$$

As expected, the space-averaged non-dimensional vorticity, ω_θ^*, increases with *Fr* for flat, conical A and B bottoms (Figure 6.5 a). At shaking speeds corresponding to values of *Fr* below 0.12, similar values of ω_θ^* were obtained for all geometries investigated. At these conditions the toroidal vortices are present only in proximity of the free surface and vessel walls, as shown in Figure 6.2 a, 6.3 a and 6.4 a, respectively. The main flow does not extend to the bioreactor bottom hence no effect of the conical bottom was observed. However for $Fr > 0.12$ the rate of vorticity variation with *Fr* is more pronounced with increasing inclination of the conical bottom. Power curves fitted to the data points suggest a steeper increase of the non-dimensional space-averaged vorticity for the conical B geometry. This behavior is in agreement with the description of the phase-resolved flow provided above, and indicates that the vorticity of the two cells is affected by the bottom geometry only for speed sufficiently large to determine full expansion to the bioreactor base. The greater space-averaged vorticity would benefit solid suspension as the solid lifting force, $F_{Saffman} = (\pi/4) d_p^3\ (\rho_l/2)\ C_s\ ((u - v_p) \times \omega)$ (Derksen, 2003), is proportional to the slip velocity $(u - v_p)$ and flow vorticity (ω) with d_p and v_p being the solid diameter and velocity, ρ_l and u the viscosity and velocity of the liquid phase and C_s the lift coefficient.

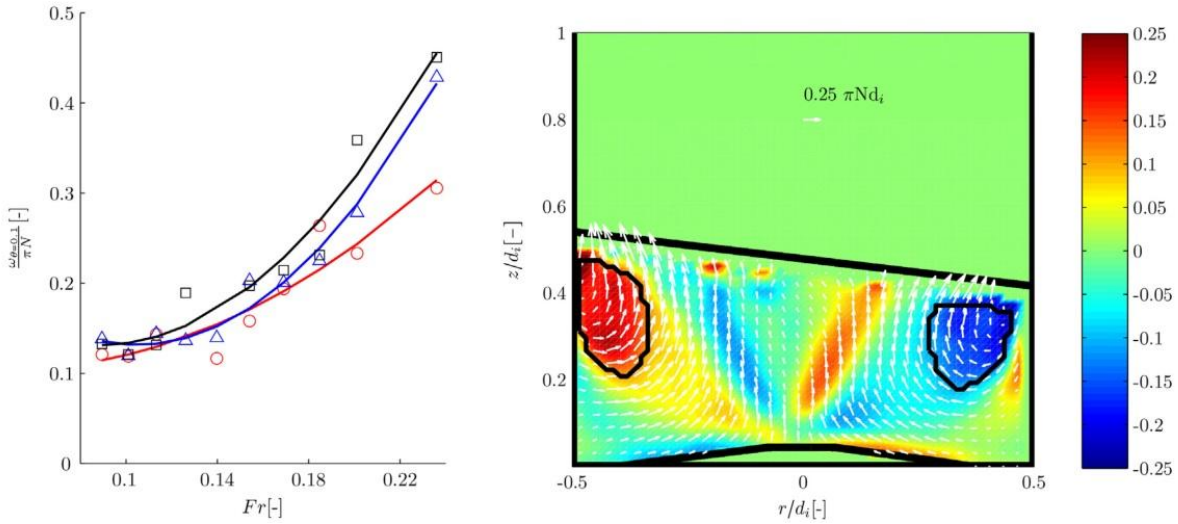

(a) (b)

Figure 6.5: (a) Variation of the spaced-averaged non-dimensional vorticity with increasing *Fr*: flat bottom (○), Conical A (Δ), and Conical B (□); (b) Visualization of the area ω_θ = 0.1 πN used to determine the average vorticity.

6.3.2 Effects of bottom design on shear rates

The effect of shear on cells and product expression has been a topic of discussion since mammalian cells became one of the major expression host for the production of antibodies and other therapeutics, and an agreement has yet to be reached on whether fluid stresses have a significant impact (Cherry and Hulle, 1992; Keane et al., 2003; Ludwig et al., 1992; Nienow et al., 2013). It is clear, though, that a more rigorous quantification of fluid shear is needed in order, for example, to improve understanding of its effect on stem cells. Maximum shear and strain rate components have therefore been quantified in this work. The strain rate tensor, S_{ij}, for the 2D flow studied is defined in the following equation (Equation 6.4):

$$S_{ij} = \begin{pmatrix} \frac{\partial u_i}{\partial x_i} & \frac{1}{2}\left(\frac{\partial u_i}{\partial x_i} + \frac{\partial u_j}{\partial x_j}\right) \\ \frac{1}{2}\left(\frac{\partial u_i}{\partial x_i} + \frac{\partial u_j}{\partial x_j}\right) & \frac{\partial u_j}{\partial x_j} \end{pmatrix} \tag{6.4}$$

where indices *i* and *j* indicate the radial and axial directions, respectively. The strain rate tensor is a measure of local rate of stretching, compression and shear. When a local reference

system aligned with the principal axes of S_{ij} is considered, the highest rate of stretching and compression can be determined.

These are found from the principal components (eigenvalues) S_1 and S_2 of the strain rate tensor in Equation 6.4. Positive values of S_1 and S_2 indicate stretching whilst negative values relate to compression (Bouremel et al., 2009; Davidson, 2004). In this work only two velocity components were measured, therefore the S_3 component of the strain rate tensor in the k direction orthogonal to the plane of measurement (i.e. azimuthal direction) was estimated using the continuity equation (Equation 6.5):

$$S_3 = -S_1 - S_2 \tag{6.5}$$

The principal components of the strain rate tensor, S_1 and S_2 , for the conical B geometry at Fr = 0.14 (N = 100 RPM) are shown in Figure 6.6 a and b, respectively. It should be noted that the principal component S_1 is negative across the entire field of view, and therefore it provides an estimate of the compression rates experienced by the cells. The direction of compression is not given in Figure 6.6 a, but it is locally aligned with the direction of the first eigenvector of the local strain rate tensor. From the contour plot the highest compression rate is found at the margins of the counter-rotating vortices. The normal stress S_2, which is always positive and is associated to local stretching rates, reaches its maximum in the lower section of the toroidal vortices, at $|r/d_i|$ = 0.1–0.5 and z/d_i = 0.1–0.2, in proximity of the tips of the conical bottom upper surface.

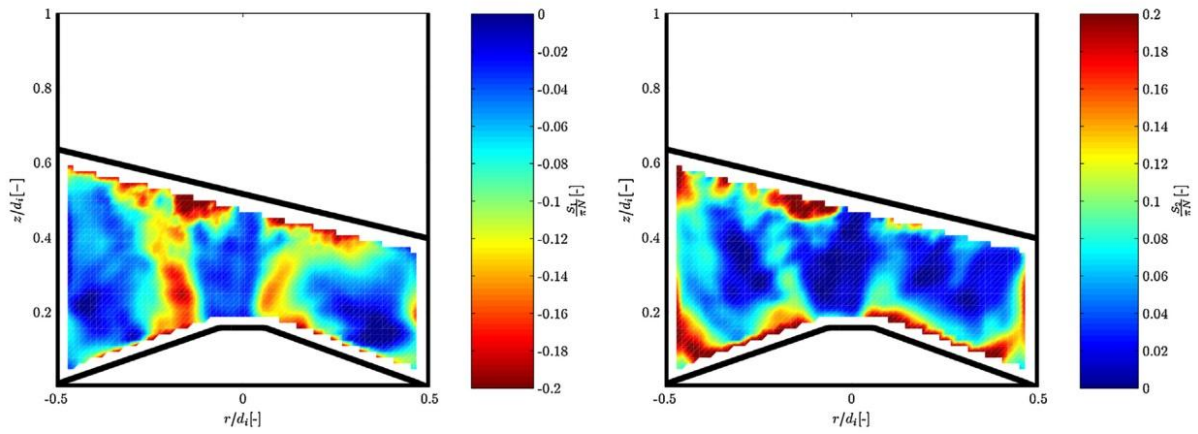

(a) (b)

Figure 6.6: Principal component of the strain rate tensor at ϕ = 0° for conical B geometry (Fr = 0.14, N = 100 RPM). (a) compression strain rate S_1, (b) stretching strain rate S_2.

The maximum shear rate, τ_{max}, experienced at a specific location, can be found from the principal components of the strain rate tensor according to the following equation (Equation 6.6):

$$\tau_i = \frac{(S_i - S_j)_{max}}{2} \tag{6.6}$$

where indices i and j are selected based on the maximum difference between any two principal components S_1, S_2, S_3. The contour plots of the phase-resolved maximum shear rates on the vertical plane (ϕ = 0°) at Fr = 0.14 (N = 100 RPM) for flat, conical A and B geometries are shown in Figure 6.7 a–c, respectively.

This Fr number corresponds to in-phase flow condition for all the geometries investigated (according to the definition given by Weheliye et al., 2013), but the toroidal vortices extend to the bottom of the vessel only for the conical B configuration (as determined from Figure 6.2 b, 6.3 b and 6.4 b).

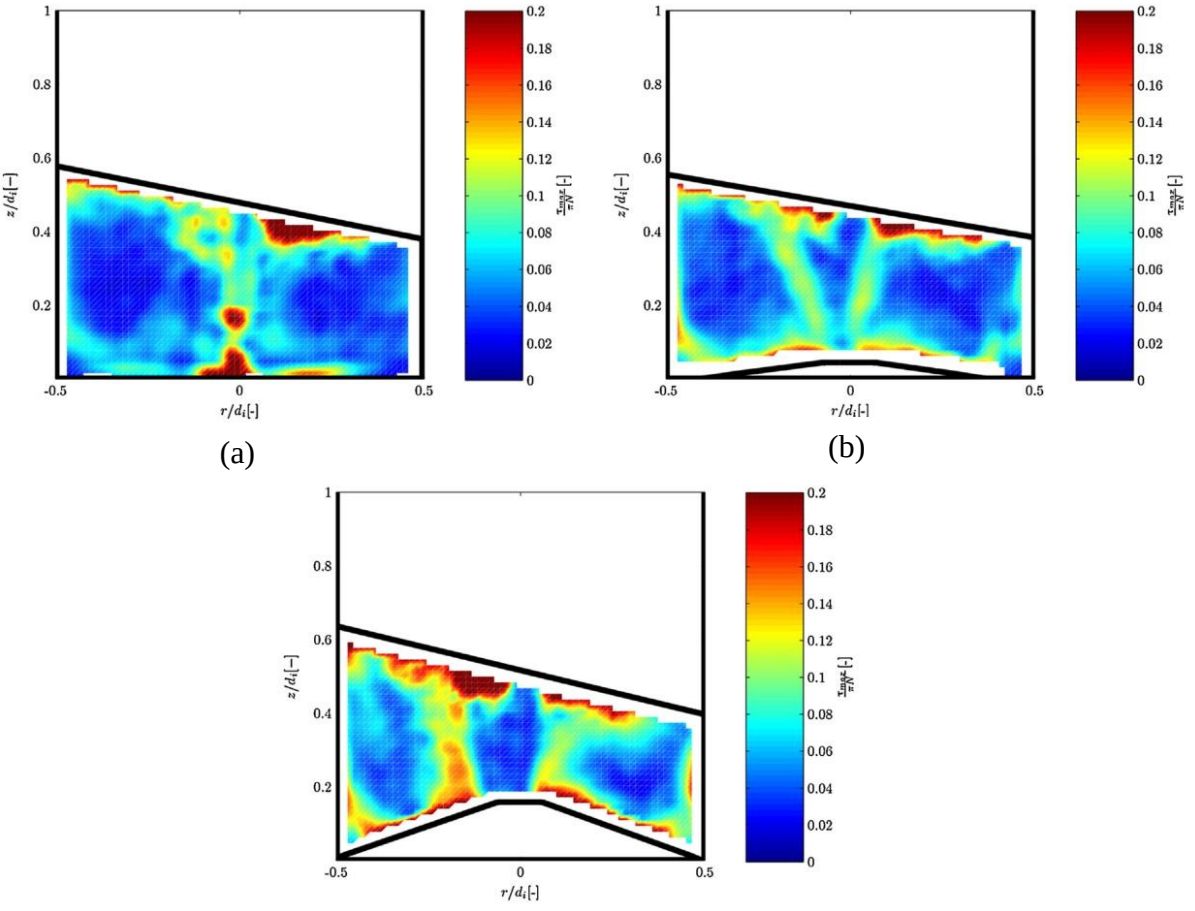

Figure 6.7: Contour maps of the maximum shear strain rate of the flow at ϕ = 0° for (a) flat, (b) conical A, (c) conical B geometries at Fr = 0.14 (N = 100 RPM).

Values as high as τ_{max} = 0.13 πN can be observed in Figure 6.7 a at the periphery of the toroidal vortical cells (shown in Figure 6.2 b). The maximum shear rate of Figure 6.7 a, τ_{max} = 0.2 πN occurs at r/d_i = 0.5 in correspondence to the cylinder axis. This was probably due to inaccuracies in the PIV measurements as tracer particle agglomerates were visually observed at such location. The lowest τ_{max} were found at the core of the cells ($|r/d_i|$ = 0.2, z/d_i = 0.2–0.3), where quasi-solid body rotation occurs. Similarly, the maximum shear rates for the conical A and B bottoms are characterized by low values at the core of the vortical cells and higher shear rates at the periphery (Figure 6.6 b–c). The maximum intensity

of the shear rate occurs at the interfaces between the vortices and the fluid above the upper conical surface. Whilst Figure 6.7 a shows two distinct low shear regions in correspondence to the vortical cell cores, a third region of low τ_{max} can be observed for conical geometries A and B, above the truncated cone tip. When observing the high shear regions rising at the margins of the counter clockwise and clockwise vortices, it appears that all of them are locally orthogonal to bioreactor base, i.e. vertical for the flat bottom (in Figure 6.7 a) and outwards

inclined in Figure 6.7 b–c for the conical bottom geometries. The maximum shear rate obtained in Figure 6.7 corresponds to dimensional shear stresses of 0.001 N m^{-2}. As a reference stem cell proliferation is affected by shear stress greater than 0.1 N m^{-2} (see Toh and Voldman, 2011) while mammalian cells damage occurs at value higher than 0.15 N m^{-2} (Elias et al., 1995), which are well above those reported in this work.

The variation of the average maximum shear stress, τ^*_{max}, with *Fr* is shown in Figure 6.8 for the three bottom configurations investigated. The asterisk denotes the space-average of the absolute value of τ_{max} over the vertical plane of measurement. Outlier values of τ^*_{max} were not included in the space-average as caused by erroneous velocity vectors close to

the free surface. For all cases τ^*_{max} increases with *Fr*. Similarly to Figure 6.7 a–c, the conical B geometry presents higher values of τ^*_{max} for most *Fr*, as the toroidal vortices are more compressed towards the sides of the vessel, resulting in a more intense deformation rate. The maximum shear stress, τ^*_{max}, increases up to *Fr* = 0.17, then a sharp decrease can be observed, after which τ^*_{max} increases again with *Fr*. This can be explained by the onset of the out-of-phase flow transition, where the tangential velocity component in the direction orthogonal to the plane of measurement is the most significant.

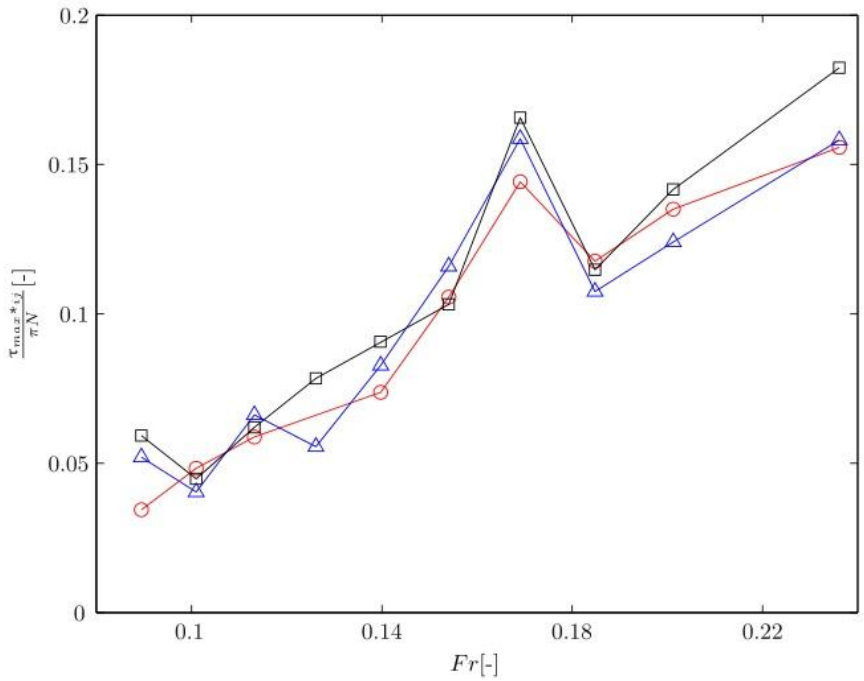

Figure 6.8: Variation of the spaced-averaged non-dimensional maximum shear rate, τ^*_{max}, with increasing *Fr*: flat bottom (○), Conical A (Δ), and Conical B (□).

6.3.3 Effects of bottom design on local flow direction

A better understanding of the bioreactor flow can be gained from Figure 6.9 a where vertical profiles of the phase-averaged radial velocity component are plotted for a phase angle ϕ = 270°. In this figure the vertical profiles associated to a flat and conical B bottom geometries are compared at two radial coordinates, *r/di* = 0 and 0.25, indicated in Figure 6.9 c, for two shaking speeds, *N* = 80 and 100 RPM. In Figure 6.9 a the non-dimensional velocity is on the abscissa, with magnitude increasing from right to left, while the distance from the vessel bottom is plotted on the ordinate axis. As expected the intensity of the radial velocity increases when moving closer to the free surface for the profiles plotted. It is evident that the two profiles for the flat and conical B bottom differ at a shaking speed *N* = 100 RPM, because at this regime the flow has nearly developed for both geometries all the way to the bottom of the reactor, and it is therefore affected by the bottom geometry. This does not occur when the lowest speed is considered as for both configurations the vortical flow has developed over a small region below the free surface, and therefore the differences in bottom geometries are less relevant. It can be observed that the curves seem to be shifted vertically between flat and conical B bottoms, this being more apparent at the higher shaking speed considered. It should be noted that both sets of measurements were obtained for the same filling volume and therefore the maximum height of the conical bottom was higher than the flat one. This

implies that points at the same height are further away from the free surface, which is the flow driving mechanism, for the conical bottom than for the flat one.

The same data are presented in Figure 6.9 b, where a normalized axial coordinate with origin on the free surface $(z-h)/d_i$ is considered. The new axial coordinate system shown in Figure 6.9 c is more effective at capturing the similarity between the flow of the two geometries. From Figure 6.9 b it is evident that according to this reference system the vertical profiles of the two configurations show an excellent match, particularly in proximity of the free surface where the local flow is less affected by the difference in bottom geometry.

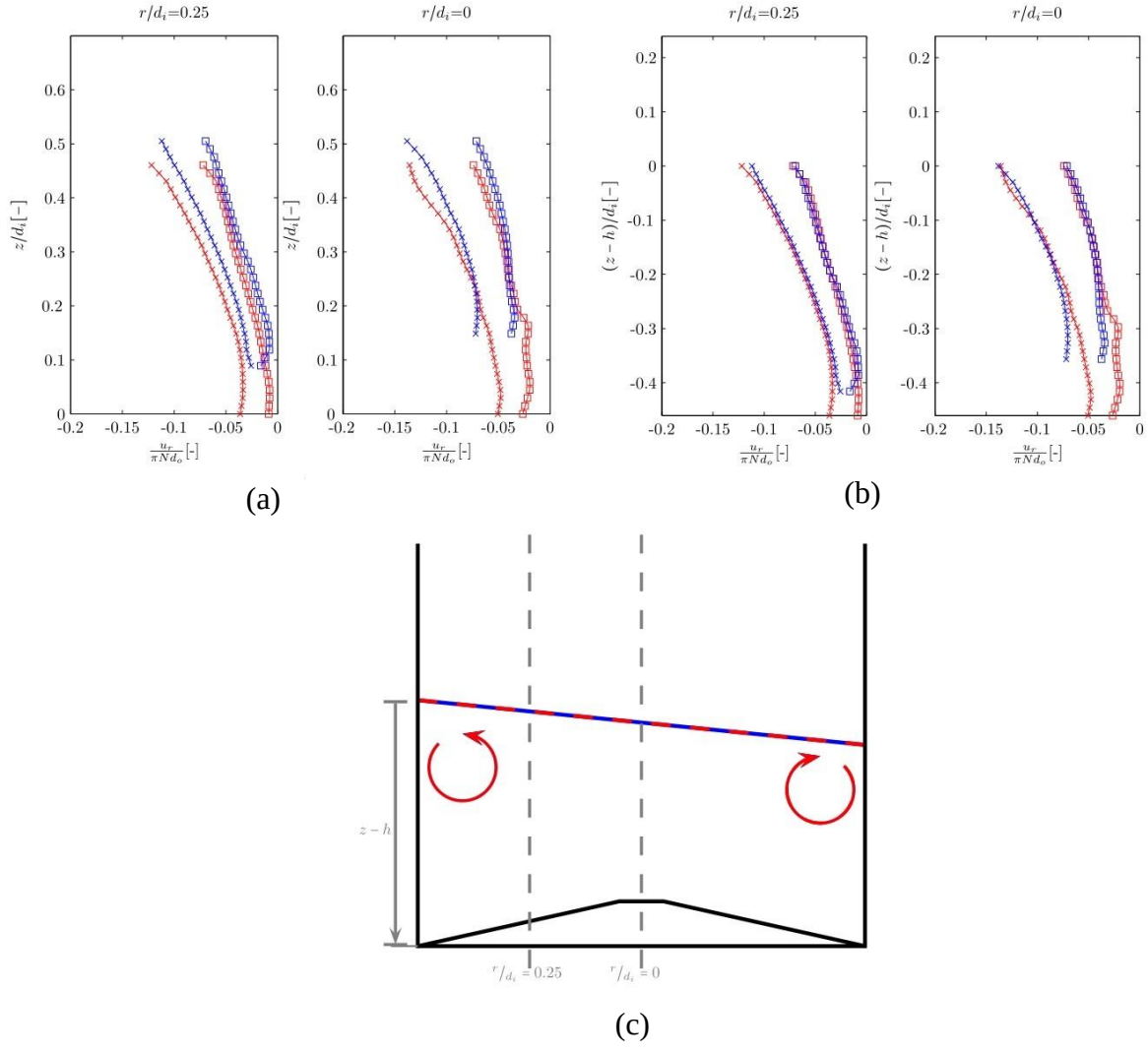

Figure 6.9: (a) Comparison of the vertical profiles of the radial velocity component for a flat bottom (red) and Conical B bottom (blue) at two shaker speeds N = 80 RPM (□) and N = 100 RPM (×); (b) profiles of the radial velocity component with a coordinate system $(z-h)/d_i$ for a flat bottom (red) and Conical B bottom (blue) at two shaker speeds N = 80 RPM (□) and N = 100 RPM (×); (c) diagram of the location of the radial profiles at coordinates r/d_i = 0 and 0.25.

The mean flow at a phase angle ϕ = 270° consists of fluid motion from one side to the other of the bioreactor. Figure 6.10 shows the velocity field for Fr = 0.14 (N = 100 RPM) for flat (white vector field) and conical B bottom geometries (black vector field). As can be seen in the inset of Figure 6.10, the velocity fields present differences in magnitude and direction between the two geometries. The contour describes the angle difference α_{angle} between the velocity fields of the flat bottom and conical B geometry, with a clockwise direction change in red and counter clockwise direction change in blue. The regions where the flow is most affected by the different bottom geometry are close to the conical bottom, with the 'upstream' side at the right of the cone experiencing a more significant change in velocity direction in comparison to the 'downstream' on the left. The condition Fr = 0.14 presents toroidal vortices expanded to the bioreactor bottom, as described in Figure 6.4 c, hence a large region of the flow is affected by the conical B geometry.

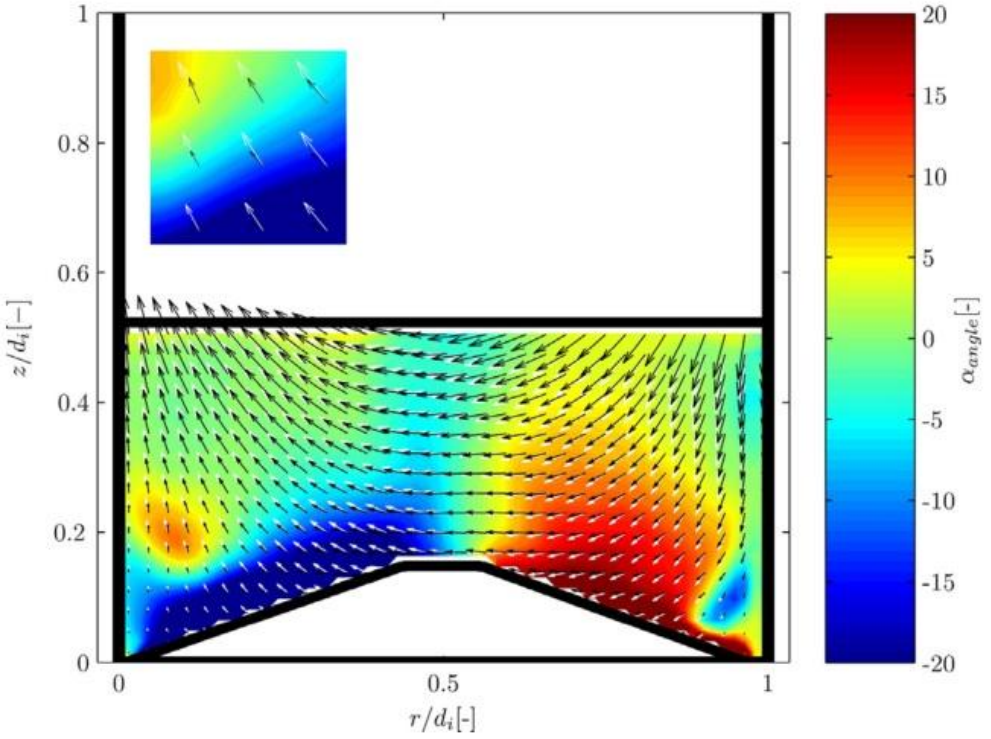

Figure 6.10: Velocity field for Fr = 0.14 (N = 100 RPM) for flat bottom (white vector field) and conical B (black vector field); contour of the angle difference, α_{angle}, between velocity fields. Inset: detail of the velocity field.

The velocity ratio U/U_c was estimated to further assess the effect of the bottom geometry on the velocity field, where U and U_c are the velocity magnitude for the flat and conical B bottom geometries, respectively. A relation was sought between the change in α_{angle} and the change in

velocity magnitude, and the results of this analysis are shown in Figure 6.11 for N = 100 RPM (Fr = 0.14). The U/U_c data shown in Figure 6.11 are limited to those points where the $|\alpha_{angle}| > 10°$. The distribution of the data points on the positive α_{angle} axis, upstream side, is characterized by a narrower spread of U/U_c in comparison to the data points associated to negative α_{angle}, downstream side (Figure 6.11). This implies that the upstream flow is mainly deflected, as indicated by the larger region with angle variation (cf. Figure 6.10), but its velocity magnitude is less affected (cf. Figure 6.11). The opposite occurs downstream of the conical bottom where the region associated to a significant deflection is smaller, but its velocity distribution is broader and U/U_c is larger.

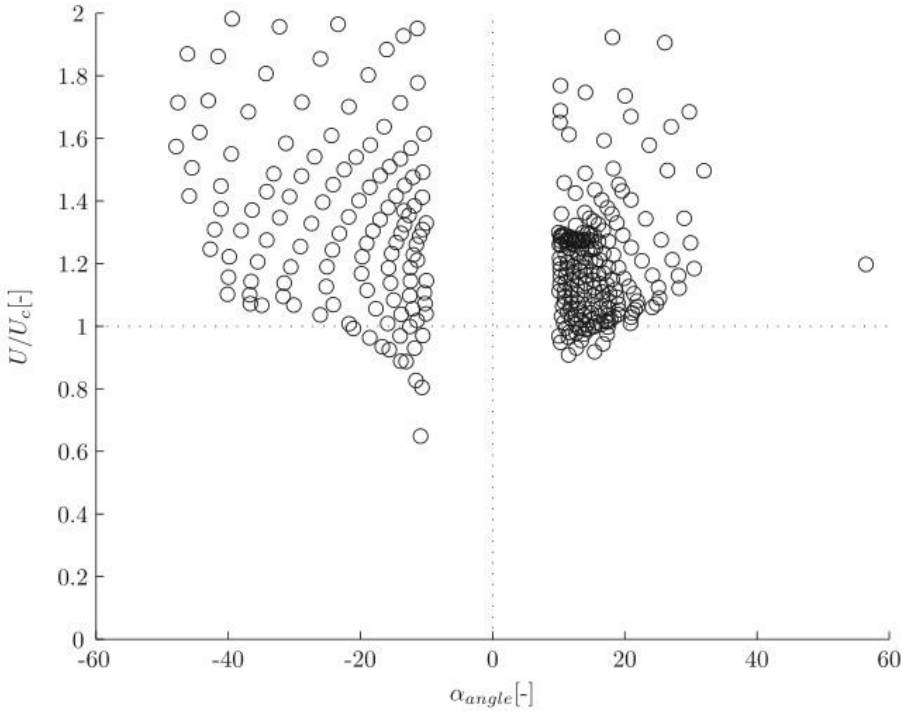

Figure 6.11: Scatter plot of the velocity ratio, U/U_c , and angle difference, α_{angle}, for Fr = 0.14 (N=100 RPM).

6.3.4 Effects of bottom design on energy content

Similarly to Rodriguez et al. (2013), in this work the velocity field is described using the Reynold's decomposition, $u(r, z, t) = \langle u(r, z, \phi) \rangle + u'_i(r, z, t), t)$, with $\langle u(r, z, \phi) \rangle$ being related to flow periodic variations and $u'_i(r, z, t)$ taking into account random fluctuations. The spaced-averaged non-dimensional kinetic energy of the random velocity fluctuations, k'^*_{rz} , was evaluated for the bioreactors under investigation according to the 2D approximation of the following equation (Equation 6.7):

$$k'^{*}_{rz} = \frac{1}{A}\int_{A} \frac{3}{4}(u_r'^2 + u_z'^2)dA \tag{6.7}$$

where $u_r'^2$ and $u_z'^2$ are phase-resolved terms of the random velocity fluctuations, and A is the area of the measurement field. The variation of k'^{*}_{rz} with Fr for all geometries under investigation is shown in Figure 6.12 at a phase angle ϕ = 0°. Low values of kinetic energy k'^{*}_{rz} were measured for Fr = 0.9–0.14 (N = 80–100 RPM), followed by a sharp increase peaking at Fr = 0.17. Above Fr = 0.17 k'^{*}_{rz} drops to low values. This can be explained by considering that at Fr = 0.17 the flow transition to a precessional vortex with a vertical axis occurs (see Weheliye et al., 2013). Above the critical flow-transition speed the main velocity component is aligned with the tangential direction which cannot be directly estimated from the vertical plane measurements presented in this work. The results presented in Figure 6.12 confirm that flow transition occurs at the same Fr numbers for all geometries considered. It can also be noted that the measured values of k'^{*}_{rz} for all geometries were comparable up to Fr = 0.14, whilst for Fr > 0.17 lower values of kinetic energy were found for the conical B geometry when compared to the flat bottom (approximately 35% smaller). This suggests that the phase-resolved flow at conditions close to N_{crit} presents more stable vortical structures, with fewer velocity fluctuations for the conical configuration.

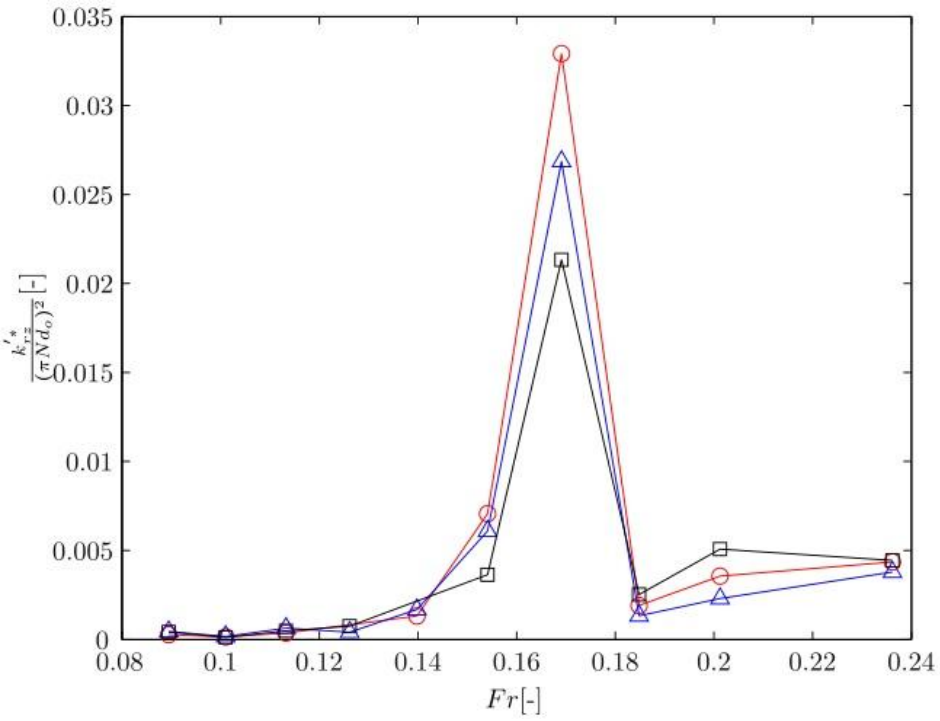

Figure 6.12: Variation of the spaced-averaged non dimensional kinetic energy of the random velocity fluctuations, k'^{*}_{rz} with increasing Fr: flat bottom (○), Conical A (Δ), and Conical B (□).

6.4 Conclusions

In the present study the effect of the implementation of a conical bottom design in an orbital shaken bioreactor has been extensively discussed. Two truncated conical bottoms of h_{cone} = 5 mm and 15 mm were used with an OSR and the resulting fluid dynamics investigated in detail and compared with those obtained for a flat bottom configuration. The impact of the bottom geometry on the general flow characteristics at a phase angle $\phi = 0°$ was investigated first. It was found that the flow in cylindrical bioreactors with conical bottoms is characterised by toroidal vortices expanding towards the bottom with increasing *Fr*, as is the case for a standard flat configuration, while for the cone with the highest inclination examined (conical B) the vortices reached the bottom at a lower *Fr*. Despite this difference the Froude number, Fr_{cr}, associated to the flow transition did not vary from the values reported for a flat bottom bioreactor. The space-averaged vorticity increased for all bottom geometries with *Fr*, however ω_θ* increased at a higher rate in the conical B geometry when $Fr > 0.12$. This was explained by considering that for this configuration the interaction between the vortical cells and the bioreactor bottom starts to occur at lower speeds. The proposed designs were also evaluated in terms of shear rates. It was found that the most intense deformations occurred at the periphery of the toroidal vortices, with low shear rate values present at the centre of the vortical cells. For a given *Fr*, the vortical cells are closer to the vessel base with the conical bottom resulting in higher maximum shear rates, τ_{max}, when the conical B configuration was analysed. The use of the conical geometry resulted in an area of low shear rates at $r/d_i = 0.5$ as the inclined surfaces of the conical bottoms modified the shape of the vortical cells, resulting in the regions of largest shear deformation being orthogonal to the cone external walls. The space-averaged maximum shear rate variation indicated that the mean shear rate within the vessel was similar for all geometries at the same *Fr*, although slightly higher values were found for the highest cone. When the designs were evaluated at a different measurement angle, $\phi = 270°$, which is characterized by a strong radial flow from one side to the other one of the bioreactor, it was observed that the region with the greatest change in velocity direction were in proximity of the inclined surfaces of the conical bottoms. The flow 'upstream' of the conical bottom experiences larger deflection with similar velocity magnitude between flat and conical B geometries, whilst the region 'downstream' of the conical bottom resulted in a greater range of velocity ratios. Finally, the variation of the kinetic energy content of the random (i.e. cycle-to-cycle) velocity fluctuations shows that the energy content increases with *Fr* for all designs and the *Fr* associated with flow transition does not change.

In this work a rigorous methodology was established, that allows the fluid dynamics characterization of alternative bioreactor designs. The use of a conical geometry at the bottom of a cylindrical OSR allows the achievement of similar flow dynamics conditions at a lower *N* in

comparison to a flat bottom bioreactor. This has important implications for shear-sensitive cultures requiring solids suspension, as the new bioreactor design can be operated at low shaking speeds, resulting in low shear rates, without compromising the quality of the suspension. It is also noteworthy that the proposed designs could be beneficial for microcarriers suspension, as higher lifting forces due to increased vorticity levels should occur in conical bottom reactors, thus avoiding the accumulation of solids at the centre of the bioreactor bottom and probably requiring a lower just suspended speed in comparison to flat bottom configurations.

6.5 References

Aloi, L.E., Cherry, R.S., 1996. Cellular response to agitation characterized by energy dissipation at the impeller tip. Chem. Eng. Sci. 51, 1523–1529.

Bouremel, Y., Yianneskis, M., Ducci, A., 2009. On the utilisation of vorticity and strain dynamics for improved analysis of stirred processes. Chem. Eng. Res. Des. 87, 377–385.

Büchs, J., Lotter, S., Milbradt, C., 2001. Out-of-phase operating conditions, a hitherto unknown phenomenon in shaking bioreactors. Biochem. Eng. J. 7, 135–141.

Cherry, R.S., Hulle, C.T., 1992. Cell-death in the thin-films of bursting bubbles. Biotechnol. Prog. 8, 11–18.

Cherry, R.S., Papoutsakis, E.T., 1988. Physical-mechanisms of cell-damage in microcarrier cell-culture bioreactors. Biotechnol. Bioeng. 32, 1001–1014.

Davidson, P.A., 2004. Turbulence an Introduction for Scientist and Engineers. Oxford University Press, Oxford.

Derksen, J.J., 2003. Numerical simulation of solids suspension in a stirred tank. AIChE J. 49, 2700–2714.

Ducci, A., Weheliye, W.H., 2014. Orbitally shaken bioreactors-viscosity effects on flow characteristics. AIChE J. 60, 3951–3968.

Elias, C.B., Desai, R.B., Patole, M.S., Joshi, J.B., Mashelkar, R.A., 1995. Turbulent shear-stress effect on mammalian-cell culture and measurement using laser-doppler anemometer. Chem. Eng. Sci. 50, 2431–2440.

Funke, M., Diederichs, S., Kensy, F., Muller, C., Buchs, J., 2009. The baffled microtiter plate: increased oxygen transfer and improved online monitoring in small scale fermentations. Biotechnol. Bioeng. 103, 1118–1128.

Gardner, J., Tatterson, G., 1992. Characterization of mixing in shaker table containers. Biotechnol. Bioeng. 39, 794–797.

Ismadi, M.Z., Gupta, P., Fouras, A., Verma, P., Jadhav, S., Bellare, J., Hourigan, K., 2014. Flow characterization of a spinner flask for induced pluripotent stem cell culture application. PLoS ONE 9.

Keane, J.T., Ryan, D., Gray, P.P., 2003. Effect of shear stress on expression of a recombinant protein by Chinese hamster ovary cells. Biotechnol. Bioeng. 81, 211–220.

Li, D., Zhou, J.X., Chowdhury, F., Cheng, J.J., Wang, N., Wang, F., 2011. Role of mechanical factors in fate decisions of stem cells. Regen. Med. 6, 229–240.

Ludwig, A., Tomeczkowski, J., Kretzmer, G., 1992. Influence of shear-stress on adherent mammalian-cells during division. Biotechnol. Lett. 14, 881–884.

Monteil, D.T., Tontodonati, G., Ghimire, S., Baldi, L., Hacker, D.L., Burki, C.A., Wurm, F.M., 2013. Disposable 600-mL orbitally shaken bioreactor for mammalian cell cultivation in suspension. Biochem. Eng. J. 76, 6–12.

Nienow, A.W., Rafiq, Q.A., Coopman, K., Hewitt, C.J., 2014. A potentially scalable method for the harvesting of hMSCs from microcarriers. Biochem. Eng. J. 85, 79–88.

Nienow, A.W., Scott, W.H., Hewitt, C.J., Thomas, C.R., Lewise, G., Amanullah, A., Kiss, R., Meieer, S.J., 2013. Scale-down studies for assessing the different stress parameters on growth and product quality during animal cell culture. Chem. Eng. Res. Des. 91, 2265–2274.

Olmos, E., Loubiere, I., Martin, C., Delaplace, G., Marc, A., 2015. Critical agitation for microcarrier suspension in orbital shaken bioreactors: experimental study and dimensional analysis. Chem. Eng. Sci. 122, 545–554.

Pieralisi, I., Rodriguez, G., Micheletti, M., Paglianti, A., Ducci, A., 2015. Microcarriers' suspension and flow dynamics in orbitally shaken bioreactors. Chem. Eng. Res. Des., http://dx.doi.org/10.1016/j.cherd.2015.11.020.

Rodriguez, G., Anderlei, T., Micheletti, M., Yianneskis, M., Ducci, A., 2014. On the measurement and scaling of mixing time in orbitally shaken bioreactors. Biochem. Eng. J. 82, 10–21.

Rodriguez, G., Weheliye, W., Anderlei, T., Micheletti, M., Yianneskis, M., Ducci, A., 2013. Mixing time and kinetic energy measurements in a shaken cylindrical bioreactor. Chem. Eng. Res. Des. 91, 2084–2097.

Sargent, C.Y., Berguig, G.Y., Kinney, M.A., Hiatt, L.A., Carpenedo, R.L., Berson, R.E., McDevitt, T.C., 2010. Hydrodynamic modulation of embryonic stem cell differentiation by rotary orbital suspension culture. Biotechnol. Bioeng. 105, 611–626.

Stolberg, S., McCloskey, K.E., 2009. Can shear stress direct stem cell fate? Biotechnol. Prog. 25, 10–19.

Tissot, S., Farhat, M., Hacker, D.L., Anderlei, T., Kuhner, M., Comninellis, C., Wurm, F., 2010. Determination of a scale-up factor from mixing time studies in orbitally shaken bioreactors. Biochem. Eng. J. 52, 181–186.

Toh, Y.-C., Voldman, J., 2011. Fluid shear stress primes mouse embryonic stem cells for differentiation in a self-renewing environment via heparan sulfate proteoglycans transduction. FASEB J. 25, 1208–1217.

Walsh, G., 2014. Biopharmaceutical benchmarks 2014. Nat. Biotechnol. 32, 992–1000.

Weheliye, W., Yianneskis, M., Ducci, A., 2013. On the fluid dynamics of shaken bioreactors—flow characterisation and transition. AIChE J. 59, 334–344.

Zhang, J.Y., 2010. Mammalian cell culture for biopharmaceutical production. In: Manual of Industrial Microbiology and Biotechnology, third ed. ASM Press, Washington, DC., pp. 157–178.

Zhang, X., Stettler, M., Reif, O., Kocourek, A., DeJesus, M., Hacker, D.L., Wurm, F.M., 2008. Shaken helical track bioreactors: providing oxygen to high-density cultures of mammalian cells at volumes up to 1000 L by surface aeration with air. New Biotechnol. 25, 68–75.

7 Conclusions

The major objective of the research presented in this thesis was to provide accurate data on the hydrodynamics developing within some specific mixing system configurations.
In each case analyzed, both fundamental and engineering aspects of the flow were addressed, with the final aim of enhancing the knowledge of the process, and of improving its performances.
Mixing in vessels was considered, and in particular a mechanically stirred vessel of standard geometry, an unbaffled mechanically stirred vessel of unconventional geometry, and an orbitally shaken bioreactor were studied.
Although these equipments are widely employed for several different applications in the chemical and pharmaceutical industry, uncertainties and approximations still exist on their design and/or operating conditions. This is true especially for the case of unbaffled stirred vessels and shaken bioreactors, where the flow develops not axisymmetrically and thus it is strongly influenced by even small changes in the system geometry.
For standard geometry stirred vessels efficient scale-up criteria and design rules have been already developed, since their behaviour is more regular and they have been subjected to investigations for many decades. Notwithstanding this, a complete characterization of the flow and mixing dynamics generated within these systems under some specific operating conditions is not available in the literature.
In the present study, experimental investigations based on the use of optical techniques like Laser Doppler Anemometry and Particle Image Velocimetry were carried out within different types of reactors, and novel and reliable data on the mean and turbulent characteristics of the flow were collected for each configuration analyzed. Subsequent data analysis allowed to identify and characterize the principal phenomena occurring in the flow and their influence on the mixing processes. In this way, relevant and brand new scientific data were collected, but also suggestions for the correct design and operation of the reactors were provided.

The first case study regarded the flow dynamics developing within a four-bladed PBT-stirred reactor working under laminar flow regime (Section 3). Through a dual channel LDA system, ensemble and angle-resolved velocity measurements were obtained in a region close to the impeller, and a three-dimensional reconstruction of the flow was achieved. The analysis of the mean flow over vertical and azimuthal planes revealed that the low Reynolds number influences the axial pumping action of the turbine and the development of macro flow structures along the impeller blades. Particularly, in these conditions the impeller discharge stream does not have enough kinetic

energy to reach the bottom of the tank, but rises gradually for increasing values of *z/D*, until it becomes totally radial at *z/D* = 0.65. In addition, two trailing vortices of radial vorticity were observed at the tips of each blade, while the available literature on PBT stirred tanks working under turbulent flow regime reports the occurrence of just one tangential vortex developing along each impeller blade.

Observing the flow and vorticity levels on azimuthal planes, it was found that apart from the direction of circulation, the two vortices present very similar characteristics, assuming absolute intensities comparable everywhere, and generating in both cases wakes with an inclination of about 30° from the horizontal direction. The vortices maintain their features almost unaffected until the radial coordinate does not exceed the blades radius (*D*/2). At this stage, they start losing strength and they disappear at around *r/D* =0.6.

It was found that the vortex radius, R_{tv}, assumes a value around 30 % of the height of the blade at any r/D, considering iso-vorticity surfaces at $\omega_r /(N\pi) = -7.5$.

To further characterize the flow induced within the reactor, the principal components of the deformation rate tensor, S_{ii}*, were assessed and their directions of action were estimated through the analysis of two angular parameters, δ_i* and γ_i* , which indicate the orientation of each principal eigenvector, with respect to the radial and tangential axes. A statistical approach was applied to determine which directions were more likely to be associated with each principal strain rate in the flow region considered, and it was found that the first and third component of the deformation rate tensor are perpendicular to the radial direction, thus lie on the azimuthal plane. Consequently, the missing direction is oriented radially.

Contour plots of S_{11}* and S_{33}* revealed that S_{11}* is associated to compression and S_{33}* to stretching of the fluid. Particularly, it was observed that the magnitude of the two eigenvalues was comparable and very modest everywhere, a part from the area close to the impeller blade and to the vortices. Then, a visualization of the directions of compression, stretching and maximum shear stress, τ^*_{max} , was provided in the core of trailing vortices.

As it is well-known that trailing vortices play a major role in the mixing dynamics occurring within a reactor, a detailed characterization of their structure and of the strain rates associated to their three-dimensional development was carried out. This type of analysis has never been performed before in a PBT stirred reactor working under laminar flow condition. Thus, the experimental data presented in this work aim at filling this lack of information, and represent novel scientific material that can also be used as a benchmark for CFD modelling validation.

In Section 4, the hydrodynamics developing within a lab-scale model digester stirred with dual A310 impeller were investigated varying operational conditions as the liquid filling ratio and the impeller rotational speed.

The simultaneous study of the velocity flow field, by PIV, and of the free surface behaviour, by visual observation and Pitot measurements, proved that a sharp correspondence between the flow field and the wave mode exhibited by the gas-liquid interface exists at any value of H_L tested. Specifically, for selected combinations of N and H_L, a flow transition was found, manifesting with changes in the impeller discharge stream inclination from typically axial to radial, and with the evolution of the free surface oscillation pattern.

From a quantitative analysis of the phenomenon, the free surface instability detected differs from any of those identified in baffled reactors, as its frequency was found mostly dependent on the geometrical characteristics of the system and not on N, although being triggered by the impeller motion. This conclusion was further validated performing additional experiments in a tank of different geometry. It was found that, independently from the vessel diameter, the free surface manifests two different oscillation patterns, depending on the combination between impeller speed and liquid height. Yet, it is worthwhile noticing that when a wave mode is established, the macroinstability frequency is irrespective of the agitation condition, depending only on the geometry of the apparatus and on the filling ratio.

Liquid sloshing theory in a confined vessel was used to interpret the outcomes of the experimental analysis, and very good agreement was found between the measured frequency data and the natural frequencies estimated analytically for a partially-filled cylindrical container. For both tiny and dumpy tanks the macroinstability frequencies, measured at low impeller speed, correspond to the zero natural oscillation mode of the free surface, thus they can be predicted by liquid sloshing theory considering the (0,1) mode as dominant.

Increasing the impeller speed, the free surface assumes different features depending on the tank diameter. In the tiny vessel, as those usually adopted in the process industry, the dominant mode is the (2,1) while for dumpy reactors, as those generally used for bio-methanation digestion, the prevailing mode is the (1,1). These findings are of great relevance for the identification of the correct operation conditions for unbaffled stirred tanks. In fact, the occurrence of wide free surface oscillations within these apparatuses has to be avoided at any cost, as it may lead to structural damages and/or to leakage of liquid (e.g. fermentation broth) in the gas collection pipes.

In the last part of this research (Section 5 and Section 6), the flow and mixing dynamics generated within shaken bioreactors were investigated.

In particular, in Section 5 an effort was made to determine the suspension speed of microcarriers in an orbitally shaken bioreactor of cylindrical geometry, and to assess the associated two-phase flow by means of Particle Image Velocimetry (PIV). Commercial GE Cytodex microcarriers were employed throughout this study to best mimic the flow conditions occurring in a bioreactor under standard operating conditions.

Suspension speed measurements were obtained through a visualization approach at different solid concentrations, that are typical for cell cultures, and for different combinations of orbital to cylinder diameters' ratio, d_o/d_i (c = 2.5 - 12.5 g/L; d_o/d_i = 0.2 - 0.7; N = 0 - 200 RPM).

The results highlighted the correlation between the microcarriers suspension and the critical Froude number corresponding to the occurrence of the flow transition identified by previous investigations for a single-phase system.

It was found that for bioreactor configurations corresponding to $\boldsymbol{h/d_i/\sqrt{d_o/d_i}} < 1$ the suspended Froude number, Fr_s, is nearly constant and equal to 1.1 × Fr_{cr}, while for $\boldsymbol{h/d_i/\sqrt{d_o/d_i}} > 1$, the suspended speed tends to increase, and suspension is delayed.

Hence, the first type of configuration should be sought because it allows to achieve full suspension minimizing power consumption and shear rates.

The dispersion mechanism was analyzed observing microcarriers distribution over a vertical plane bisecting the vessel for increasing N. It was found that before the flow transition, the particles tend to accumulate at the centre of the reactor base along spiral patterns, while after flow transition, they are sucked into the bulk flow by the depression created by the axial precessional vortex. Full dispersion is achieved at ≈ 1.2 × Fr_{cr}.

The velocity fields of the liquid and solid phases were simultaneously measured over a vertical plane bisecting the vessel, by means of a two-phase PIV technique, and the results showed that mean flow dynamics occurring in the cylindrical bioreactor are not significantly affected by the presence of the microcarriers both for in-phase and out-of-phase conditions.

This is in agreement with previous studies on stirred tank reactors where low solid concentrations are employed.

In Section 6, the flow dynamics developing within cylindrical shaken bioreactors equipped with different bottom geometries were investigated by means of phase-resolved Particle Image Velocimetry.

In particular, the effects of conical shaped bottoms of different heights on the fluid flow (h_{cone} = 5 mm and 15 mm) were evaluated under different operating conditions with water being the working fluid.

It was found that at a phase angle ϕ = 0° and for in flow condition, the flow field generated within the conical bottom bioreactor assumes the toroidal vortex configuration typically detected in standard flat bottom cylindrical OSRs. However, for the cone with the highest inclination, the interaction between the vortical cells and the bioreactor bottom starts to occur at lower speeds, thus the vortices reach the bottom at a lower *Fr*, and the space-averaged vorticity, ω_θ*, increases at a higher rate.

The proposed designs were also evaluated in terms of shear rates, and it was found that the most intense deformations occurred at the periphery of the toroidal vortices, with low shear rate values present at the centre of the vortical cells. The use of the conical geometry resulted in an area of low shear rates at r/d_i = 0.5 as the inclined surfaces of the conical bottoms modified the shape of the vortical cells, resulting in the regions of largest shear deformation being orthogonal to the cone external walls.

Finally, the kinetic energy of the random velocity fluctuations was evaluated, and the results showed that the energy content increases with *Fr* for all designs and that the *Fr* associated with flow transition does not change.

Concluding, it can be inferred that a cylindrical OSR with conical bottom provides more efficient mechanisms for solid suspensions in comparison to a flat bottom bioreactor. This has important implications for shear-sensitive cultures, as the new bioreactor design can be operated at lower shaking speeds, resulting in lower shear rates, without compromising the quality of the suspension. Also, the presence of a conical bottom could avoid solid accumulation at the centre of the bioreactor, thus allowing lower values of the just suspended speed.

List of Publications

Papers in international journals

Pieralisi, I., Rodriguez, G. , Micheletti, M., Paglianti, A., Ducci, A. Microcarriers' suspension and flow dynamics in orbitally shaken bioreactors, 2015. Chemical Engineering Research and Design;

Rodriguez, G., Pieralisi, I., Anderlei, T., Ducci, A., Micheletti, M. Appraisal of fluid flow in a shaken bioreactor with conical bottom at different operating conditions, 2015. Chemical Engineering Research and Design;

Pieralisi, I., Montante, G., Paglianti, A. Prediction of fluid dynamic instabilities of low liquid height-to-tank diameter ratio stirred tanks , 2016. Chemical Engineering Journal;

Pieralisi, I., Melillo, T., Paglianti, A., Ducci, A. Characterisation of the fluid dynamics in a reactor equipped with an axial PBT turbine, (under review).

Papers in congress preceedings

Pieralisi, I., Paglianti, A., Micheletti, M., Ducci, A. Multiphase flow in an Orbitally Shaken Bioreactor, "North American Mixing Forum - NAMF XXIV", 22-27 June 2014, The Sagamore Lake George, NY, USA (Oral presentation. Speaker: Dott. A. Ducci);

Pieralisi, I., Sacchi, L., Montante, G., Vallini, V., Paglianti, A. Analysis of Solid-Liquid Interactions in a Model Bioreactor, "17th International Symposium on Application of Laser Techniques to Fluid Mechanics", 07-10 July 2014, Lisbon, Portugal;

Papers in congress preceedings and oral presentations

Pieralisi, I., Montante, G., Vallini, V., Paglianti, Free Surface Instabilities in a Model Unbaffled Bioreactor, 10th Pacific Symposium on Flow Visualization and Image Processing, June 15-18, 2015, Naples, Italy;

Pieralisi, I., Paglianti, A., Micheletti, M., Ducci, Microcarrier flow in Orbitally Shaken Bioreactors, 15th European Conference on Mixing, 28 June-3 July 2015, Saint Petersburg, Russia.